MASTERS BY RESEARCH

High Burnup Fragmentation in Uranium Oxide Fuels for Light Water Reactors

Dixon, Lewis

Award date:
2024

Awarding institution:
Bangor University

PRIFYSGOL
BANGOR
UNIVERSITY

School of Computer Science and Electronic Engineering
College of Environmental Sciences and Engineering

High Burnup Fragmentation in Uranium Oxide Fuels for Light Water Reactors

Lewis Dixon

Submitted in partial satisfaction of the requirements for the
Degree of Master of Research
in Computer Science

Supervisor Prof. Simon Middleburgh

September 2023

Acknowledgements

I would like to thank Prof. Simon Middleburgh for being my supervisor and putting up with my constant pestering and questions. I would also like to thank Dr. Robert Annewandter for supporting me, especially for help with understanding papers and learning software and tools. I would also like to thank Dr. Michael Rushton for similarly helping me with LAMMPS and pointing me in the right direction for areas of research. Additionally I would like to thank the other PhD students in the Nuclear Futures Institute who have helped me along the way. Finally, I would like to thank Penny Dowdney and Kess2 for giving me the opportunity to take part in this project, and for funding it.

Statement of Originality

The work presented in this thesis/dissertation is entirely from the studies of the individual student, except where otherwise stated. Where derivations are presented and the origin of the work is either wholly or in part from other sources, then full reference is given to the original author. This work has not been presented previously for any degree, nor is it at present under consideration by any other degree awarding body.

Student:

Lewis Dixon

Statement of Availability

I hereby acknowledge the availability of any part of this thesis/dissertation for viewing, photocopying or incorporation into future studies, providing that full reference is given to the origins of any information contained herein. I further give permission for a copy of this work to be deposited with the Bangor University Institutional Digital Repository, and/or in any other repository authorised for use by Bangor University and where necessary have gained the required permissions for the use of third party material. I acknowledge that Bangor University may make the title and a summary of this thesis/dissertation freely available.

Student:

Lewis Dixon

Abstract

Fragmentation and pulverisation are commonly observed problematic phenomenon in nuclear fuels at burnups in excess of 65 GWd/tHM. The high burnup structure that forms at the rim of pellets with very high burnups has been shown to contribute to this pulverisation, along with other factors such as fission gas release and irradiation temperature. Fragmentation is unwanted as it can cause thermal conductivity to decrease through the introduction of insulating gas-gaps in cracks and in the spaces between fragments, and causes significant release of fission gas which will increase the gas pressure in the fuel rod. Pulverisation during a loss of coolant accident (LOCA) event typically leads to fuel relocation within the rod, and dispersion outside the rod if there is a burst as a result of rod overpressure. This project considers two approaches for determining the likelihood and amount of fuel pulverisation, through the use of mathematical modelling based on inputs from fuel performance code such as EDF's ENIGMA. The first approach, a broadly empirical model, uses a curve mapped to fragment size data from post irradiation examination (PIE) results to predict fragment sizes if a transient occurs at different temperatures. The curve is a good fit between the burnups of 60 to 100 GWd/tHM against experimental data from the Halden reactor project and Studsvik LOCA tests. The second approach, a mechanistic model based on bubble bursting, created by K. Kulacsy, was tested and its methodology validated against other literature, then modified through the addition of molecular dynamics data from LAMMPS for gas pressures. In some example bubble size distribution data for the rim region in high burnup fuel, the model predicted a coarse estimate for 98% of bubbles bursting, implying this region would almost completely pulverize into small fragments in a LOCA where the terminal temperature reached 2000K. The link between the number and sizes of bubbles overpressuring and bursting,

and the amount of pulverisation occurring needs further experimental data to prove, however current work suggests that the more bubbles that burst, the more fine fragmentation is expected. Comparison with literature supports this with a link between burnup and the average amount of gas in bubbles, and the fragment size relationship with burnup identified in the first model.

Contents

List of Figures

List of Tables

Chapter 1

Introduction

Nuclear power is an important energy source that provides low carbon, reliable and low cost energy. Reactor designs are however continuously changing to improve efficiency, safety, power output, and to decrease waste. A significant part of this process is the design, simulation and fabrication of fuel assemblies in order to improve the amount usable energy that can be extracted from the fuel through changes such as cladding materials, fuel compositions and the length of time fuel can be irradiated for.

Understanding how nuclear fuel performs inside a reactor is critical in ensuring it can run safely, and helps inform the design of new nuclear reactors and operational regimes. One method of assessing how the fuel rods perform is through the use of simulation. Computational simulation allows for performance and characteristics of fuel to be assessed under different circumstances, at relatively low cost and without the need to experimentally test new fuel rod designs. Typically fuel performance codes such as TRANSURANUS [36] and ENIGMA [54] use a combination of empirical and mechanistic models developed from experimental results to predict how fuel will behave, with predictive power limited to the data ranges they have been validated against.

This project aims to understand how fuel behaves as burnup increases through the use of EDF's ENIGMA fuel performance code to provide boundary conditions for further simulation, and for inputs into regression models built from existing data. A number of parts of this study are needed to fulfil this aim, including gathering information on, and testing tools for simulating fuel

performance. Gaining an understanding of how microstructure can impact performance is also required, as well as learning the ENIGMA fuel performance code and evaluating its outputs. The project specifically focuses on how fuel fragments as it reaches the HBS (high burnup structure) formation threshold. This fragmentation is associated with increases in fission gas release [24], decreases in thermal conductivity and increased risk of fuel dispersion in the event of a rod burst [33]. The latter point makes it incredibly important to gain a good understanding of the conditions required to, and subsequent results of, fuel fragmenting, as the potential for fuel dispersal during a rod burst is an important safety criterion.

In order to achieve this there are 2 primary focuses for this project. Initially an empirical relationship between fuel burnup and fragmentation is established, based on experimental data from publicly available post irradiation examination data of fuels subjected to simulated LOCAs (loss of coolant accidents). This identifies a simple correlation between burnup and fragment size, as well as the percentage of fine fragmentation, which poses significant risk in LOCAs due to its ability to relocate within the rod or leave through cladding bursts. Following the identification of the empirical relationship, a mechanistic gas-bubble burst model proposed by K.Kulacsy [32] is initially verified against literature, then modified to use gas pressures from molecular dynamic simulation tool LAMMPS, and to provide pressures at which different bubble sizes should burst. The model is applied to an example rim region of a high burnup fuel sample that would be expected to pulverize if the empirical relationship is used. This identifies the fraction of bubbles that would overpressurise and burst during a LOCA, resulting in the ceramic pulverizing in the rim region should the fraction be sufficiently high.

Chapter 2

Literature Survey

A variety of areas of existing research support this project, including nuclear reactor operation principles, fuel designs, fuel structure, fission product production processes, and fuel fragmentation criteria. This section will discuss the basic principles behind nuclear reactors, the design of fuel and fuel changes during irradiation, including micro-structural changes such as grain growth, high burnup structure formation and defect formation, as well as mechanical processes resulting from gas release such as creep, bursting and ballooning.

2.1 The Nuclear Reactor

Initially developed to produce fissile material for weapons in the 1940s, reactors have evolved from the relatively simple graphite moderated design of the research pile, Chicago pile 1, into complex energy generation systems designed to operate as efficiently as possible. A number of different reactor designs are in use today that mainly consist of 3 types: PWRs (Pressurised water reactors), BWRs (Boiling water reactors) and AGRs (Advanced gas reactors), other reactors such as the Russian RBMK design (used in Chernobyl) or the Canadian CANDU design are less common. Heat from a reactor is used to heat water into steam which then spins a turbine, this is common irrespective of reactor type, though PWRs and BWRs have notable differences that impact safety and reactor design. In a PWR there are 2 isolated cooling loops, the primary loop contains water pressurised to $150\,\mathrm{MPa}$ and runs at around $325\,^{\circ}\mathrm{C}$. The secondary loop, which passes through a steam generator fed by the primary loop, carries steam to the turbines [63]. Figure 2.1 shows

the general layout of a PWR and turbine systems. In a BWR there is only a single loop and it operates at a lower pressure of around $75\,\mathrm{MPa}$. Water enters the reactor core at the bottom and is heated into steam as it flows up the core before exiting at the top and flowing to turbines [63]. As a BWR only has a single coolant loop, the steam exiting the core, and entering the turbines may be radioactive due to short lived tritium and nitrogen isotopes, this means extra shielding material is needed on turbines, pumps and pipes, and makes maintenance more complex. In a PWR this is not the case (though it is the case for the primary loop piping, pumps and pressurisers). AGRs operate with a similar design to PWRs where the primary coolant passes through a heat exchanger with a secondary water loop, but uses CO_2 as a primary loop coolant gas, and are graphite moderated [63]. This work will primarily be focusing on UO_2 fuel behaviour in PWRs, other reactor types use fuels of slightly different designs (such as annular fuel in AGRs), chemistry (such as UN and MOX), enrichment and desired performance characteristics.

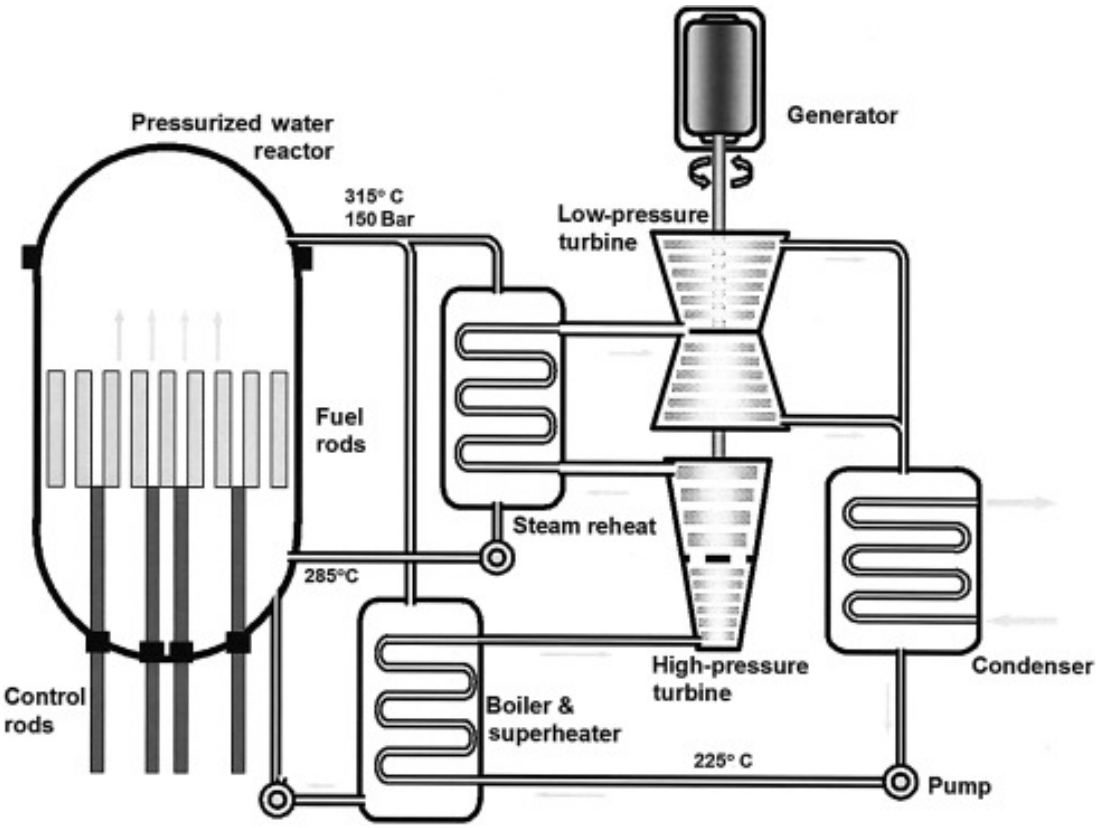

Figure 2.1: A PWR layout, adapted from [60]

2.1.1 Fuel

The most common fuel type in reactors is UO_2, this is commonly enriched up to 4.95% in PWRs, but can be lower in other reactor types with more moderation. Fuel is formed into small pellets, typically 10mm diameter by 10mm height [63], which are stacked into a fuel rod and held in place by a spring. Fuel rods (or pins) are placed into a typically square fuel assembly of around 17x17 rods about 3-4m tall that is then placed into the reactor (see Figure 2.2). Not all fuel channels in the assembly are filled to allow space for instrumentation and/or control rods or water rods for increased moderation. Spacing between individual rods is only a few mm filled by water.

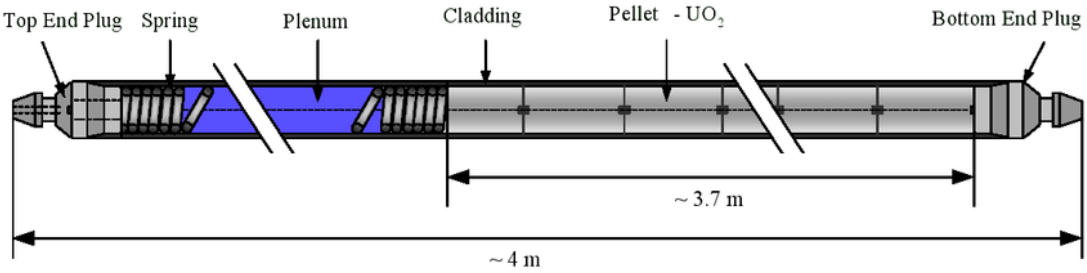

Figure 2.2: A typical fuel rod design seen in a PWR, sourced from [5]

In PWRs, enriched uranium is required. Uranium naturally occurs as 99.3% $^{238}\mathrm{U}$ [45]. $^{235}\mathrm{U}$ is the primary fissile isotope, and undergoes fission when struck by thermal neutrons slowed by the moderator, $^{238}\mathrm{U}$ however, only undergoes fission when struck by fast neutrons, accounting for about 3% of fissions. Figure 2.4 shows the differences in neutron absorption cross sections. In order for fuel to be viable in a PWR, it must have its $^{235}\mathrm{U}$ content increased to around 4%.

The UO_2 fuel is itself a brittle ceramic with a cubic crystal structure [39]. The lattice structure allows for the formation of defects such as interstitial sites, enabling the diffusion of fission products throughout the crystal. Individual grains of UO_2 exist at differing orientations providing grain boundaries which fission gas products can diffuse to. As with any ceramic, under heating grain growth is observed, however UO_2 experiences the formation of a high burnup structure in the rim region of pellets characterised by the sub-

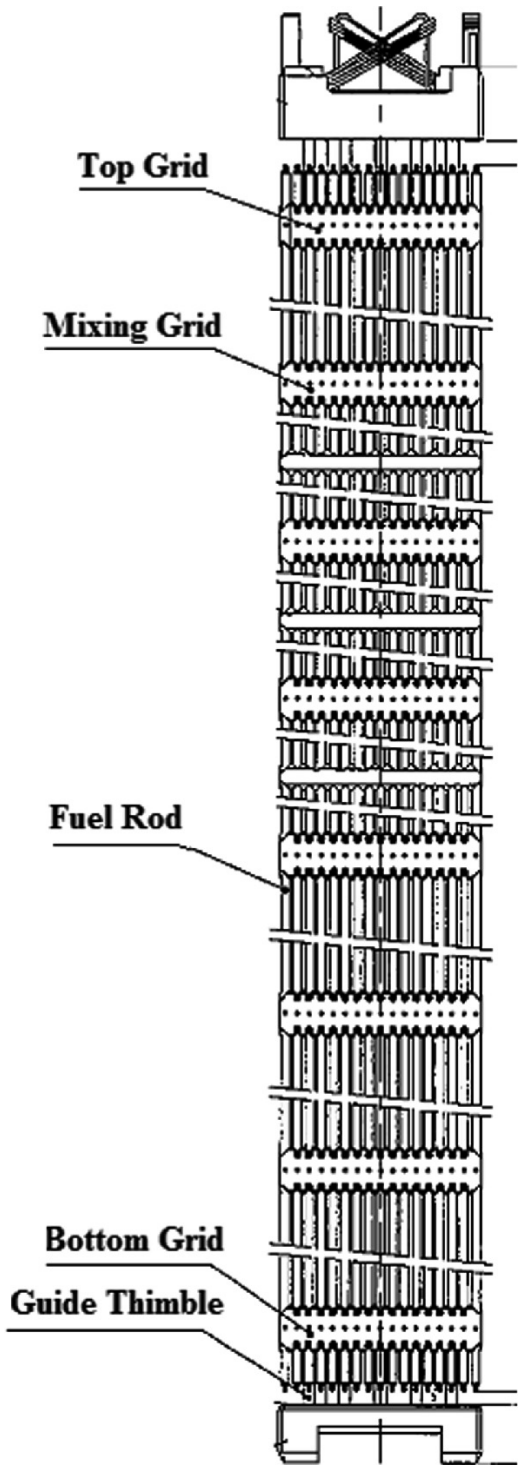

Figure 2.3: A typical fuel assembly used in a PWR, adapted from [34]

division of larger grains into significantly smaller sub-micron grains [52]. This structure has potentially undesirable impacts on fuel characteristics, such as decreasing thermal conductivity, increasing gas retention and decreasing fracture resistance.

Various aspects of fuel operation and performance will be discussed in the following sections.

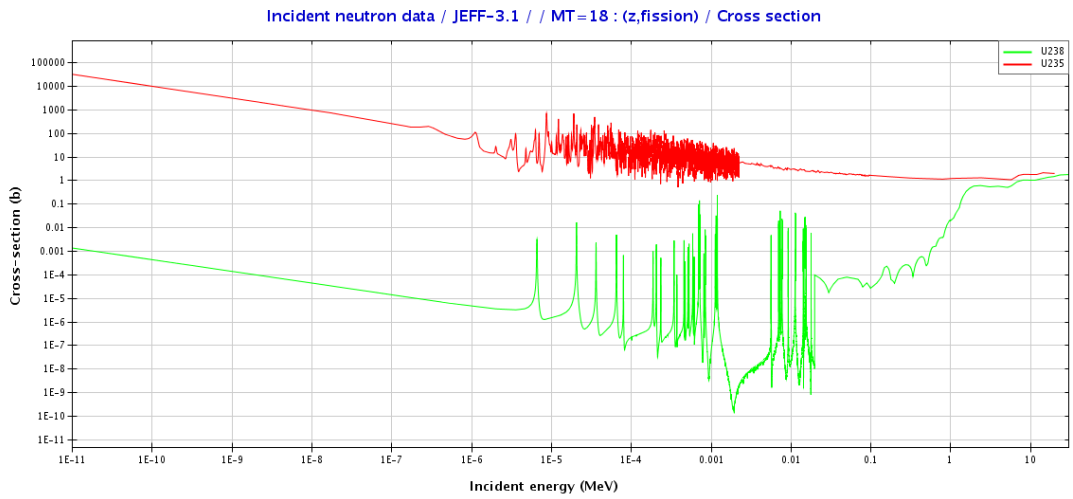

Figure 2.4: Neutron absorption data for U-238 and U-235. U-235 presents a significantly larger cross section to low energy neutrons compared to U-238 which only has a large cross section for neutron energies over 1 MeV (Fast neutrons). Data Sourced from JANIS web [58].

2.1.2 Moderation

In a PWR, light water is used as both a moderation medium and coolant. In reactors with lower overall reactivity, such as those using natural uranium fuel, heavy water is used or different moderation materials such as graphite. The moderation is required to slow high speed neutrons into thermal neutrons which are more likely to cause a subsequent fission event, perpetuating the chain reaction. Excess reactivity can be managed by 'poisoning' the fuel to reduce its reactivity, or by lowering neutron absorbing control rods into the reactor, or by adding a soluble neutron absorber (typically boron) into into the primary coolant loop [63]. In general, it is necessary to have a constant critical reactivity other than when changing the reactor power, as to maintain a stable number of fissions per second where one fission causes only one other and so on. Under accident conditions, spikes in reactivity can cause subsequent spikes in temperature which can lead to overpressuring of fuel pins, boiling of coolant water, and damage to fuel and fuel rods. In PWRs temperature spikes can also decrease reactivity through a negative feedback loop due to the effect of the doppler coefficient on uranium-238, causing it to absorb more thermal neutrons, reducing the number available for the fission process. A number of different coefficients play a role in this, the fuel temperature coefficient, moderator temperature coefficient and void

coefficient are all negative. The void coefficient is the most negative by far, but only lowers reactivity when the coolant begins to boil.

2.2 Fuel Performance Code

A number of tools exist to simulate the performance and characteristics of nuclear fuel. These range from higher level engineering codes that use empirical models to predict behaviour, down to atomistic modelling codes that simulate interactions between individual atoms. Engineering codes are commonly used for the evaluation of fuel designs, positioning of fuel in reactors, and predicting fuel degradation. Industry codes such as TRANSURANUS [36] and ENIGMA [54] fulfill these roles and are typically 1 - or 1.5 - dimensional, calculating fuel behaviour at slices long the length (axial position) of a rod, and at radial positions for each axial position. For more in depth simulation, finite element modelling or molecular dynamics that can simulate the individual interactions occurring between fuel grains, or right down to atomistic scale where behaviour of atoms can be simulated that may not match the coarser engineering models under certain circumstances, especially beyond the validated bounds of these models. A few tools, such as BISON [68] can perform more complex multidimensional simulations that incorporate both the models used in engineering code, and more models from the first-principle.

Engineering code has to take into account a number of closely and loosely coupled performance criteria, many of which have circular dependencies. However, due to the more empirical nature of engineering code its not always capable of predicting the exact behaviour of fuels, typically where models are based on older work or assumptions based on limited research. With the primary use case of these tools being the evaluation of fuel performance, they need to run very quickly. In the case of a tool such as ENIGMA, it may be used to simulate an entire reactor core of upwards of 225 rods. While this may not seem like a large number now, many codes were written to run on very early computers with limited processing power and have been upgraded

over time to include more complex relationships, and to upgrade models from empirical relationships to more mechanistic ones.

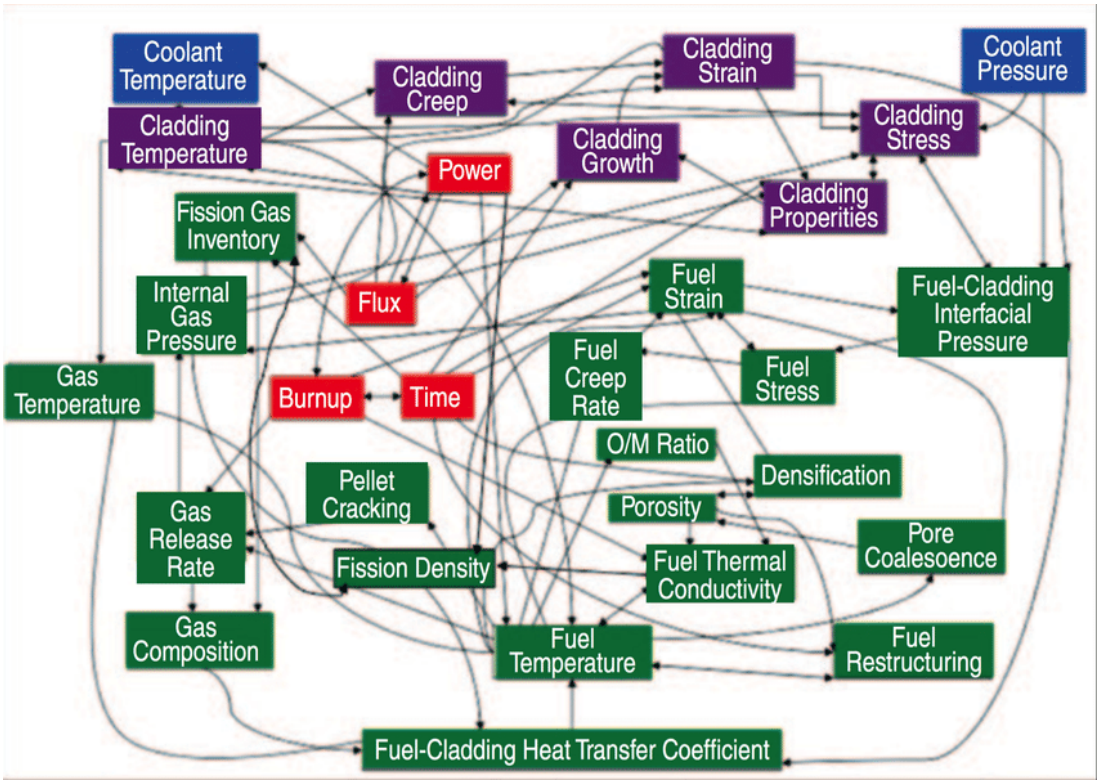

Figure 2.5: The factors and relationships involved in fuel modelling, taken from [62]

A number of factors can be used in fuel performance code to evaluate fuel condition. A significant factor that tends to affect many others is burnup. Burnup is a quantification of the condition of the fuel over its lifetime as a measure of either the number of atoms that have undergone fission or the total amount of energy released by the fuel (typically measured in GWd/tHM or MWd/kgHM - giga-watt days per tonne heavy metal) [62]. Another important factor is fuel temperature as this can normally be associated with higher gas diffusion and release rates as well as temperature induced micro-structural changes. It is however worth bearing in mind that these factors fail to consider other criteria that may significantly impact how fuel behaves. Burnup for example is only a measure of energy release, it doesn't consider at what rate that release took place and so factors like fission rate, fuel cracking, densification as well as the starting conditions of the fuel structure all play a significant role in impacting its performance. Its therefore very important that fuel performance codes consider these factors in the models they use. Empirical relationships suffer from limitations where there is not sufficient

data to properly support a relationship, or where models fail to work when extrapolated beyond experimental ranges. With these in mind, most modern fuel performance codes use far more mechanistic micro-structural based models - though still based on equations in literature describing phenomena, typically partial differential equations - for these [12]. The most commonly included factors are: grain growth, thermal conductivity, fuel cracking and fragmentation, fission gas production, diffusion and release, fuel densification and swelling, and thermal and irradiation driven creep [12] [62] [66]. Code typically also considers how cladding behaves, with similar factors like creep rate, stresses and strains, and oxidation [62].

2.3 Fuel Physical Processes

During irradiation a number of physical processes occur, these are driven by radiation, heating or chemical processes occurring in the fuel. These processes can significantly impact the characteristics of the fuel, so are commonly used in the models in fuel performance code. An overview of some of the more important processes is presented below. many of these are relevant for fuel fragmentation behaviors.

2.3.1 Fission Gas Behaviour

Fission gas behaviour encapsulates a variety of processes including production, diffusion and release of gaseous fission products. Fission gasses account for approximately 30% of fission products [61], with the majority of this being xenon, followed by krypton. These gasses form intra- and inter-granular bubbles and may contribute to the weakening of the crystal lattice through the formation and overpressurization of these bubbles [32]. It is also understood that these gasses lower the thermal conductivity of the UO_2 [11] by introducing insulating gas-bubbles. The decrease in thermal conductivity increases fuel centre temperatures, resulting in a positive feedback loop causing the generation of more gaseous fission products as a result of higher temperatures [61][43]. Fission gasses also contribute to the internal fission gas pressure, which exerts stresses on the cladding, increasing the

risk of cladding ballooning, especially in events where pressures rise very quickly, and also contribute to fuel cracking and pulverisation, especially at higher burnups. The process of FGR takes place in 3 stages: initially gasses diffuse through individual grains then form bubbles on grain faces and interconnections with grain edge bubbles, before finally escaping due to interconnected grain face bubbles proving a pathway to free surfaces and being released [61]. This process can be seen in figure 2.6

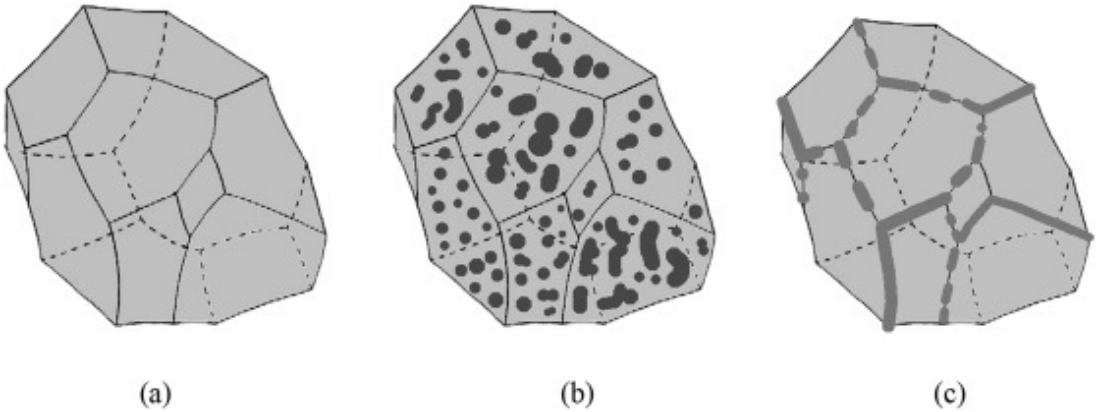

Figure 2.6: Stages of bubble transport as identified above. (a) shows a polycrystalline structure with grain boundaries as solid lack lines. (b) shows the nucleation of grain face bubbles, and (c) shows grain edge transport routes that alow gas to dffuse to free surfaces. Figure taken from [61]

2.3.2 Creep, Swelling and Expansion

Creep is the process of the deformation of a material over time in response to mechanical stresses. In nuclear fuels creep is mainly observed in the rod cladding, it is partially driven by irradiation and by heating, and contributes (along with fuel expansion) to a decrease of the pellet-cladding gap. Creep is a precursor to ballooning, although creep is a comparatively slow deformation of 10s of microns whereas ballooning can be a relatively fast process of deformation over a few mm in a short period of time in response to rapidly increasing stresses. Swelling also occurs in the ceramic fuel, causing an increase in fuel volume over time through the replacement of atoms with fission products. A number of processes cause this, but the most common causes identified are the build up of solid fission products within the crystal structures, and from the nucleation of fission gas bubbles due to low gas solubility within the UO_2 matrix [19][37]. The material will deform once the

stresses reach its yield strength [55], however other deformation processes such as cracking and relocation may have already taken place. In the temperatures of normal operating conditions, it is unlikely that cladding creep and fuel swelling is driven primarily by temperature, but by irradiation, closely linked to the fission rate and subsequent exposure to thermal neutrons. [6]. Figure 2.7 shows the stages of cladding creep and fuel swelling during the lifetime of fuel.

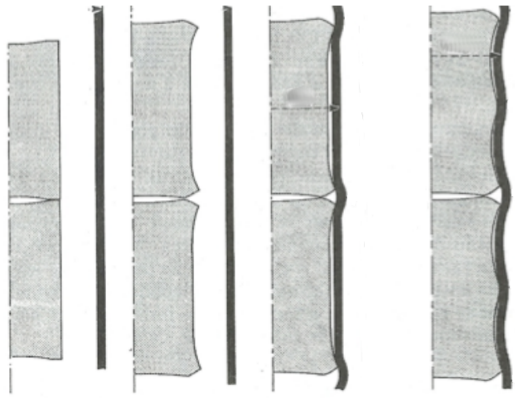

Figure 2.7: Stages of cladding creep and pellet swelling during fuel runtime. The far left image is the fuel as fabricated, the far right is the fuel after undergoing irradiation for a long period of time. Adapted from [7]

2.3.3 Cracking and Fragmentation

As soon as UO_2 is exposed to the high radiation environment of a running reactor, fission events taking place and generating heat in the fuel cause significant thermal stresses to occur. This immediate increase in internal stresses is typically relaxed with radial cracking. UO_2 has poor thermal conductivity ($9\,\mathrm{W\,mK^{-1}}$ at $300\,\mathrm{K}$ to just over $2\,\mathrm{W\,mK^{-1}}$ at $1500\,\mathrm{K}$) [46] , so experiences a significant temperature difference between its centre temperature and surface temperature. Over the distance of approximately 5mm the temperature typically decreases from over $1000\,°\mathrm{C}$ in the centre to $500\,°\mathrm{C}$ at the pellet surface [7], resulting in a very steep temperature gradient. As the fuel is a ceramic it has very little capability to deform to relax these thermal stresses placed on it, and so will crack. Figure 2.8 shows this thermally induced cracking. This cracking is observed in almost all nuclear fuels, and radial craking is very common as soon as the fuel is exposed to high temperatures, even those of very low burnup. The cracking increases

the volume of the fuel, as well as causing the relocation of smaller fragments radially within the rod. This redistribution and movement of the fuel will decrease the pellet cladding gap, and decrease thermal conductivity between fragments. Further cracking is observed as burnup increases, continuing to relax stresses caused by defect buildup and thermal and irradiation damage. During temperature transients additional cracking is observed between the larger initial cracks. Initial fuel state also has an impact on the amount of fracturing that takes place, a higher as-fabricated porosity for example will make the fuel more susceptible to cracking due to a reduced fracture strength.

Cracking has a number of impacts on fuel properties. Stated previously, cracks provide free surfaces for fission gasses to escape the ceramic from, they also impact thermal conductivity by effectively creating gas-gaps between individual fragments resulting in thermal conductivity barriers. Cracking also increases the susceptibility of the fuel to pulverisation, especially in the event of a LOCA (loss of coolant accident) [64] - however normal large fragments are still of importance in this situation. The finer fragmentation is generally associated with the formation of a high burnup structure at the rim of pellets. While this finer fragmentation is believed to primarily come from the rim region of pellets, there may be some finer fragmentation further towards the core of pellets in areas with higher porosity. Publicly available post irradiation examinations for fuel that has experienced artificially induced LOCAs have typically only focused on the sizes of fragments, not where they came from. Higher porosity is associated with lower fracture strength [32], However measurements of porosity show it increases fairly predictably towards the pellet rim.

2.3.4 High Burnup Structure Formation

The high burnup structure forms within $100\,\mu$m of the pellet rim as average pellet burnup increases beyond 60GWd [49]. The HBS is observed to form only where irradiation temperatures are below $1000\,^{\circ}$C [49]. The structure grows towards the centre of the pellet, though due to limitations on the maximum

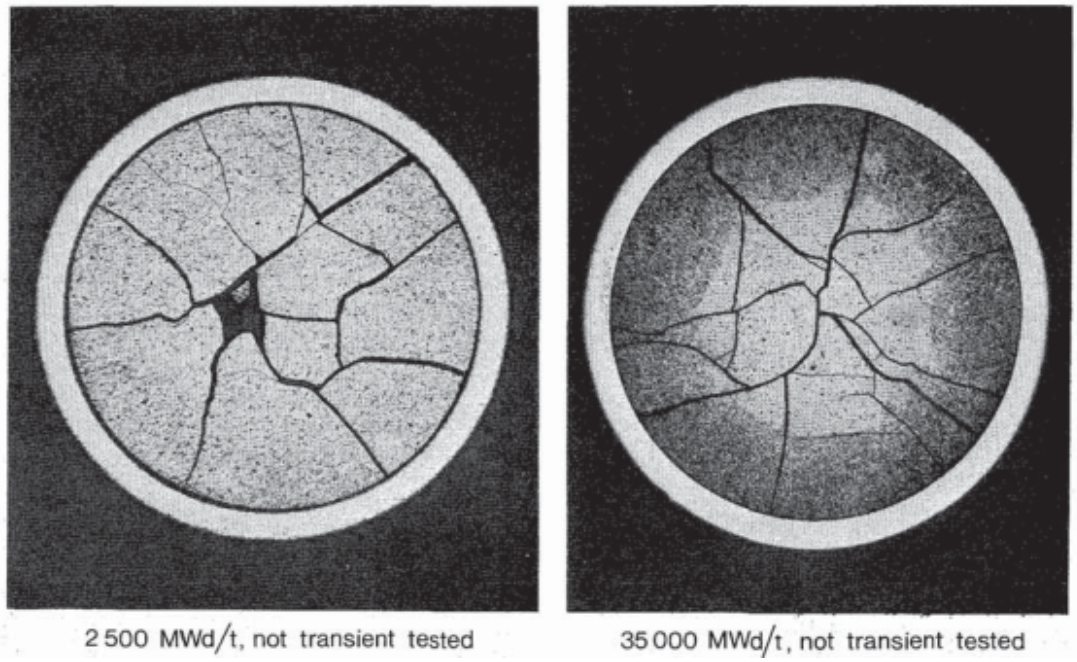

Figure 2.8: Cross sections of pellets at relatively low and medium burnups from the FR-2 reactor. Cracking as stated previously occurs as soon as the fuel experiences thermal stresses, as evident in the 2500MWd burnup image. Slightly more cracking, though minor is visible in the higher 35000MWd image. [29]

burnup fuel can reach in a reactor it generally never forms more than $1\,\mathrm{mm}$. The HBS is associated with a number of significant structural changes, but is characterised primarily by the subdivision of larger grains into smaller, sub-micron grains around $0.1\,\mu\mathrm{m}$ to $0.3\,\mu\mathrm{m}$ [69] and a significant increase in trapped intergranular fission gasses. Intragranular porosity notably decreases in the HBS, which contributes to some restoration of the intragranular thermal conductivity, however overall thermal conductivity decreases due to the increase in intergranular porosity. Figure 2.9 shows the structural changes observed in the HBS compared to a normal fuel grain structure, as well as identifying some conditions required for its formation. HBS is undesirable as it decreases thermal conductivity at the pellet periphery, is a significantly weaker structure than the unaffected UO_2, and is highly susceptible to pulverisation in temperature transients and LOCAs. It was initially believed that HBS also contributed to an increase in fission gas release, this is still factored in certain performance codes, however a number of experiments and reports now suggest that fission gas is instead trapped in the HBS [65] [40] [69] and is more likely released if fragmentation occurs [65]. There is also evidence suggesting that irradiation temperature affects the onset

of HBS formation, were it will not form provided the temperature is high enough [69], this may be due to temperature driven defect healing causing recrystallisation.

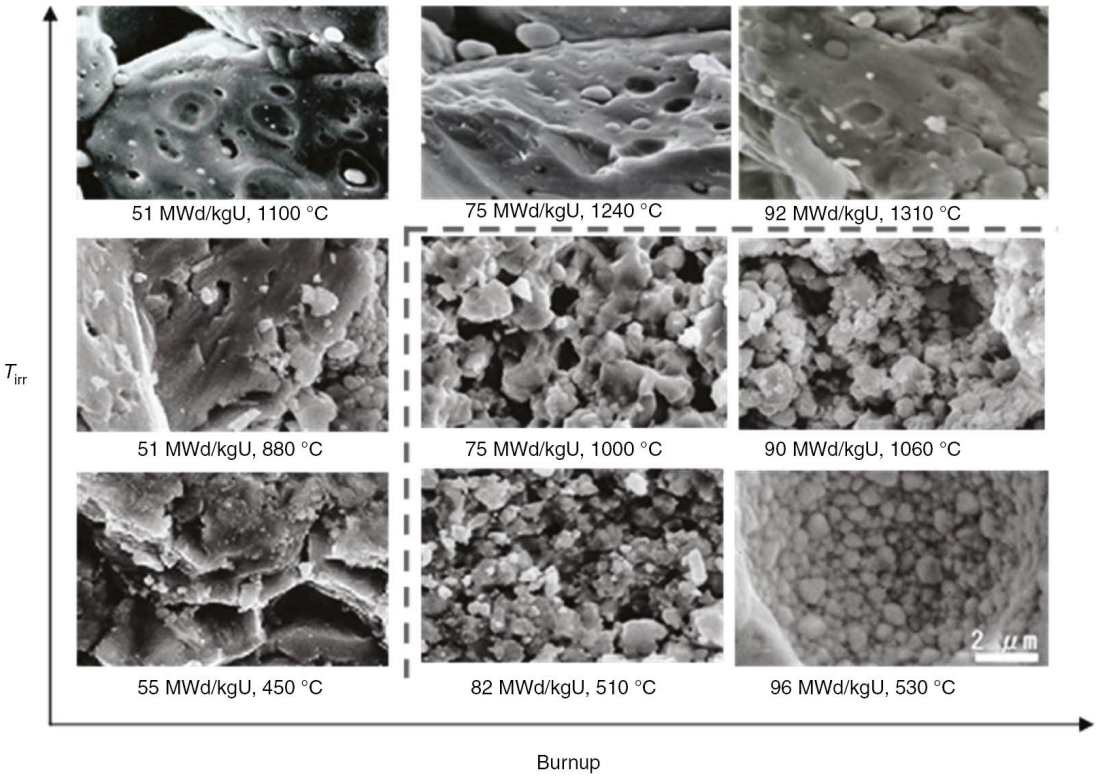

Figure 2.9: SEM images showing fracture surfaces of differing burnups and irradiation temperatures, the images within the dotted line are from samples showing formation of the high burnup structure, note the obvious smaller grains and higher porosity in these images. Sourced from [69]

2.4 High Burnup pulverisation

Sections 2.3.4 and 2.3.3 discuss the processes involved in fuel pulverisation, however understanding the affects of these processes is important too. A number of experiments [14][15][29][10] have been conducted to understand the results of fuel pulverisation following either transients or LOCA events, typically through PIE of fuel samples. Experiments conducted on high burnup light water reactor fuel after Chernobyl showed fragmentation as a result of rapid heating, as well as significant gas release [24]. Earlier out-of-pile transient tests on LMFBR fuel (mixed oxide fuel) through the 1970s and 1980s showed evidence of very fine gas-induced fragmentation due to overpressuring of gas pores. Projects such as the Halden reactor project and the Studsvik LOCA test project have been run to allow fuel subjected to high

burnups to be exposed to temperature transients simulating the conditions of a LOCA in order to collect data on cladding ballooning, fission gas release and fuel pulverisation. Heating rate also impacts pulverisation, with faster heating rates showing higher fractions of very fine pulverisation compared to slower heating rates. Early testing suggested the minimum heating rate was over $100\,\mathrm{K\,s^{-1}}$, but later tests showed this could be as low as $50\,\mathrm{K\,s^{-1}}$. For fast enough heating rates, the rate at which bubbles can grow to relax internal pressures is lower than the rate of pressure increase leading to their overpressuring, burst, fission gas release and thus induced pulverisation [24][71].

Pulverisation data is important for this project as it is the basis for an empirical relationship between burnup and the susceptibility for fuel to pulverize. Dr. Tony Turnbull suggests a threshold for both burnup and temperature where sub 1mm pulverisation is observed in fuel subjected to a LOCA [64] defined by equation 2.1, He does however note that the majority of the powder was more likely to be from 20 to 200 µm, and that < 1mm is potentially too coarse for an upper limit. Jernkvist suggests that the finer fragments formed under accident conditions by bubble bursting may exist down to grain size (approximately $10\,\mu$m) [24], and fragments formed by thermal stresses at the pellet surface are likely to exist between 0.1 mm to 0.5 mm [42].

$$P(Bu,T) = 1 \begin{cases} \text{for } T > T_{vb}(Bu) \wedge 70 < Bu < 95, \\ \text{or } T > 635 \wedge 95 < Bu \end{cases} \tag{2.1}$$

Where T_{vb} is defined by equation 2.2.

$$T_{vb} = (-11.24 * Bu) + 1703.8 \tag{2.2}$$

T is the terminal temperature in °C, Bu local burnup in GWd/tHM. These equations define the area above the red line in figure 2.10. In order for pulverisation to take place both the burnup and temperature conditions defined in equation 2.1 must be met, in either the first or second case.

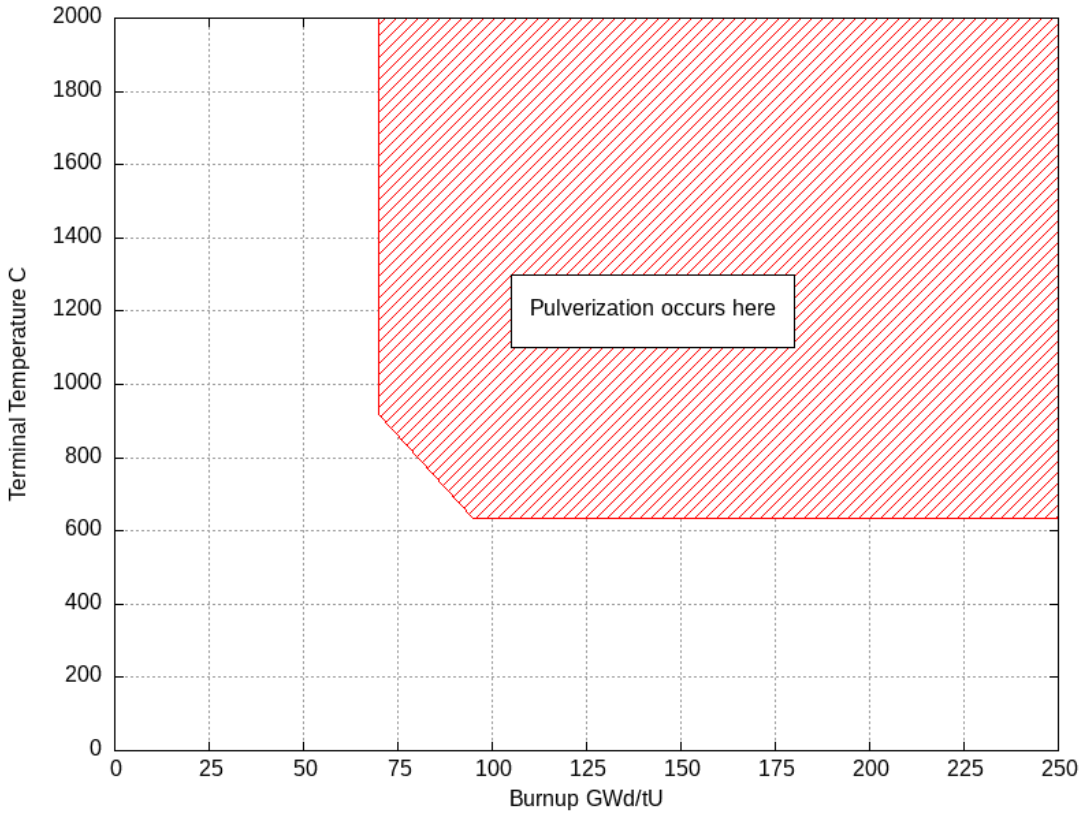

Figure 2.10: The threshold as defined by equation 2.1. Any fuel that experiences burnup and temperature conditions that fall within the shaded area is likely to experience pulverisation. Reproduced from [64]

While this threshold is useful in predicting fuel pulverisation, and can play a role in fuel performance code, it is a rather coarse threshold that simply defines a true or false as to whether small pulverisation takes place. It may therefore be better to consider the fragment size distributions for fuel exposed to LOCA conditions and set a limit for a fragment size defined as pulverisation, and that can be considered a risk in relation to the severity of the LOCA. A number of experiments have collected this data on fragment sizes, which potentially allows for a more detailed burnup threshold to be defined, and an empirical relationship between burnup and the percentage of pulverisation expected in a fuel. Fragment size data is presented through the following figures.

Figure 2.11: PIE fragment size data from (a) PBF and (b) FR-2 tests. Reproduced from [57]. See 2.14 for more detailed distribution data.

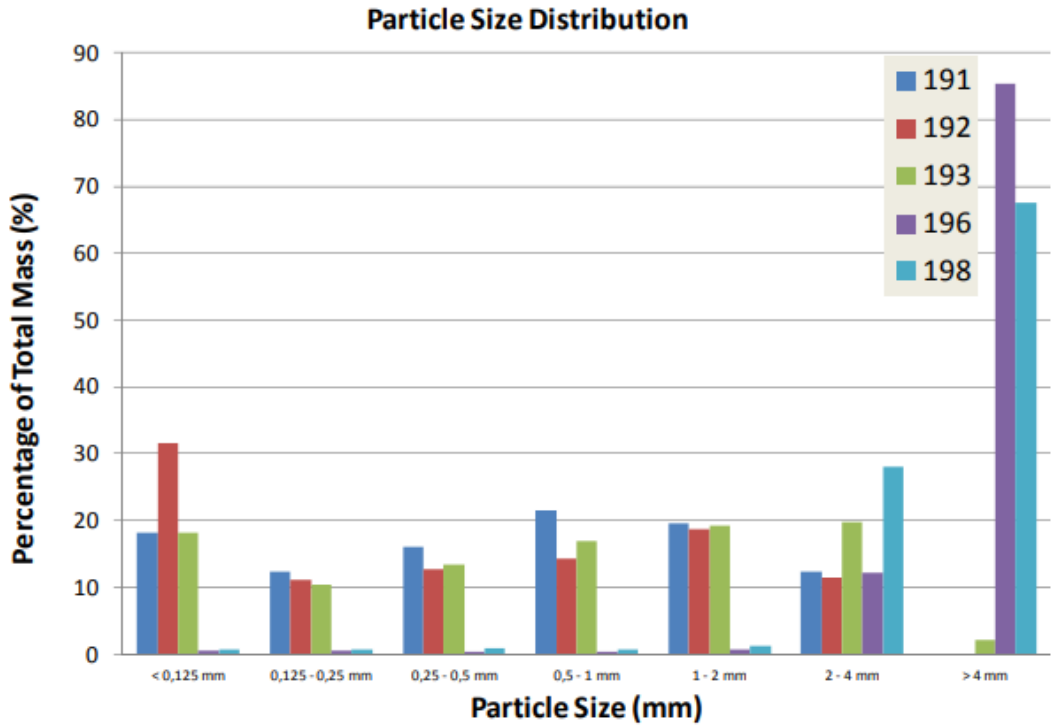

Figure 2.12: PIE fragment size data for publicly available Studsvik LOCA tests 191 to 198. Sourced from [13]. Test data in table 2.1.

Table 2.1: Test conditions for figure 2.12. PCT - Pellet cladding temperature. Data source [57].

Test	Burnup (GWd/tHM)	PCT (°C)	Time at PCT (s)
191	69	1185	25
192	68	1185	5
193	69	1185	85
196	55	700	
198	55	1185	85

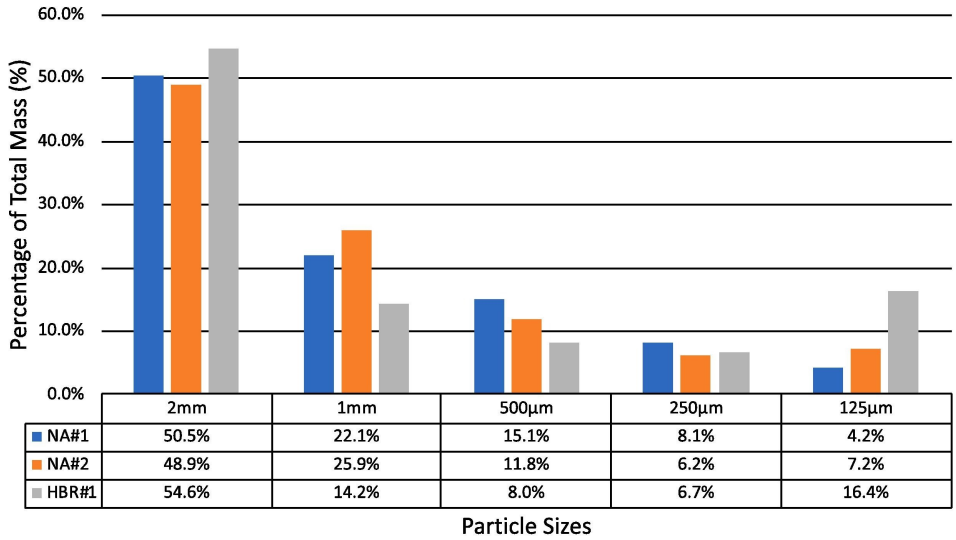

	2mm	1mm	500µm	250µm	125µm
NA#1	50.5%	22.1%	15.1%	8.1%	4.2%
NA#2	48.9%	25.9%	11.8%	6.2%	7.2%
HBR#1	54.6%	14.2%	8.0%	6.7%	16.4%

Figure 2.13: PIE fragment size data for the NA#1, NA#2 and HBR#1 tests conducted at ORNL. Sourced from [10].

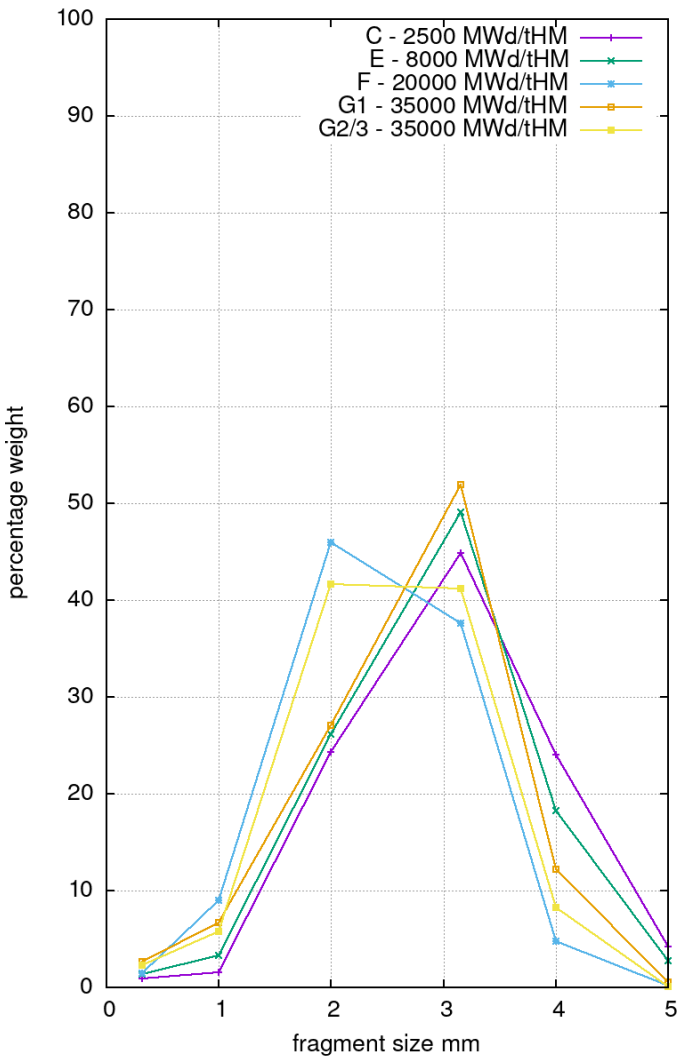

Figure 2.14: More detailed PIE data than 2.11 for the FR-2 LOCA tests conducted on low burnup fuel. Reproduced from [29].

Table 2.2: Fragment distribution data for Halden IFA-650 experiments as percentages of fuel mass. Reproduced with data from [57] and [10]. Samples in bold have less data publicly available. The last 4 samples do not have quantitative fragmentation data available, but are described as 'medium and fine', this is taken to mean 100% sub 1mm pulverisation.

Rod	**Burnup**	**Fragment Size Bin**						
		<0.125mm	0.125-0.25mm	0.25-0.5mm	0.5-1mm	1-2mm	2-4mm	>4mm
#	GWd/tHM			%				
650.12	72.3	0.01	0.03	0.06	0.11	0.13	1.88	97.78
650.13	74.1	0.4	0.12	0.14	0.13	0.02	0.01	99.18
650.14	71.1	0.46	0.12	0.15	0.12	0.03	1.09	98.03
650.15	**64.8**		**6.1**		**2.4**		**91.5**	
650.3	**81.9**		**100**				**0**	
650.5	**83**		**100**				**0**	
650.9	**90**		**100**				**0**	
650.4	**92**		**100**				**0**	

The above data presents a variety of fragment distributions at different burnups. The starting point for fine fragmentation mostly agrees with the threshold suggested by Dr. Tony Turnbull, though temperature has not been factored in these cases. Data from the FR-2 tests appears to show quite significant fragmentation at very low burnups, likely the result of thermally induced cracking. Interestingly, the data from Studsvik (See graph 2.12) shows reasonably high fine fragmentation below the Turnbull threshold, however Halden rods 650.12 to 650.14 (see table 2.2) have very low fine fragmentation despite being above the Turnbull threshold for both temperature and burnup. To further this, a model proposed by the US NRC puts a starting burnup for fine pulverisation below 1mm at 55GWd [3], and a predicted sub 1mm pulverized mass percentage, m_p, given by equation 2.3 [3]:

$$m_p = \begin{cases} 0.4 * (Bu - 55) & \text{for } 55 < Bu < 80, \\ 1 & \text{for } 80 < Bu \end{cases} \tag{2.3}$$

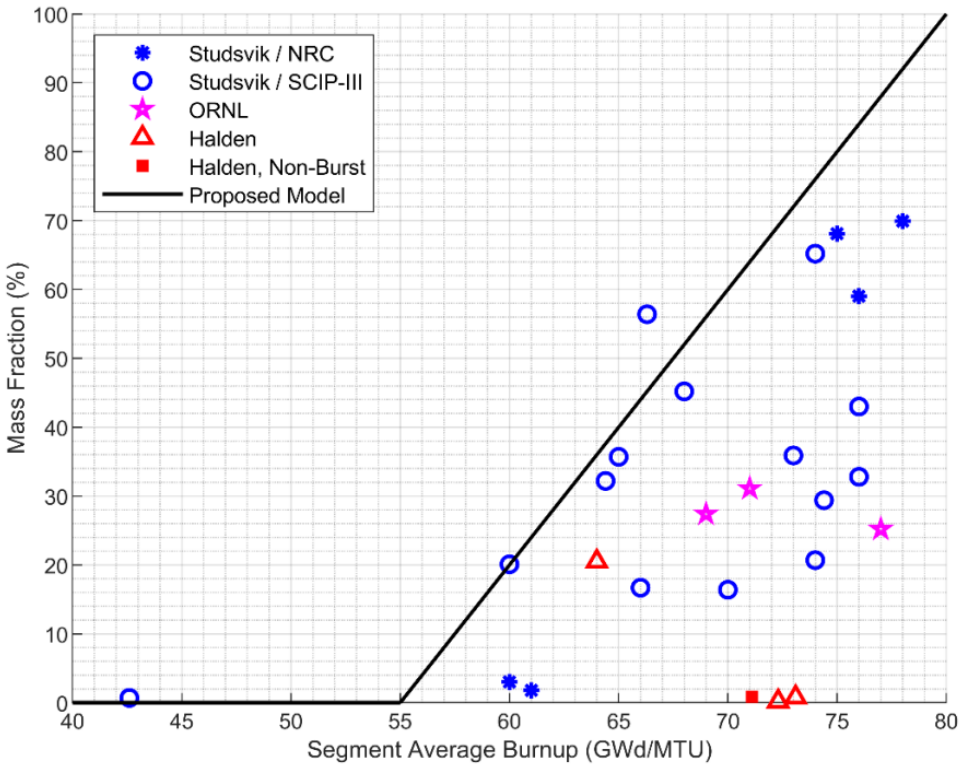

Figure 2.15: Maximum possible 1mm pulverisation fraction for fuel burnup as proposed by the NRC, following the above equation. A significant number of samples fall below the line, however this appears to be a cutoff with no samples bar one being above it. Sourced from [3].

While the NRC describes this as a threshold for dispersable fuel (and the accompanying parameters for 2mm pulverisation), It is useful in its definition of a fraction of pulverized fuel rather than the simple true or false from Turnbull's model. Considering the data from the FR-2 experiments (see figure 2.14), it is likely that fragment sizes fall into a bell curve, so this proposed model may well align with Turnbull's pulverisation threshold as discussed earlier, though more detailed data is required to validate that.

Chapter 3

Modelling Approaches

For this project, two main areas were focused on: initially the creation of an empirical relationship between burnup and pulverisation; and a second mechanistic evaluation of the potential causes of fine fragmentation. The initial empirical model would ideally be integrated with the ENIGMA fuel performance code from EDF in order to provide basic pulverisation predictions. The mechanistic evaluation is based on a fission gas model proposed by Katalin Kulacsy [32], modified to use gas pressures provided by molecular dynamics simulations in LAMMPS.

3.1 Empirical Model

Burnup and fragment size share a relationship where an increase in burnup generally signifies a decrease in average fragment size; or an increase in fine fragmentation. With this in mind, it is possible to describe this relationship mathematically through the analysis of PIE fragment size distribution results. While this does not factor in other impacts on fragmentation such as temperature and fission gas behaviours, the empirical nature means it should hold true for most circumstances.

3.1.1 Background

The data from section 2.3.4 was collated and the average fragment size for each burnup value was calculated and formed into table 3.1. Temperature data has been included where available. The calculation of the average fragment size was done using the midpoint within a size bin, for example, the mass of fragments between 1 and 2 mm was calculated with 1.5 mm

assumed as the average size for that range. For upper ranges, where the range was >4 mm, for example, the pellet diameter was used as the upper bound so the size used in the average calculation typically falls around 6 to 7mm. It is expected that for larger fragments, the distribution forms a bell curve, evident from the distribution data from the FR-2 experiments in figure 2.14, thus selecting a size to use for the average calculation within the upper upper size bounds as a value halfway between the lower bound and pellet diameter is logical. For smaller fragments, the distribution may be more like a logarithmic curve, with more fragments falling towards the bottom bound of a size bin, following the general trend of the fragment distribution data for the sample. There is some evidence to suggest this in figures 2.12 and 2.13 - though it is inconclusive and no finer measurements exist. However, in order to ensure consistency the distribution has similarly been assumed as a bell curve and a midpoint selected for the calculation because of this.

Table 3.1: Average fragment sizes for publicly available fragment size distribution data.

Rod Averge Burnup GWd/tHM	**Average fragment Size** mm	**Terminal Temperature** C	**Test**
75	1.35	1185	Studsvik 191
78	0.91	1185	Studsvik 192
76	1.22	1185	Studsvik 193
61	5.48	950	Studsvik 196
60	5.15	1185	Studsvik 198
72.3	6.90	800	Halden IFA 650.12
74.1	6.95	800	Halden IFA 650.13
71.1	6.90	860	Halden IFA 650.14
64.8	3.92	850	Halden IFA 650.15
81.9	0.5	850	Halden IFA 650.3
92	0.5	850	Halden IFA 650.4
83	0.5	1100	Halden IFA 650.5
90	0.5	1000	Halden IFA 650.9
71	1.31	1000	ORNL HBR#1
74	1.33	1200	ORNL NA#1
84	1.32	1000	ORNL NA#2
2.56	3.07		FR-2 C
8	3.03		FR2-E
21.91	2.21		FR-2 F
33.78	2.47		FR-2 G1
36.52	2.62		FR-2 G2
10.76	3.13		PBF
16	3.1		PBF
16.6	3.2		PBF

There are some outliers in table 3.1, notably the lower burnup data from the PBF and FR-2 tests, as well as three high burnup samples from Halden. The lower burnup samples are likely experiencing cracking into large fragments

due to thermally induced stresses, figure 2.8 shows the fracture pattern seen in the FR-2 pellets, which does not show the pulverisation expected from higher burnups. The three high burnup samples from halden that are outliers appear to show almost no fragmentation. The terminal temperature reached by these samples was not significantly lower than that of the other samples, however IFA-650.14 had much lower free volume in the rod than 650.3 to 650.9 [23] and did not burst. Similarly IFA-650.12 did not burst during the transient, but did during the cooldown. The data was cleaned of these potential anomalies and when plotted against burnup in figure 3.2, it is possible to estimate a curve that can give a reasonably accurate relationship between burnup and average fragment size.

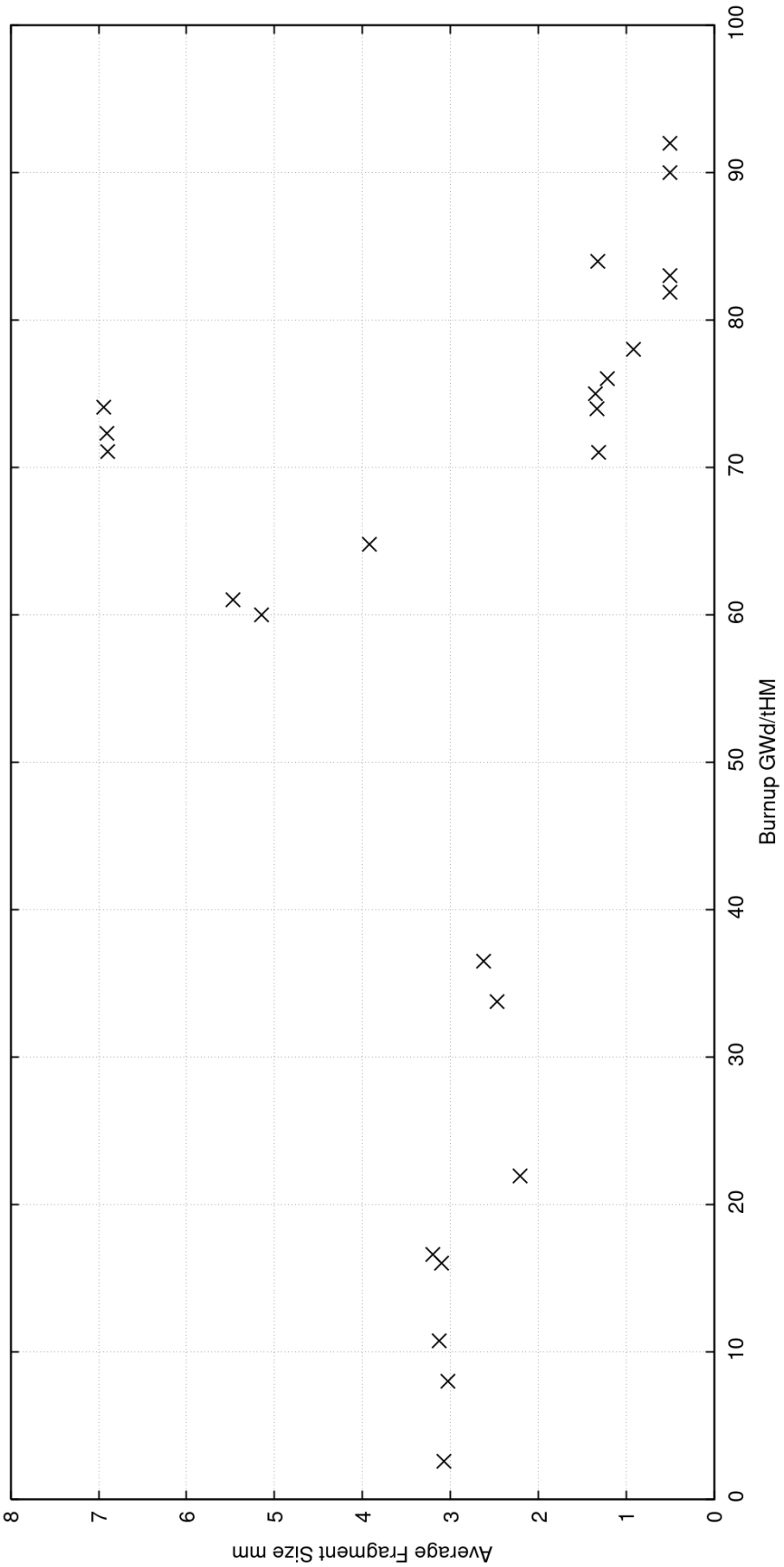

Figure 3.1: Data in table 3.1.

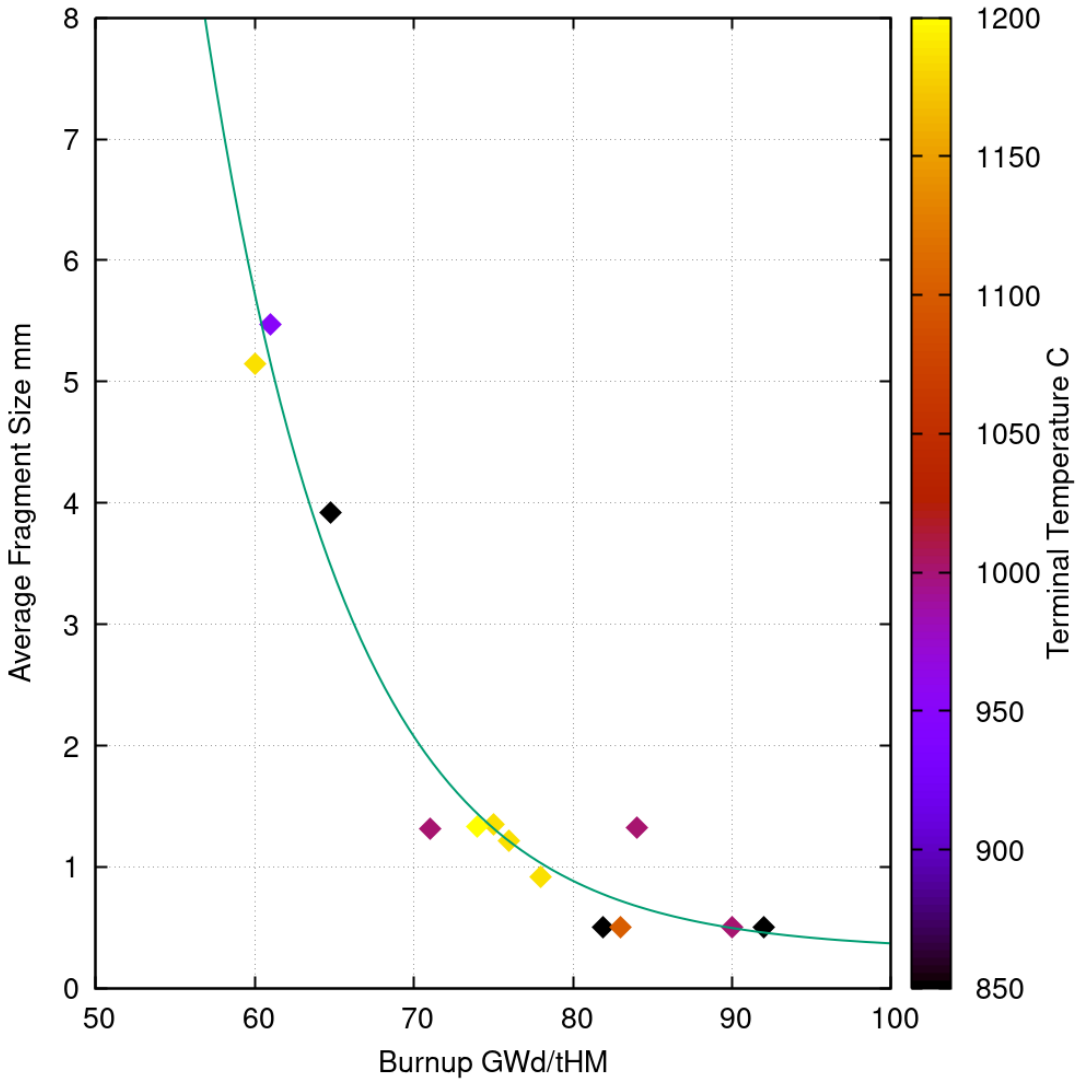

Figure 3.2: Filtered data from table 3.1 with low burnup and anomalous samples removed as low burnup fragmentation is not a result of HBS formation. A logarithmic plot has also been fitted to this. This curve does not hold true for fuel burnups below the HBS formation threshold, neither above the range of experimental data.

The curve fitted to 3.2 is defined in equation 3.1.

$$f(x) = 0.308 + 4491.26 * e^{(-0.112*Bu)} \tag{3.1}$$

Where *Bu* is segment average burnup. The relationship described with equation 3.1 does not hold true below around 60 GWd neither above 100 GWd, however lack of data prevents further refinement.

There is however a trend evident in the data when lower burnup samples are considered. This suggests average fragment size may follow a linear regression when excluding the samples at higher burnups with large fragment

sizes, as shown in figure 3.3. The fragmentation observed at low burnups is however associated with thermal stresses [27], not burnup and so the curve defined in equation 3.1 has been chosen to estimate high burnup average fragment size and provides what appear to be reasonably accurate size predictions within the range of public data. There is however a large gap in fragment size data between burnups of 40 to 60 GWd (see figure 3.1). Data within this region would be especially valuable in more accurately predicting fragmentation as it may support the trend in figure 3.3.

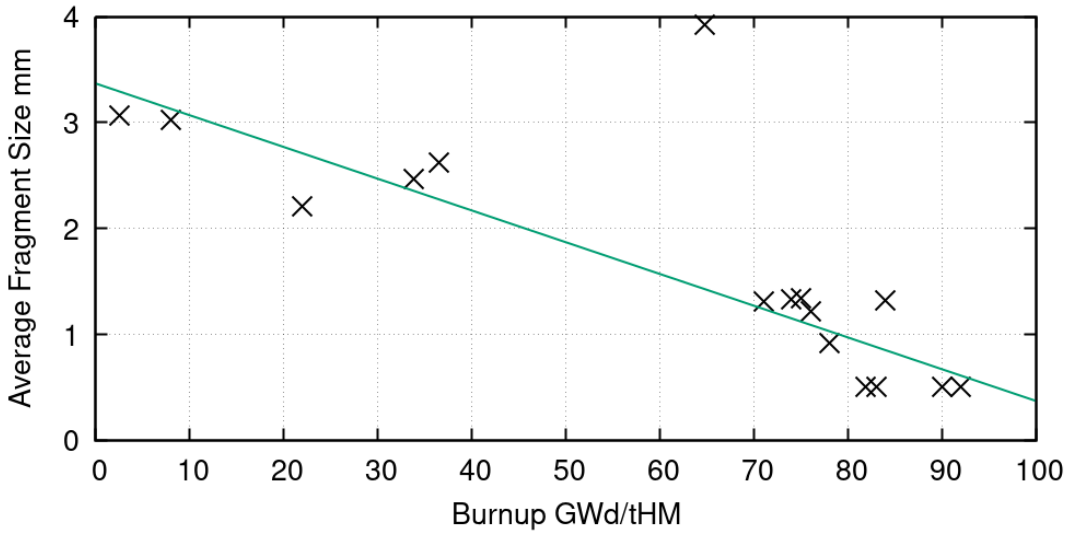

Figure 3.3: Average fragment size data with burnup, large fragment size samples (>4mm) with high burnup have been filtered as large fragments are not expected over about 60GWd.

Below 1 mm fragmentation has also been considered as fragments below this size are most likely to be mobile within a rod [26] and are more likely to be ejected from a rod in a burst due to their mass and size in relation to the burst size [14]. Data was also collated for the sub 1mm fragmentation fraction for publicly available data and is presented in table 3.2.

When plotted against burnup, the data in table 3.2 shows a clear point at which the pulverisation fraction begins to increase, this is in agreement with the model suggested by the US NRC [3], however it is also possible to calculate an estimate for average sub 1 mm pulverisation fraction equation, which was neglected by the NRC. This is given in equation 3.2.

Table 3.2: < 1 mm pulverisation fraction from LOCA tests from data in section 2.3.4.

Burnup GWd/tHM	**<1mm pulverisation Fraction**	**Test**
81.9	1	IFA-650.3
92	1	IFA-650.4
83	1	IFA-650.5
90	1	IFA-650.9
72.3	0.085	IFA-650.12
74.1	0.002	IFA-650.13
71.1	0.008	IFA-650.14
64.8	0.009	IFA-650.15
69.3	0.558	studsvik 191
68.2	0.666	Studsvik 192
69.3	0.577	Studsvik 193
55.2	0.019	Studsvik 196
55.2	0.030	Studsvik 198
74	0.495	NA#1
84	0.511	NA#2
71	0.453	HBR#1
2.56	0.026	FR-2 C
8	0.048	FR-2 E
21.91	0.109	FR-2 F
33.78	0.097	FR-2 G1
36.52	0.084	FR-2 G2
42.6	0.006	SCIP-III
60	0.201	SCIP-III
66	0.167	SCIP-III
64.4	0.322	SCIP-III
65	0.356	SCIP-III
66.3	0.563	SCIP-III
68	0.452	SCIP-III
70	0.163	SCIP-III
73	0.359	SCIP-III
74	0.205	SCIP-III
74.4	0.293	SCIP-III
76	0.327	SCIP-III
76	0.430	SCIP-III
74	0.652	SCIP-III

$$f(x) = 0.025 * Bu - 1.38 \tag{3.2}$$

Within the range 55 < *Bu* < 92 GWd/THm, 90% confidence bounds are presented in figure 3.4. A standard deviation of up to 0.5 is observed within the range 65 < *Bu* < 75 GWd/THm due to the large spread in data, notably some of the samples from Halden IFA-650. In general, the fragment size data from IFA-650 is relatively random however [38]. The most recent data from Studsvik SCIP-III falls far closer to the 95% confidence bound. Coarse data from higher burnup (> 80 GWd) Halden samples possibly overestimates < 1 mm pulverisation. Similarly to the average fragment size data in figure 3.2, lack of public data is detrimental to the accuracy of the equation. Values below 50 GWd have been excluded as small fragment formation in lower burnups is more likely a side effect of thermally induced crack formation, additionally the NRC model puts a starting point for 1 mm pulverisation at 55 GWd. The data from Halden is quite coarse, however is still valuable in understanding the extent of fine pulverisation given the limited amount of public data.

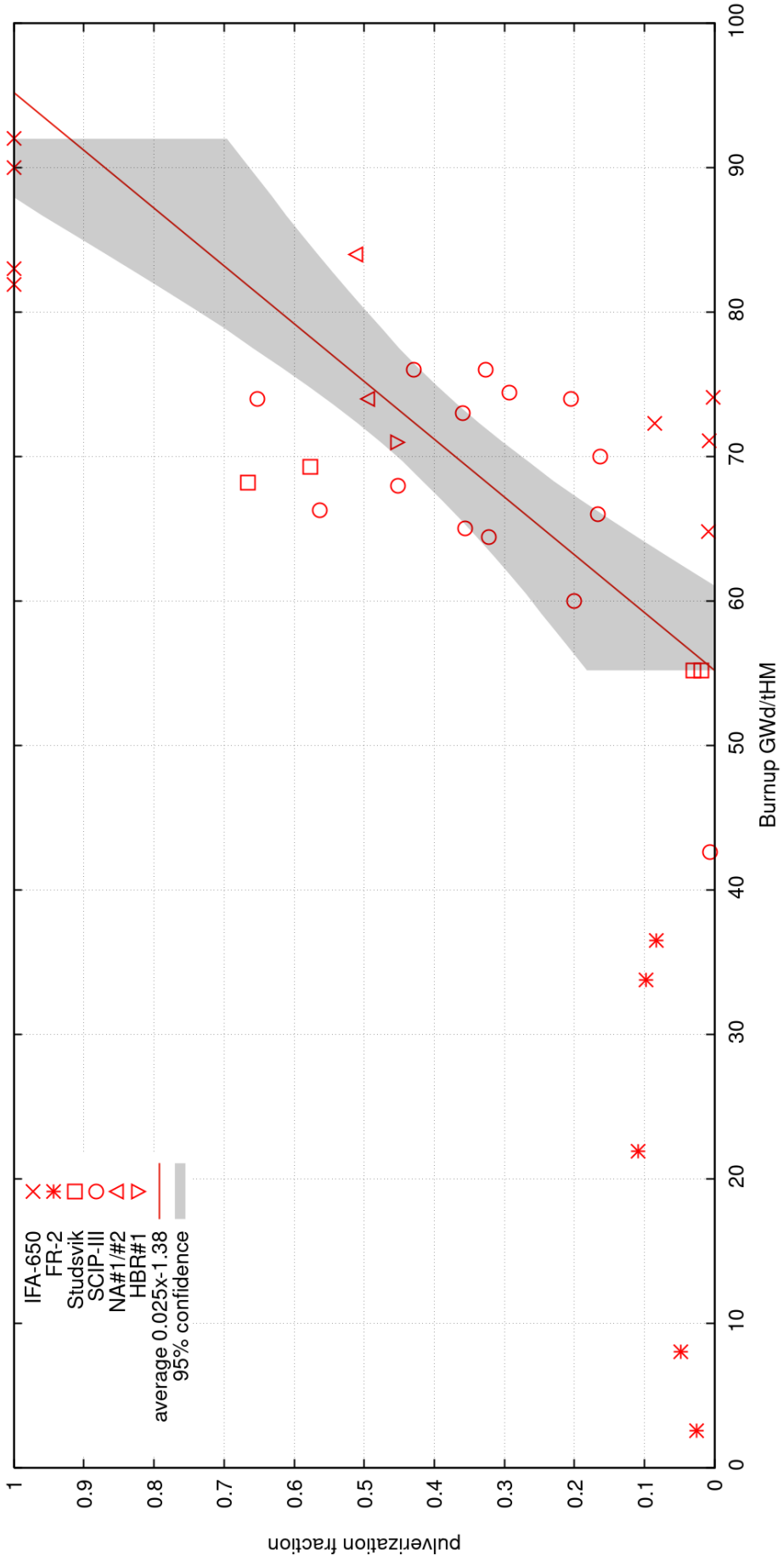

Figure 3.4: < 1 mm pulverisation fraction for table 3.2.

3.1.2 Implementation and Results

Using the data from figures 2.15 and 3.2, a simple empirical model for fragment size and pulverisation fraction was created using python. The model was designed to take burnup and temperature inputs from EDF UK's ENIGMA performance code and output predicted average fragment size and maximum pulverisation for each axial zone in the input. It can also be modified to include a true or false value for each zone reaching the Turnbull pulverisation threshold. The model's focus is identifying the risk of pulverisation rather than predicting it is taking place. It is indeed quite evident that until very high burnups there is little agreement between the maximum < 1 mm pulverisation fraction and the predicted fragment size, as shown in figure 3.5. The code loops over each axial (or radial) zone in each time step and calculates respective fragmentation values, these are outputted in a format shown in figure 3.7, optionally an average for each timestep can be calculated from the main output by using the the "-a" and "-A <file>" command line switches. The code also takes an argument for the pellet diameter, this is treated as the maximum possible fragment size for an axial zone.

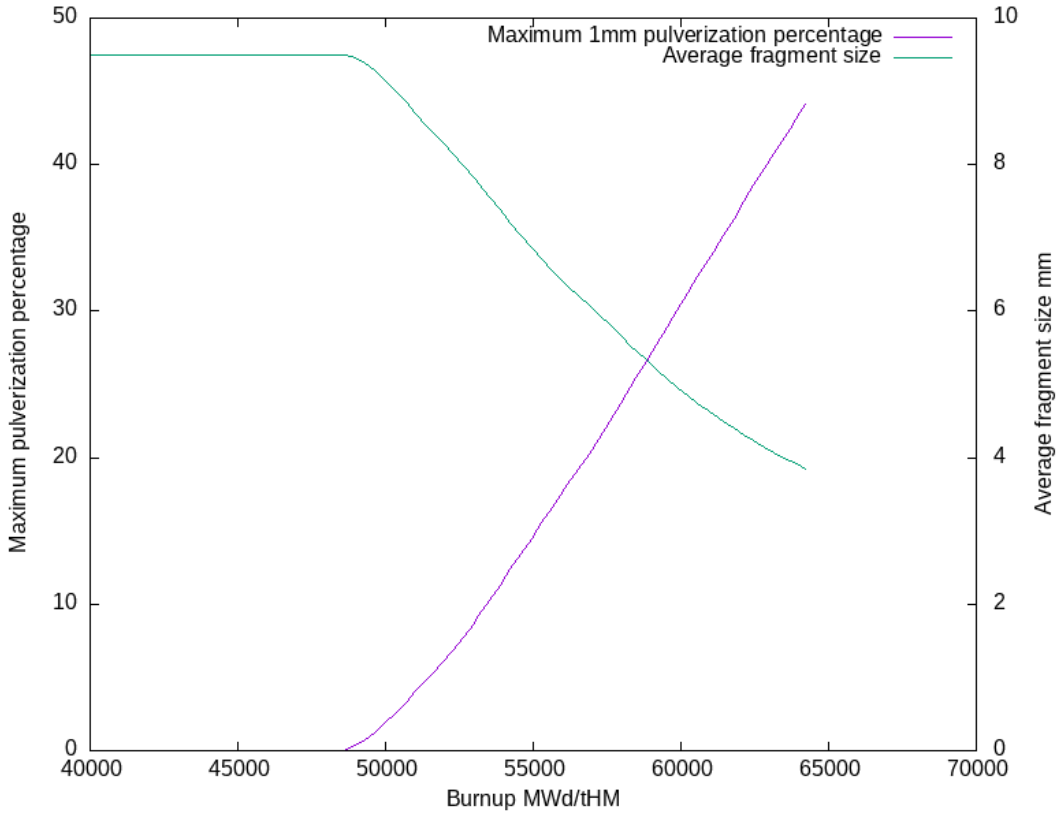

Figure 3.5: Maximum pulverisation fraction (pink) and average fragment size (green) for a test samples set up with power history conditions defined in table C.1.

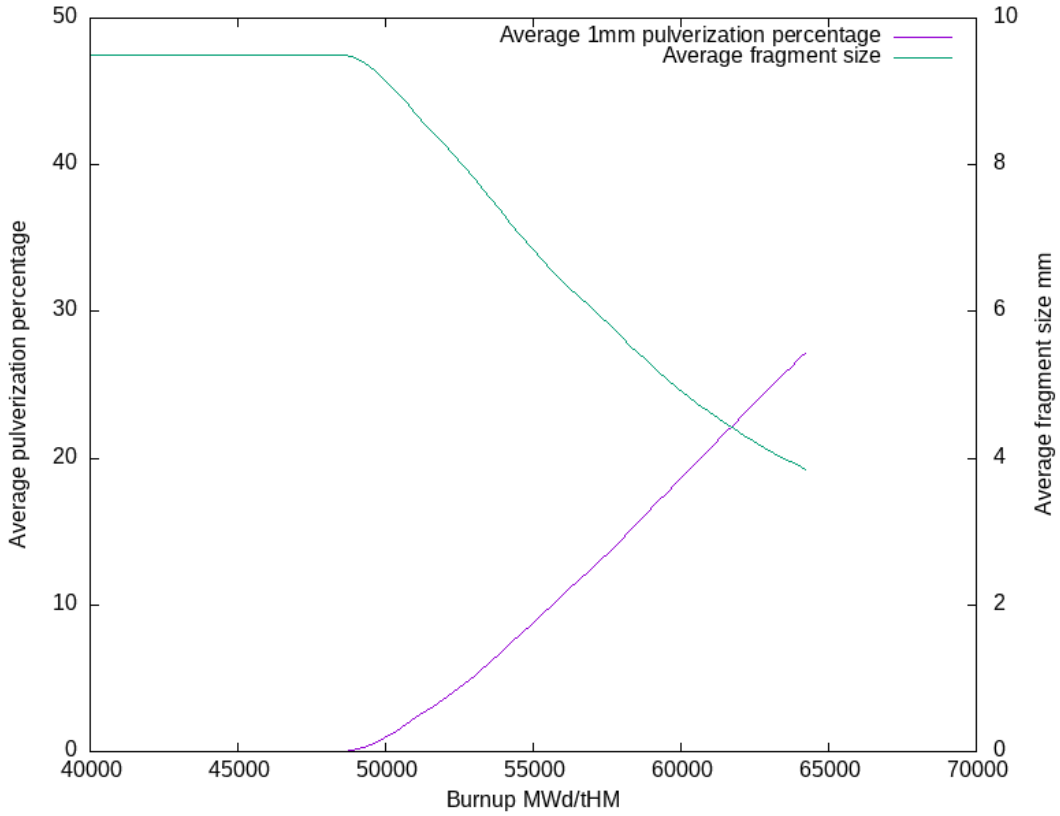

Figure 3.6: Average pulverisation fraction (pink) and average fragment size (green) for a test samples set up with power history conditions defined in table C.1.

```
STEP 29-
SUB-STEP 2
END OF STEP HOURS: 32304.0
BURNUP MWd/tU   TEMPERATURE   PULV-FRAC-SUB-1MM   AVR-FRAG-SIZE-MM
48342           978           -0.0                9.5
66925           1263          29.31               2.8
70563           1229          38.41               1.97
71143           1190          39.86               1.86
70968           1174          39.42               1.89
70414           1181          38.04               2.0
69643           1214          36.11               2.15
67971           1267          31.93               2.53
62687           1302          18.72               4.32
43344           990           -0.0                9.5
64200.0                       27.18%
```

Figure 3.7: Snippet from the full output file from the code used to produce figure 3.6. The command used to produce the file with these headings was: fragmentation_model.py -i case.txt -a -o outfile -A avgoutfile -f -d 9.5

The pulverisation fraction line in figures 3.5 and 3.6 show the maximum and average pulverisation respectively. In both graphs the same average fragment size curve is present. The maximum pulverisation fraction for the test run predicted in figure 3.5 is high when compared to the average fragment size predicted. However when an average pulverisation fraction is considered rather than the maximum, in figure 3.6, a lower value of around 30% is estimated when the average average fragment size is just under 4mm. If the end axial zones in the rod are ignored, which have not reached a burnup high enough to pulverize, an estimate that better matches experimental data is attained; 33% < 1 mm pulverisation for an average fragment size of 2.4 mm. The burnups achieved in this run are not very high, and so do fall within a region of more uncertainty for the average fragment size. Despite this, when compared with SCIP-III experiments of similar burnups (64-65 GWd/tHM), the pulverisation fraction closely matches the observations (see table 3.2). The average fragment size possibly falls between 2 and 3 mm if using figure 2.14 as a distribution reference, as these samples also have fragment mass fractions for fragments below 2mm of around 43% [3]. More data to confirm the relationship in any more detail is not publicly available.

3.2 Mechanistic Model

There are a number of models that have been proposed for simulating and understanding the causes and onset of fragmentation. Some of these rely on phase field simulations for brittle fracture, such as one proposed by Jiang et al. [28], others rely on fuel rod performance programs, such as FRAPCON [27]. The model chosen here is less complex and makes use of an equation of state to calculate gas pressures in bubbles, with their overpressure leading to fracture. This model is described by K. Kulacsy [32]. This has been chosen as its implementation is relatively simple, and boundary conditions can be provided where necessary from ENIGMA, with the potential for the entire model to be added to ENIGMA should it provide useful fracturing data. Heating rate is entirely neglected within this model, however it is observed that there may be a threshold heating rate, above which bubbles cannot relax internal gas pressures through growth, making bursting far more likely. This may be evident through significantly increased FGR at heating rates over $90\,^{\circ}\mathrm{C\,s^{-1}}$ for high burnup samples [65].

3.2.1 Background

The model as described by Kulacsy [32], relies on equations for gas pressures in bubbles, material properties including stresses and strains, and Ronchi's equation of state for rare gases [51]. Much of the following is reproduced from Kulacsy's paper.

Kulacsy defines a threshold at which fracturing of the material is expected to take place, where the fracture strength, σ_f, is exceeded by the tangential stress on the surface of a gas bubble, σ_t.

$$\sigma_t > \sigma_f \tag{3.3}$$

Where σ_f and σ_t are both in MPa.

The fracture strength of UO_2 is defined in [17] with equation 3.4

$$\sigma_f = \begin{cases} 1.7 \times 10^8 * (1 - 2.62 * (1 - D))^{\frac{1}{2}} e^{-\frac{1590}{8.314*T}} & \text{for } 273 < T <= 1000\text{K}, \\ 1.7 \times 10^8 * (1 - 2.62 * (1 - D))^{\frac{1}{2}} e^{-\frac{1590}{8.314*1000}} & \text{for } T > 1000\text{K} \end{cases} \tag{3.4}$$

where σ_f is fracture strength in Pa, D is the fraction of theoretical density and T is temperature in Kelvin. Kulacsy rearranges this equation in the form presented in equation 3.5, D is replaced with φ representing the porosity fraction.

$$\sigma_f = \begin{cases} 170 * exp(-\frac{191.34}{T}) * \sqrt{1 - 2.62\varphi} & \text{for } T <= 1000\text{K}, \\ 170 * exp(-\frac{191.34}{1000}) * \sqrt{1 - 2.62\varphi} & \text{for } T > 1000\text{K} \end{cases} \tag{3.5}$$

Typical values for normal operating conditions fall around 115 to 125 MPa (625 K and 5% porosity gives a value of 116 MPa), this was checked against porosity dependant fracture strength values presented in [41], see figure 3.8. These samples were analysed at room temperature and did not include a temperature dependence, however the magnitude of values calculated is very similar.

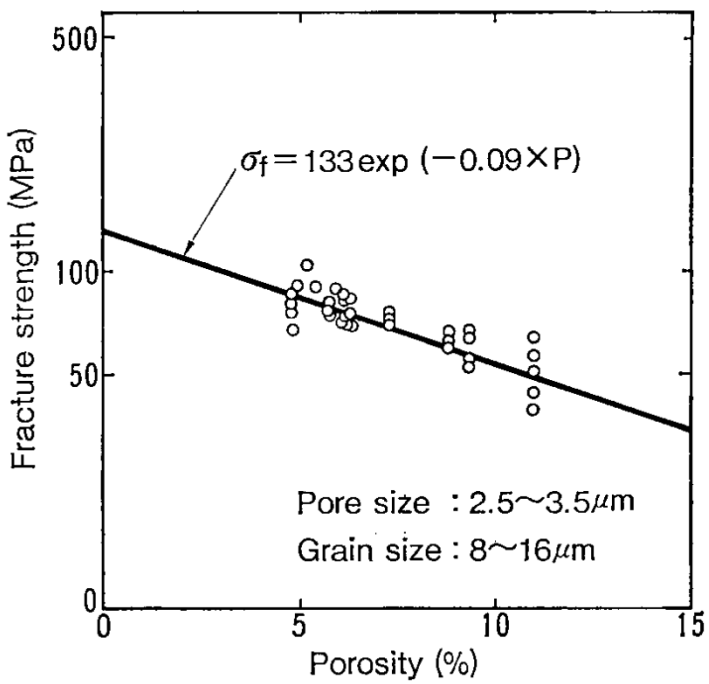

Figure 3.8: Porosity dependant fracture strength used for validation of equation 3.5. Sourced from [41].

For fracturing to take place, gas bubbles formed in the UO_2 should overpressure and burst. The point at which they burst is dependant on the fracture resistance of the UO_2, impacted by its porosity and temperature. The equilibrium (steady state with no bubble growth) pressure for a gas bubble in UO_2 is defined by equation 3.6 [4].

$$p_{eq} = p_h + \frac{2\gamma}{r} \tag{3.6}$$

Where p_{eq} is calculated in MPa, p_h is the hydrostatic (external) pressure in MPa, and r is the pore radius in μm. The porosity and temperature dependant surface energy, γ is in J/m^2 and given by combining the porosity and temperature dependant surface energy calculations into equation 3.9. It is noted that the surface energy in pores is 0.41 times the free surface energy [18][44], and has an inverse linear relationship with temperature.

$$\gamma_T = 0.85 - 1.4 \times 10^{-4} * T \tag{3.7}$$

$$\gamma_p = \gamma_T * (1 - \varphi)^{4.025} \tag{3.8}$$

$$\gamma = 0.41 * \gamma_p \tag{3.9}$$

When plotted against porosity in figure 3.9, it is evident that porosity fraction far more significantly impacts surface energy than the temperature of the material.

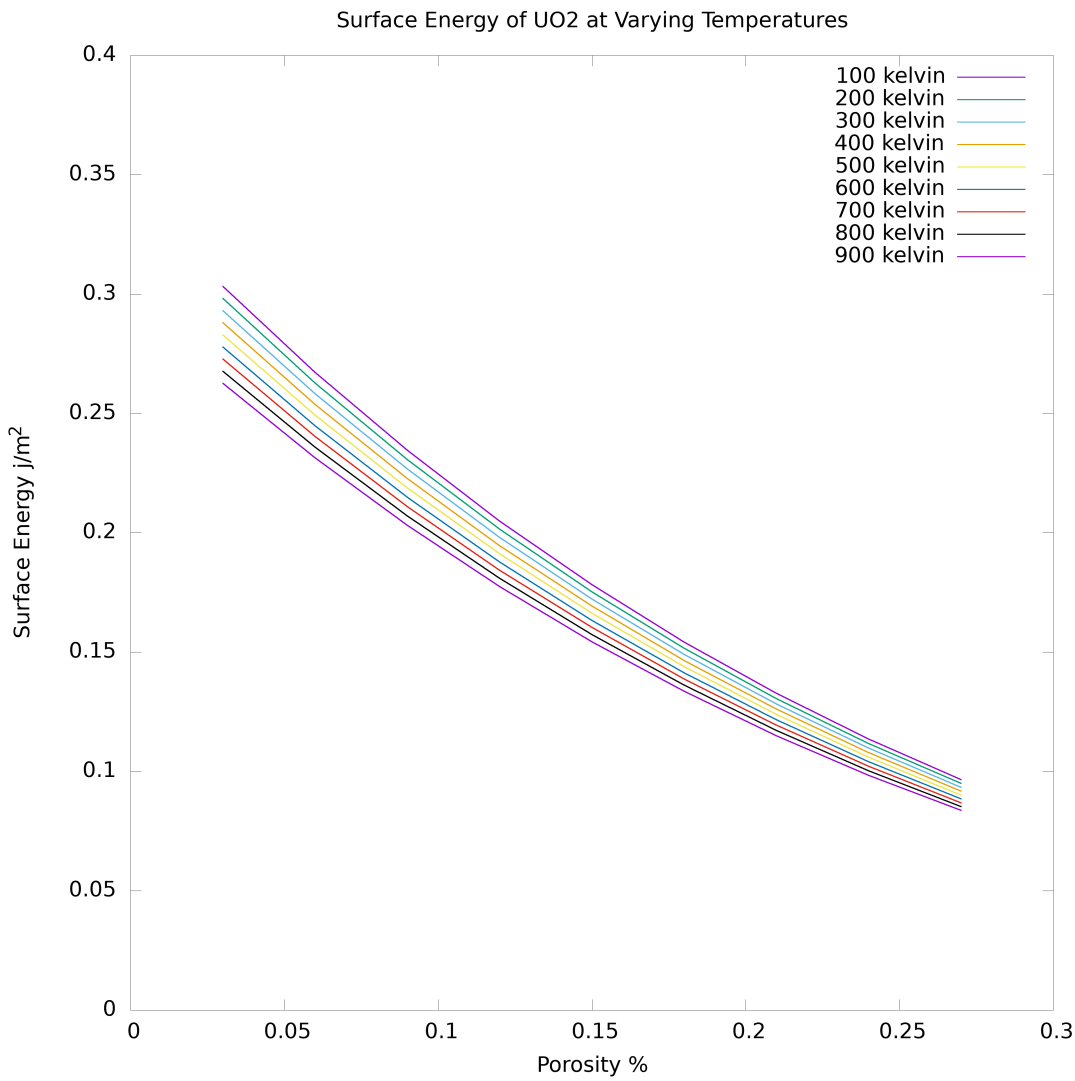

Figure 3.9: Surface energy for UO_2 for porosity fractions from 5% to 27% as calculated with equation 3.9.

The minimum excess pressure within a gas bubble required to drive bubble growth through dislocation formation is given by equation 3.10 (sometimes referred to as dislocation punching pressure).

$$p_{ex} = \frac{Gb}{r} \tag{3.10}$$

Where p_{ex} is calculated in MPa, b is the burgers vector of UO_2, given as 0.39 nm in [43], and r is the bubble radius. G, the shear strength, is given by equation 3.11.

$$G = \frac{E}{2 * (1 + v)} \tag{3.11}$$

Where G is calculated in MPa. v, Poisson's ratio is dependant on porosity, given by equation 3.12.

$$v = 0.32 - 0.34\varphi \tag{3.12}$$

E, Young's modulus in MPa is dependant on temperature and porosity and given by equation 3.13.

$$E = 2.334 \times 10^5 * (1 - 1.0915 \times 10^{-4} * T) * (1 - 2.752\varphi) \tag{3.13}$$

A gas bubble can sustain a maximum pressure, p, under normal operation, given by equation 3.14. A higher pressure is expected to be relieved through bubble growth.

$$p = p_{eq} + p_{ex} \tag{3.14}$$

In order to determine the tangential stresses at the bubble surfaces during transients Kulacsy provides equation 3.16 for calculating the tangential stress at the bubble surface.

A basic definition for surface stress in a pore is given in [44] as equation 3.15.

$$p_0 = \sigma_t = \frac{2\gamma}{r} - p \tag{3.15}$$

where p is the gas pressure in the pore.

Equation 3.16 describes the tangential stress at the bubble surface during heating, this is applicable for any pressure within the bubble. Equation 3.17 calculates the tangential stress at the bubble surface assuming that the bubble is at its maximum overpressure prior to growth, given in equation 3.14.

$$\sigma_t = p - (\frac{3}{2}p_h + \frac{2\gamma}{r}) \tag{3.16}$$

$$\sigma_t = \frac{Gb}{r} - \frac{1}{2}p_h \tag{3.17}$$

Where σ_t is calculated in MPa, P_h the external hydrostatic pressure is in MPa, and r is the pore radius in μm.

For this work, equation 3.16 has been chosen as it provides a gas pressure threshold above which the bubble will burst, satisfying the condition in equation 3.3. Equation 3.17 provides values for which bubble growth will occur.

In order to determine the gas pressures in the bubbles during heating, an equation of state is required. A natural choice would be the ideal gas law, however Kulacsy notes that it indicates high gas content for high pressures resulting in very high gas release when the bubbles burst, higher than experimental results indicate. Kulacsy chooses Ronchi's EOS, which is provided in a tabulated form requiring interpolation between values, as it provides lower gas volumes for higher pressures.

3.2.2 Implementation

The minimum gas pressures required to cause bubble bursting for fuel with various porosity fractions and temperatures can be determined by rearranging equation 3.16, into the form given in equation 3.18.

$$p_b = \sigma_t + \frac{3}{2}p_h - \frac{2\gamma}{r} \tag{3.18}$$

Where σ_t is determined with equation 3.4, as the fracture strength for the fuel in the given state.

Equation 3.18 can be used with data on porosity fractions in relation to burnup to determine the pressures bubbles can safely reach at different operational temperatures without bursting. Figures 3.10 to 3.12 show the impact of bubble size, porosity and temperature on the minimum bubble gas pressures required to cause fracturing.

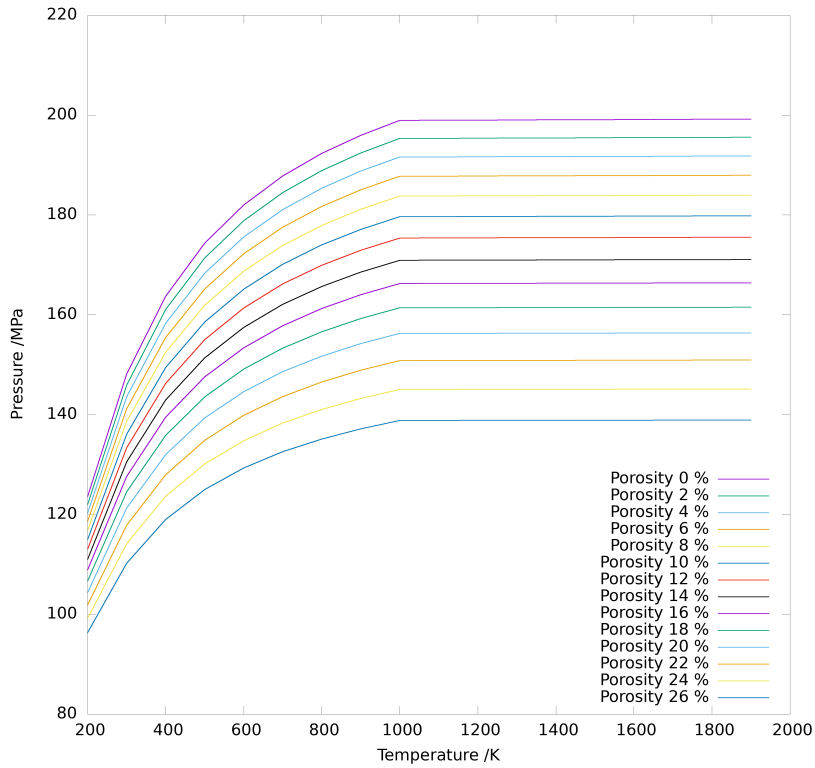

Figure 3.10: Minimum gas pressure in a 0.4 μm bubble required to cause bursting as a function of temperature and porosity.

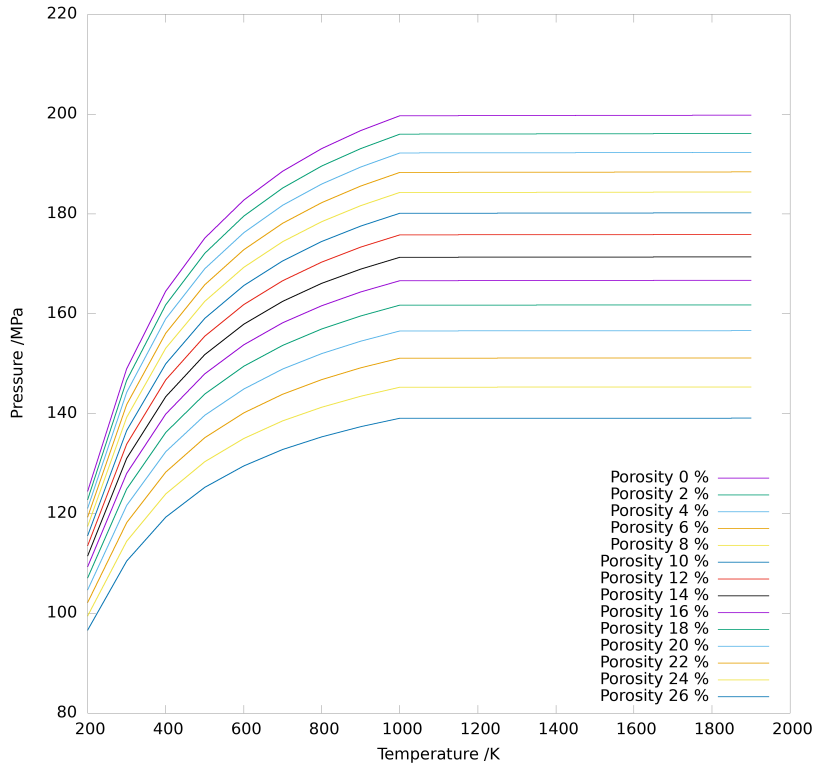

Figure 3.11: Minimum gas pressure in a 0.8 μm bubble required to cause bursting as a function of temperature and porosity.

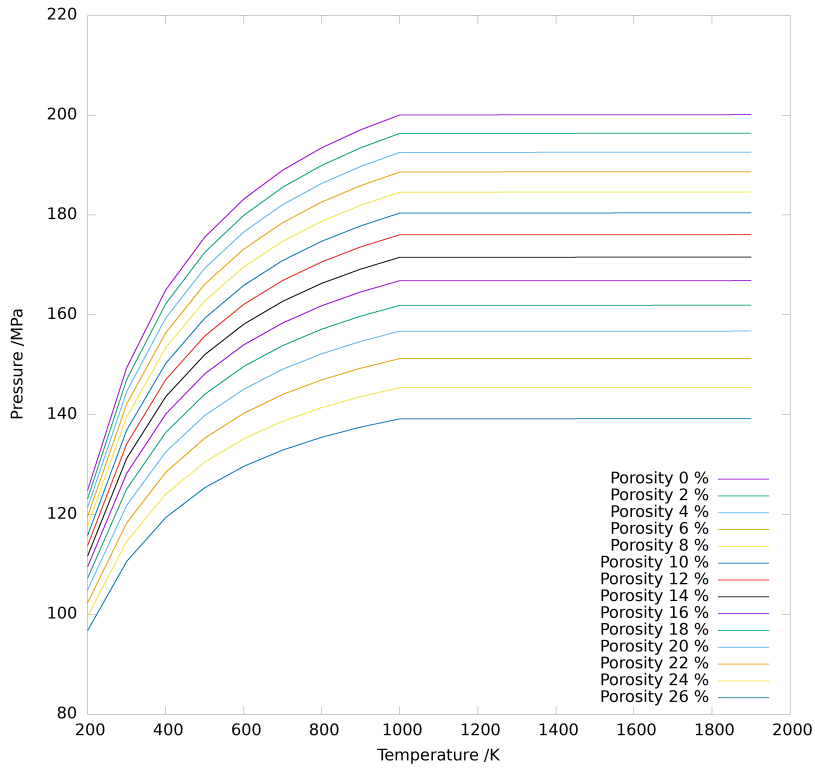

Figure 3.12: Minimum gas pressure in a 1.6 μm bubble required to cause bursting as a function of temperature and porosity.

Ronchi's equation of state for rare gases [51] provides a tabulated form for determining the gas pressure in a bubble during heating. The steady state gas pressure for a bubble size at a given temperature can be calculated with equation 3.6. This pressure can then be used to find the molar volume for the gas in Ronchi's EOS and, assuming no more gas is added to the bubble, nor any bubble growth takes place, the pressure during fast transient heating retrieved from the table. The bubble burst is assumed to take place when the following condition is met:

$$p_s > p_b \tag{3.19}$$

Where p_s is the calculated gas pressure from the equation of state, and p_b is the minimum pressure for bubble burst calculated in equation 3.18.

Porosity is expected to increase with burnup, as demonstrated in ref [53][56]. Intragranular Pore size increases with increasing radial position towards the pellet periphery [25], as burnup is shown to increase towards the pellet rim [2], and pore size is shown to be dependant on fuel burnup [30]. Intragranular

bubble sizes are expected to increase with burnup, the fraction of gas within the pellet contained in these bubbles is expected to remain fairly consistent [59]. Very little data is available in public literature of pore size distributions, Ronchi provides a number of distributions from varying observation types [50] however these are distributions of bubble size over an entire sample with no consideration of burnup or radial position.

Ronchi's equation of state provides a reliable prediction for gas pressures during a temperature increase, however in its tabulated form it is in the wrong format for the lookups required (requiring interpolation between 4 pressure values). Another EOS that is commonly considered in literature is Van der Waals, though it is generally accepted that Ronchi's EOS is more accurate for Xe bubbles in nuclear fuels [70][32]. The Carnahn-Starling EOS can also offer an approximation of pressure values, and has undergone revisions to improve accuracy. However, There is notable disparity between experimental data and common equations of state, such as Ronchi, Van der Walls and Carnahan-Starling, for small highly pressurized bubbles, and indeed between the different EOSs themselves as seen in figure 3.13. Additionally, these equations of state neglect interactions with bubble faces, the gas/matrix interface, that may have a crucial impact the behaviour of highly pressurized xenon [22]. Therefore for this current project LAMMPS was used to calculate gas pressures to purely rely on simulation, although the interface between gas and crystal matrix was also neglected. A sensitivity analysis was not carried out as it was beyond the scope of the project. 6000 xenon atoms were simulated with periodic boundaries, in an initial volume of 3063 cm^3/mol which was heated from 300K to 2000K. The volume was decreased linearly from the initial down to 100 cm^3/mol by shrinking the boundary lengths of the box from 312.5 Å to 100 Å. With the steady state temperature and pressure known, along with the volume of the gas bubble, the pressure during heating can be determined similarly to the method with Ronchi's EOS. The input file for LAMMPS is included in Appendix D.

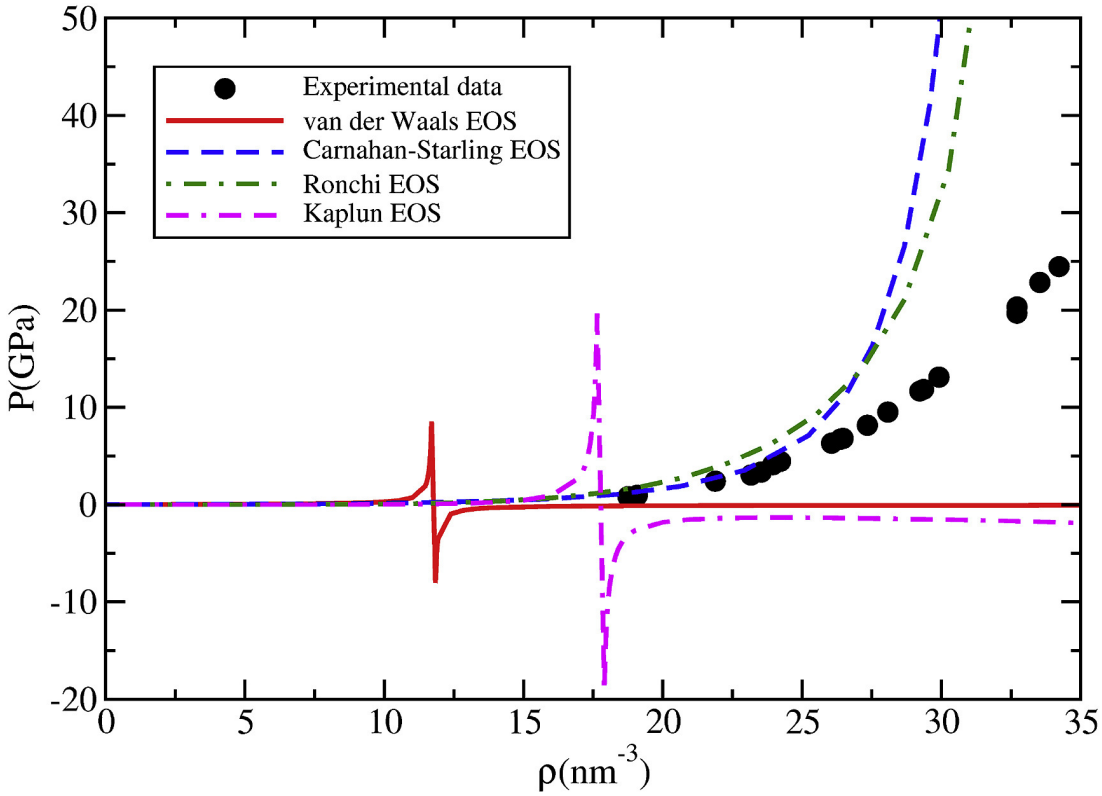

Figure 3.13: Pressure/Density comparisons for high gas pressures for noble gases as calculated by common EOSs compared with experimental data. Sourced from [21]. Both Van der Walls and Kaplun predict non-physical behaviour in very small bubbles not too indifferent in size from those considered in this work, and Ronchi and Carnahan-Starling predict exponentially higher pressures than experimental results as densities increase.

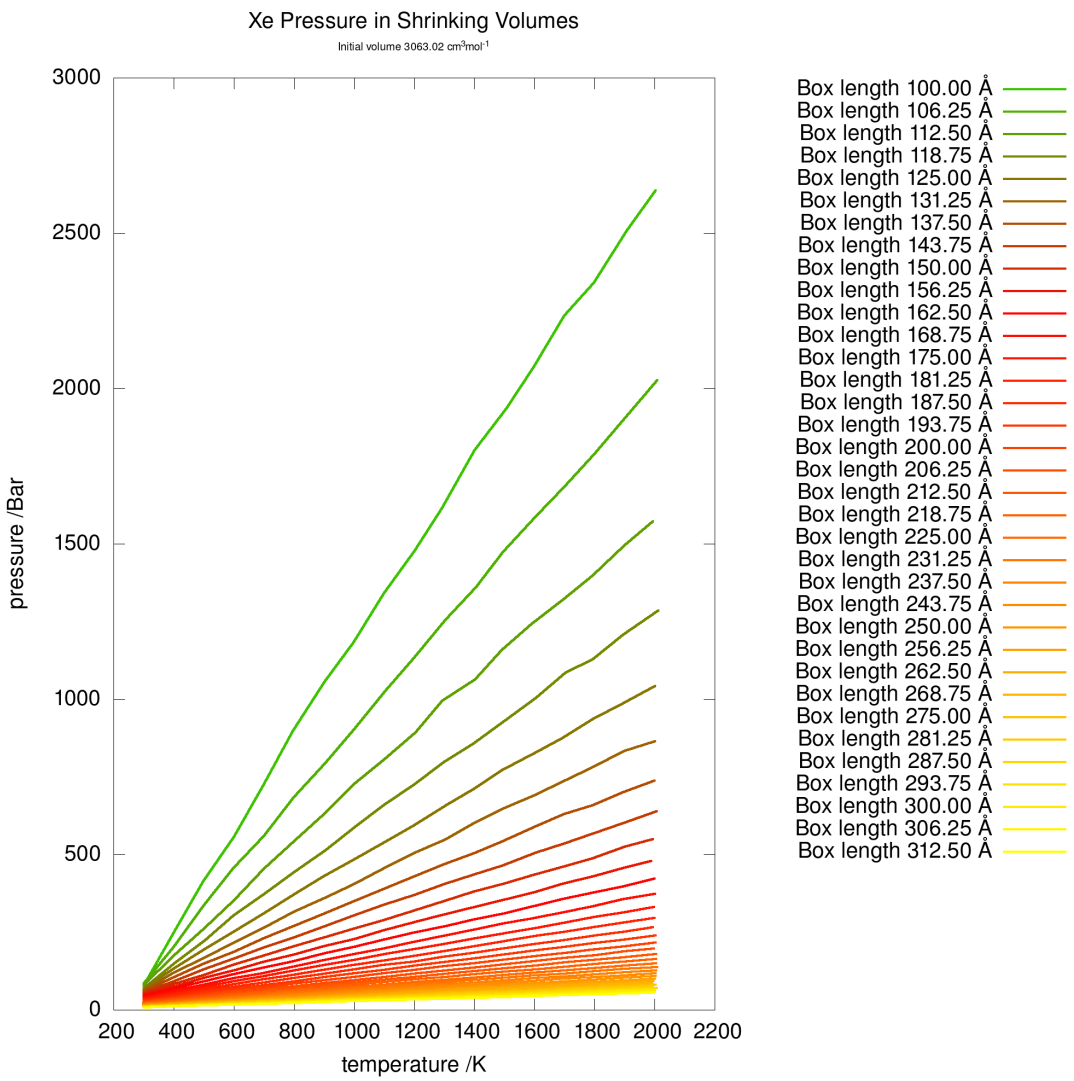

Figure 3.14: Calculated gas pressures for xenon in volumes from 3063 to 100 cm^3/mol. The side lengths for the shrinking box are given in angstroms for each run.

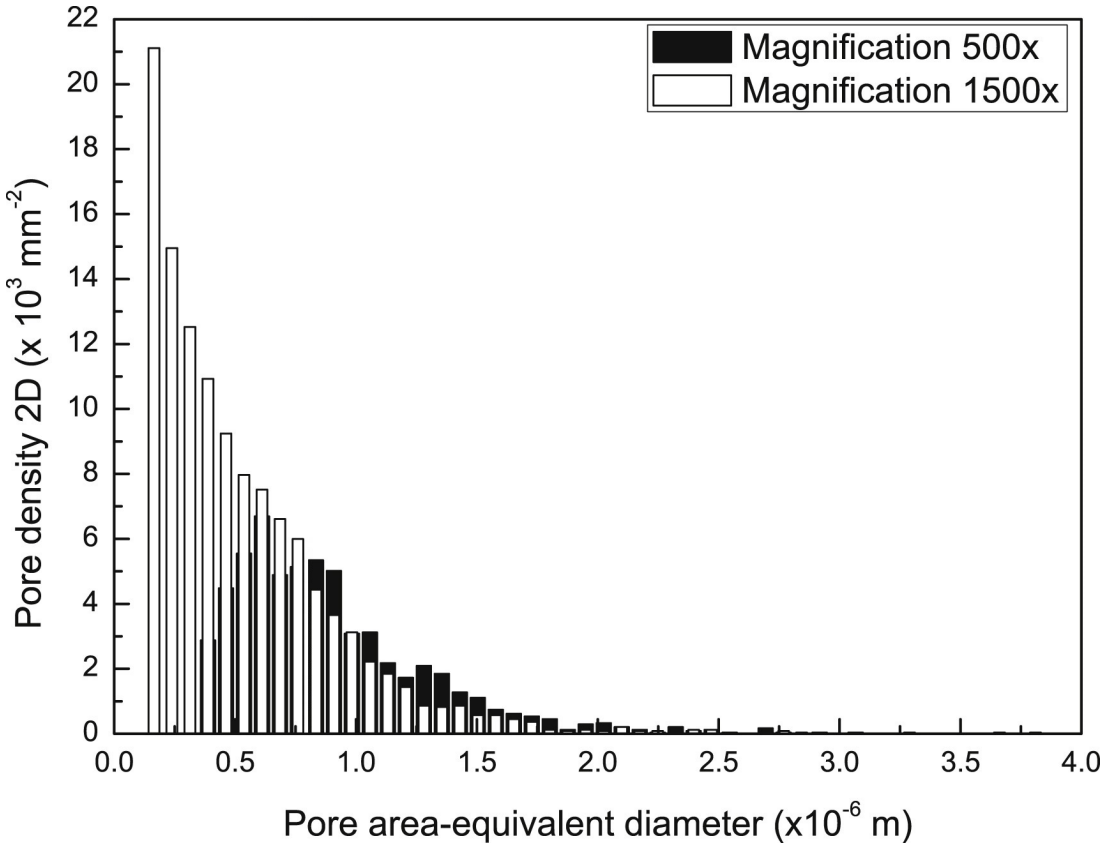

Figure 3.15: Bubble size distribution in the rim region of 67 GWd/tHM fuel, with a calculated local burnup of 82 GWd/tHM. Adapted from [9].

With gas pressures, a known bubble distribution, irradiation temperatures and porosity faction, the percentage of bursting bubbles can be calculated, which can provide a predictor as to the onset of fragmentation. Ref. [9] provides a number of bubble size distributions for pellet rim regions at very high local burnups (>100 GWd). The paper also suggests distributions follow a log normal curve, but does not provide values for terms. Kulacsy provides pore distribution graphs for $r/r_0 = 0.9$ and $r/r_0 = 0.98$. These distributions are broadly similar to the one picked in figure 3.15. Local burnup is lower at 82GWd in the example chosen. The distribution does suggest a larger proportion of smaller bubbles than Katalin's. Values from the distribution in figure 3.15 have been used in the following example in order to apply the model on fuel irradiated under different conditions to that used by Kulacsy, and that is closer in average burnup to end-of-life fuels from reactors. Kulacsy presents FGR fraction for her distributions, which is not directly comparable to the calculations below, however more bubbles are shown to be bursting at lower temperatures than using the distribution in figure **??**.

Irradiation parameters are provided in [9]. The restraint pressure was 8 MPa, temperature was $620\,°$C, porosity fraction was measured at 5% and the distribution only covers the very outer rim region $r/r_0 = 0.95$. The present model has been applied to a bubble size distribution curve fitted to figure 3.15 with equation 3.20.

$$f(x) = 17.3 + 26955.5e^{-2.2*d} \tag{3.20}$$

As both sides of the equation 2.3 are temperature dependant, the burst point during heating is a crossover between the 2 lines in figure 3.16, an example for a 0.48 µm radius pore with the conditions described above. A constant temperature increase from 600K has been used to simulate a transient. No bubble growth is occurring during the transient.

Assuming the bubble is at its maximum pressure before growth, 67.3 MPa, the tangential surface stress under the above restraint conditions at 600K is 54 MPa. During a transient the stress follows the green line in figure 3.16.

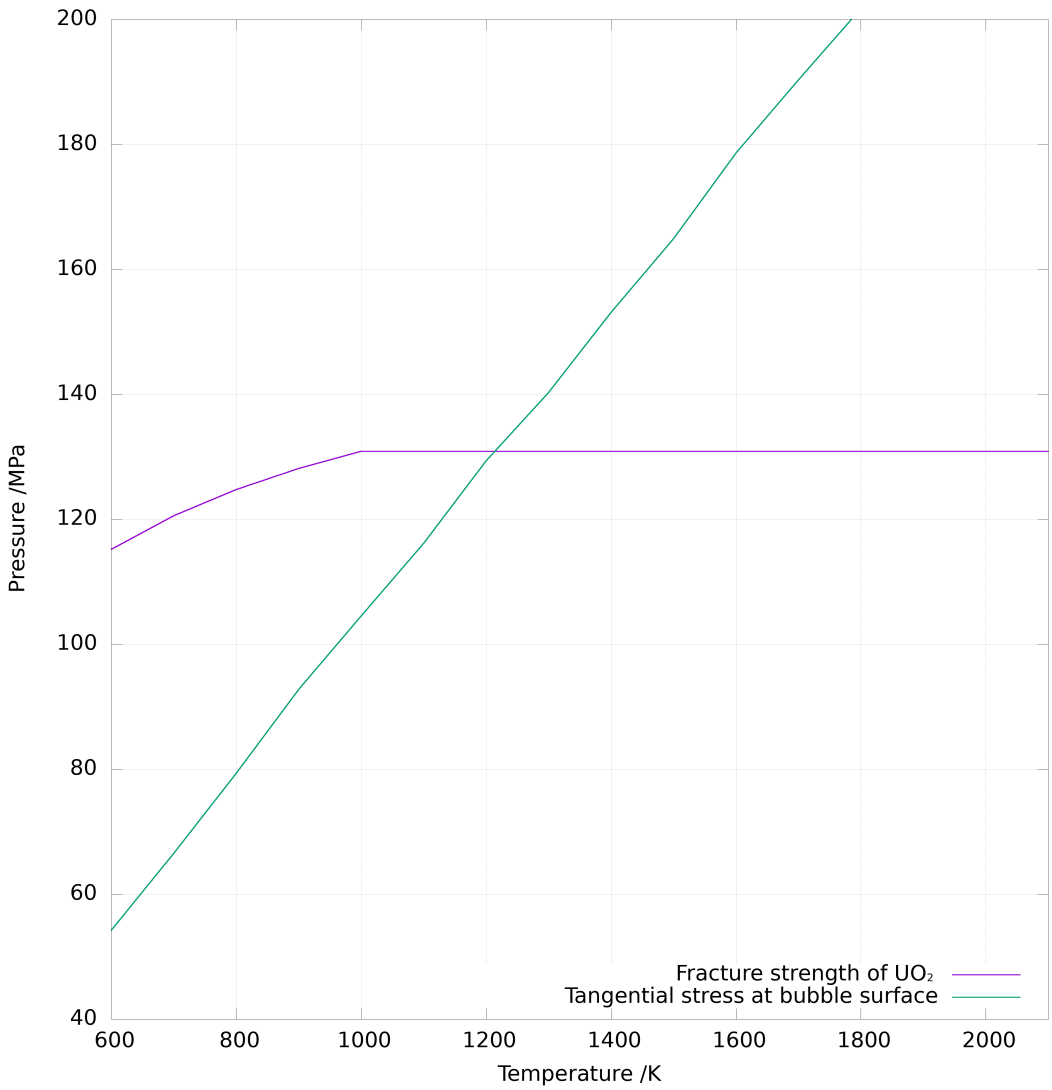

Figure 3.16: The tangential stress at the surface of a 0.48 µm bubble compared to the calculated fracture resistance of UO_2 using equation 3.4. The point at which both lines cross is the temperature at which a 0.48 µm fully pressurized bubble will burst. Similar relationships can be applied across a bubble distribution to get a fragmentation fraction for a given temperature.

For a 0.24 µm radius bubble under the same restraint conditions, the tangential surface stress at 600K is 113.2 MPa.

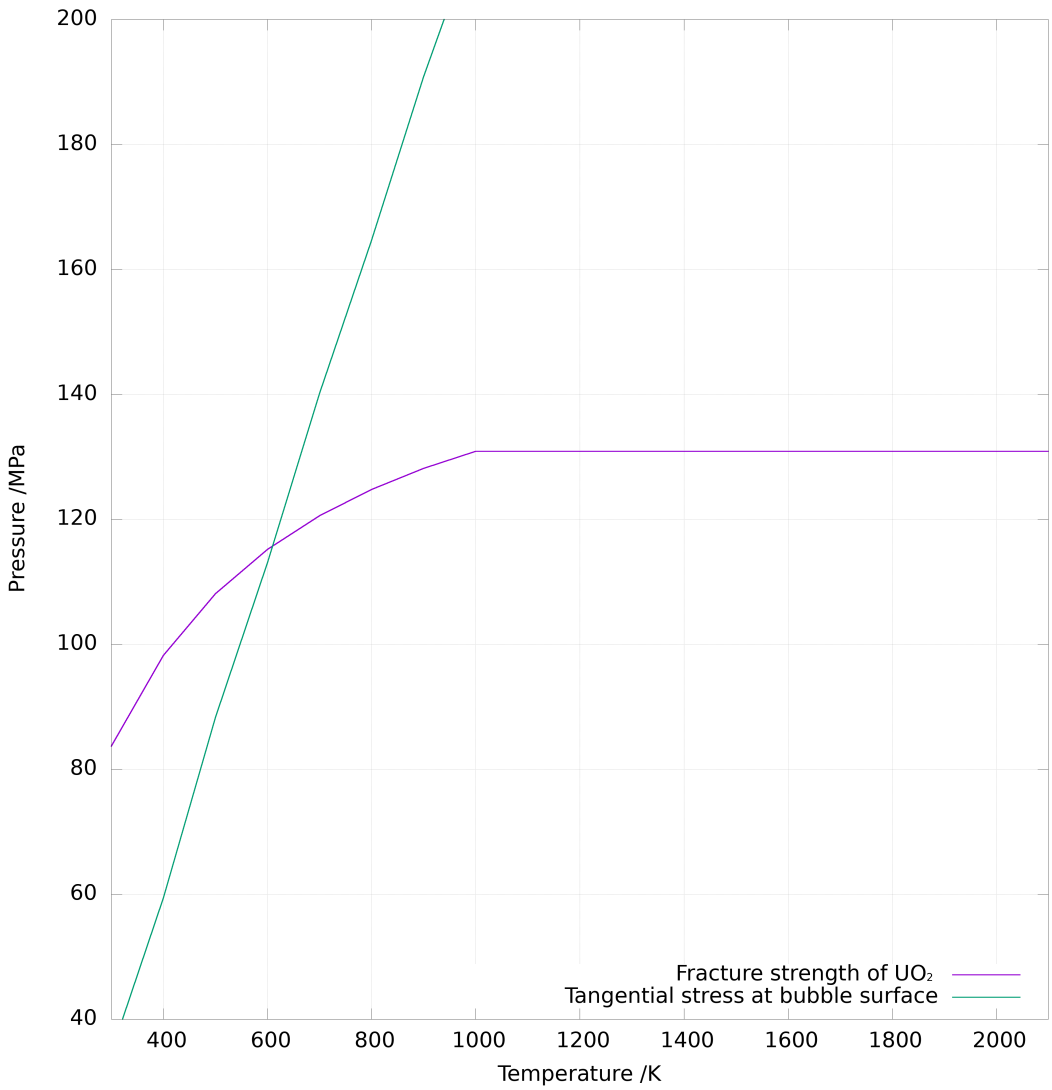

Figure 3.17: The tangential stress at the surface of a 0.24 μm bubble compared to the calculated fracture strength of UO_2, with 5% porosity.

For a 1 μm radius bubble under the same restraint conditions, the tangential surface stress at 600K is 24 MPa.

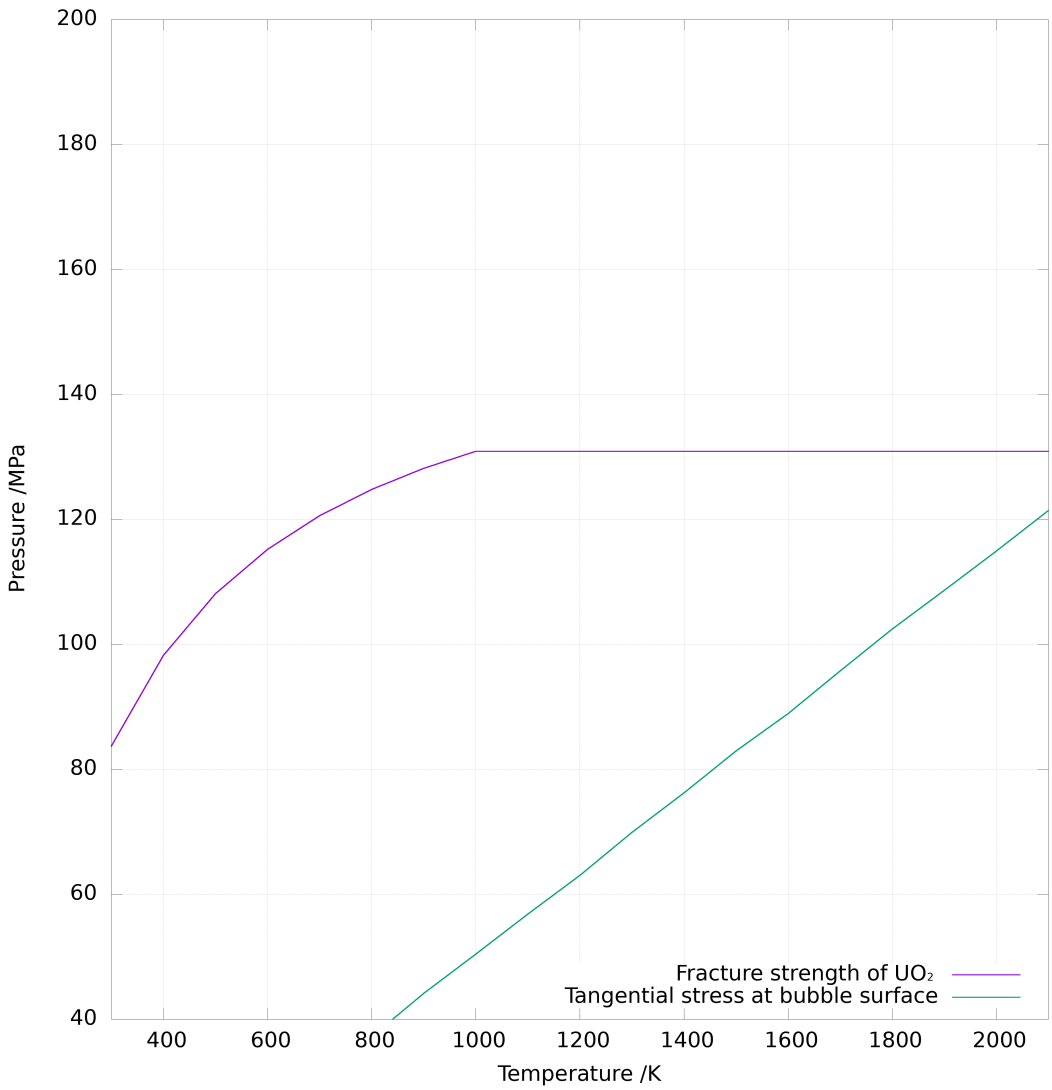

Figure 3.18: The tangential stress at the surface of a 1 μm radius bubble compared to the calculated fracture strength of UO_2. Note that the bubble is not expected to burst until temperatures exceed 2100 K.

If the data from figures 3.17, 3.16 and 3.18 are used with the bubble distribution equation 3.20, a coarse estimate for a pulverisation risk can be calculated. For this example, the transient terminal temperature will be 2000K.

100% of bubbles below a diameter of 2 μm are expected to burst (it will be slightly lower than 100% due to 1 μm radius bubbles not bursting until around 2300 K, however this coarse estimate cannot factor this) , no bubbles with diameters above 2 μm are expected to burst in the transient. Integrating the distribution in figure 3.15 between 0.1 μm and 4 μm, and subtracting the integration between 2 μm and 4 μm, predicts 98% of bubbles within the

region $r/r_0 = 0.95$ would burst in a transient reaching 2000 K. This value could be refined by sampling the bubble burst parameters at more than 3 points on the curve. Figure 3.19 shows the temperatures and pressures at which bubbles of different sizes will burst for UO_2 with 5% porosity and with an 8 MPa restraint pressure. While it is evident that both temperature and bubble radius have an impact on the pressures required for bursting to take place, there is a maximum pressure that can be sustained of around 160MPa under normal operating conditions (T >= 625K) for all bubbles with radii greater than 0.1 μm as the surface plateaus rapidly in both temperature and radius axis. For larger bubble radii (r > 1 μm) the transient temperature has a far more significant impact on their ability to withstand internal gas pressures than the radius

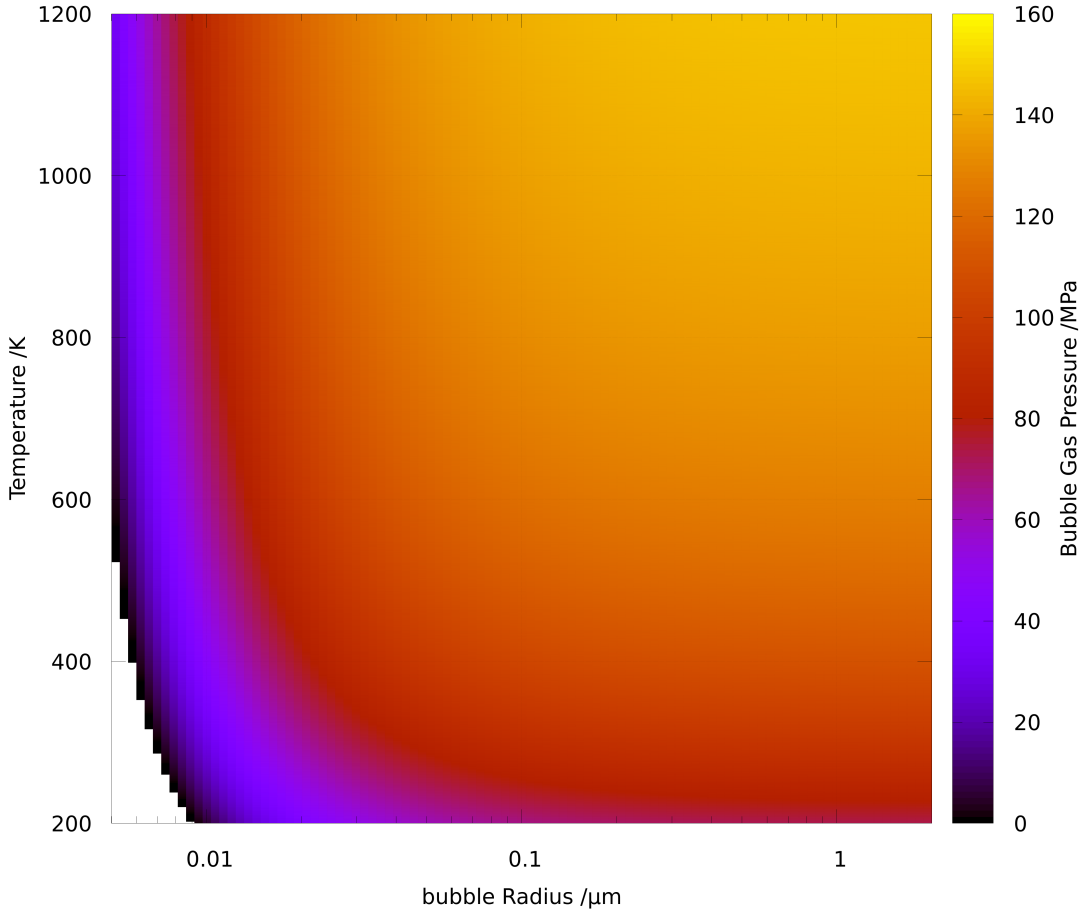

Figure 3.19: Minimum bubble gas pressure required to cause a bubble to burst at a given temperature and for a bubble radius. The section of the heatmap in the bottom left with no values implies bubbles of very small radius cannot form at low temperatures. Note that the bubble radius axis is logarithmic.

3.2.3 Discussion

The value for surface energy has significant uncertainty. The energy of free surfaces has uncertainty of up to 70% [18], which is expected to be even greater when calculating the surface energy for pores. This may go some way in explaining the discrepancy between calculations for γ in different publications. With this uncertainty considered, the Young-Laplace equation, regularly used to describe the equilibrium pressure within pores, also loses accuracy. The Young-Laplace equation may not be best suited for the calculation of bubble pressures in solids as it is designed to be applied in

liquids. The surface energy value is as mentioned significantly variable for UO_2, but the equation also neglects any reference to higher energies needed for a bubble to form in a solid. Compared to a liquid where for a bubble to form and grow it simply needs to push atoms out of the way, in a solid ceramic with very little ability to undergo plastic deformation, other mechanisms such as defect diffusion into the bubble and irradiation will impact the evolution of a bubble, as well as the energy required to form dislocations in the surrounding matrix [16]. Additionally local defect concentration will impact the resistance of the surrounding ceramic to bubble growth. Some literature suggests that the surface energy term should be replaced with a surface stress term where the interface is a fluid-solid boundary [20][47], showing good increases in accuracy of pressure calculations. There is also the suggestion that the Young-Laplace equation is invalid for very small highly pressurized bubbles [47].

It is evident that there is link between gas bubbles bursting and the onset of fragmentation in HBS. Literature generally accepts the suggestion that very fine fragmentation is a result of gas bubbles bursting [27][24][65], and there is evidence of significant fission gas release at the point of fragmentation occurring. Experimental results also show that significant fission gas release and fragmentation only occurs during fast heating [71], suggesting that the bubbles will continue to grow provided the temperature ramp is slow enough to allow the gas in them to pressurize above the dislocation punching pressure for the bubble. Heating tests however still show fragmentation and pulverisation occurring where ramp rates are low enough to allow bubble growth without bursting [23][48].

Another phenomenon that has not been considered is pore interlinkage, and the interactions that occur due to closely located pores. Pore interlinkage is observed when multiple gas bubbles coalesce, typically along grain boundaries, allowing pressures to relax, and potentially some gas to escape the grains depending on the extent and location of interlinkage. Some of this interlinkage is visible in images in ref [30]. Yang-Hyun et al suggests that above local porosity of 24% within a grain, significant interlinkage will occur,

and subsequent increases in FGR [31]. Literature agrees that porosity impacts fracture resistance of the fuel, with some applying the fracture criterion in equation 3.3 while also considering local pore density in a grain rather than overall porosity [35]. Phase field modelling has been applied in ref [67] to the process of nearby pore coarsening, however this cannot be directly applied to the pellet-scale predictions of pulverisation in this work. It may be possible to compute a rate at which bubble coarsening occurs at porosities and burnups above a specific threshold, which provides an additional method for pressure to relax. This could be applied for the amount of bubble bursting expected across a pellet diameter, slightly reducing it. No work has been conducted to determine if this is the case however.

With this in mind, the present model can only be considered applicable for fast temperature ramps of 10s of K/s, and the significant uncertainty for internal gas pressures should also be factored. Literature suggests that bubbles are expected to exist at pressures between the equilibrium pressure and the dislocation punching pressure [32] and show pressures above those estimated through simulation [1]. The model assumes all the bubbles are at their maximum overpressure during the temperature ramp, though it is expected that a proportion of bubbles do not exist at these pressures and so despite being in the same size class will not burst at the same temperature as other bubbles. Any pressure relaxation mechanisms have been neglected, though the addition of these would enhance the accuracy of the model, especially where a temperature ramp rate is considered.

Chapter 4

Conclusion

The two models presented in this work show different ways of predicting high burnup fragmentation in nuclear fuels. The empirical model presented in section 3.1 provides an estimate for the fuel pulverisation fraction where only burnup and temperature data is available. The equation for the average fragment size, fitted to the high burnup data, looks accurate within the range where most LOCA and heating tests have taken place and reflects the results from some experiments. The maximum < 1mm pulverisation fraction equation proposed by the NRC also fits nicely with publicly available experimental results, however the average pulverisation fraction, which should prove more useful as a less conservative estimate only shows a 0.5 r^2 value, indicating it needs further refinement with extra data. There is more that could be done to enhance the predictions in this model, the addition of more LOCA fragment size data would greatly enhance the accuracy. The Studsvik SCIP III and IV data, yet to be fully released, shows a similar relationship to what is predicted, though the validity of this is currently limited due to distribution data for < 1mm and < 2mm being the only publicly released results. Additionally there is a substantial gap in fragmentation data for burnups between 40 and 60 GWd, which poses an issue causing 2 possible fits to the average fragment size graph (see figure 3.2) depending on what data is eliminated as outliers. Again the more recent Studsvik experiments may help with this.

The mechanistic model presented by K.Kulacsy has been reproduced and verified, with minor enhancements. The source paper neglected many units and used some confusing statements for parts of equations. The units have

been properly derived and checked against supporting literature as well as the equations validated. Ronchi's EOS has been replaced with a molecular dynamics simulation to better reflect the states of gas in bubbles, however it does only consider xenon. The MD approach provides values for pressures similar to the ideal gas law at low temperatures but diverges as temperatures increase, however it is not the same as values from Ronchi's EOS. Indeed it may be more accurate for pressures in very small bubbles where the xenon may behave more like a solid than a fluid. With the validation and changes, the rearranging of the tangential stress equation allows the pressures for bubble burst, and fragmentation onset to be calculated without necessarily having access to irradiation data. Future work should consider identifying a relationship between burnup and bubble sizes and their distribution across a pellet radius in order to enable burnup to be used as an input parameter rather than requiring a bubble distribution as used in the example. Some papers have already identified size distributions at limited radial positions (as used in this work), but not assessments across an entire rod. Some recent work has taken place attempting to understand radial distributions of bubbles, however in metallic fuel, not ceramic [8]. A lot more experimental data would be required for this. With this inclusion, the model may be more easy to use within fuel performance code to calculate pulverisation risks during temperature ramps. Code currently uses more coarse models such as the true/false pulverisation model from Dr. Tony Turnbull. Additionally the surface energy value used for determining pressure should be changed to a value more accurately reflecting the mechanical conditions of the material. Additional work could also take place to compare pulverisation with other existing models. As higher FGR is an indicator of fine pulverisation and prior bubble bursting, code that can predict this at high burnups would provide a valuable comparison to what is predicted here. This was not planned or carried out due to the limited scope of this project.

For both cases, the predicted pulverisation needs to be compared to more experimental data, this however requires more PIE experiments to take place. If indeed there is a desire to keep fuel in reactors for longer, the understanding of conditions for fragmentation needs to be improved. Additionally, these

models likely only hold true for pure UO_2 fuel, with new fuels being developed with additives to enhance their thermal and mechanical characteristics, they need refining to account for these changes.

References

[1] L. K. Aagesen Jr, S. Biswas, K. A. Gamble, W. Jiang, P.-C. A. Simon and B. W. Spencer, 'Implementation and testing of physics-based pulverization model in bison,' Sep. 2022. DOI: 10.2172/1984930. [Online]. Available: https://www.osti.gov/biblio/1984930 (p. 56).

[2] B. J. Ade, 'Radial variation of burnup and source terms in high burnup lwr fuel...,' Oak Ridge National Lab.(ORNL), Oak Ridge, TN (United States), Tech. Rep., 2015 (p. 44).

[3] M. Bales, A. Chung, J. Corson and L. Kyriazidis, 'Interpretation of research on fuel fragmentation, relocation, and dispersal at high burnup,' *Washington (DC): The US Nuclear Regulatory Commission*, pp. 2021–13, 2021 (pp. viii, 22, 30, 36).

[4] T. Barani, G. Pastore, A. Magni, D. Pizzocri, P. Van Uffelen and L. Luzzi, 'Modeling intra-granular fission gas bubble evolution and coarsening in uranium dioxide during in-pile transients,' *Journal of Nuclear Materials*, vol. 538, p. 152 195, 2020 (p. 39).

[5] P. Blair, 'Modelling of fission gas behaviour in high burnup nuclear fuel,' Jan. 2008. DOI: 10.5075/epfl-thesis-4084 (p. 5).

[6] D. Brucklacher and W. Dienst, 'Creep behavior of ceramic nuclear fuels under neutron irradiation,' *Journal of Nuclear Materials*, vol. 42, no. 3, pp. 285–296, 1972, ISSN: 0022-3115. DOI: https://doi.org/10.1016/0022-3115(72)90079-7. [Online]. Available: https://www.sciencedirect.com/science/article/pii/0022311572900797 (p. 12).

[7] L. V. Brutzel, R. Dingreville and T. Bartel, 'Nuclear fuel deformation phenomena,' 2015. [Online]. Available: https://inis.iaea.org/search/search.aspx?orig_q=RN:47032408 (pp. vii, 12).

[8] L. Cai *et al.*, 'Understanding fission gas bubble distribution, lanthanide transportation, and thermal conductivity degradation in neutron-

irradiated α-u using machine learning,' *Materials Characterization*, vol. 184, p. 111 657, 2022, ISSN: 1044-5803. DOI: https://doi.org/10.1016/j.matchar.2021.111657. [Online]. Available: https://www.sciencedirect.com/science/article/pii/S1044580321007798 (p. 58).

[9] F. Cappia *et al.*, 'Critical assessment of the pore size distribution in the rim region of high burnup uo2 fuels,' *Journal of Nuclear Materials*, vol. 480, pp. 138–149, 2016, ISSN: 0022-3115. DOI: https://doi.org/10.1016/j.jnucmat.2016.08.010. [Online]. Available: https://www.sciencedirect.com/science/article/pii/S0022311516305712 (pp. ix, 48, 49).

[10] N. Capps *et al.*, 'Integral loca fragmentation test on high-burnup fuel,' *Nuclear Engineering and Design*, vol. 367, p. 110 811, 2020, ISSN: 0029-5493. DOI: https://doi.org/10.1016/j.nucengdes.2020.110811. [Online]. Available: https://www.sciencedirect.com/science/article/pii/S0029549320303058 (pp. viii, x, 15, 20, 21).

[11] W. Chen, M. W. Cooper, Z. Xiao, D. A. Andersson and X.-M. Bai, 'Effect of xe bubble size and pressure on the thermal conductivity of uo2—a molecular dynamics study,' *Journal of Materials Research*, vol. 34, no. 13, pp. 2295–2305, 2019. DOI: 10.1557/jmr.2019.93 (p. 10).

[12] M. Ding, X. Zhou, H. Zhang, H. Bian and Q. Yan, 'A review of the development of nuclear fuel performance analysis and codes for pwrs,' *Annals of Nuclear Energy*, vol. 163, p. 108 542, 2021, ISSN: 0306-4549. DOI: https://doi.org/10.1016/j.anucene.2021.108542. [Online]. Available: https://www.sciencedirect.com/science/article/pii/S0306454921004187 (p. 10).

[13] M. Flanagan and P. Askeljung, 'Observations of fuel fragmentation, mobility and release in integral, high-burnup, fueled loca tests,' in *Enlarged Halden Program Group Meeting, Sandefjord, Norway*, 2011, pp. 2–7 (pp. viii, 19).

[14] M. E. Flanagan, P. Askeljung and A. Puranen, *Post-test examination results from integral, high-burnup, fueled LOCA tests at Studsvik nuclear laboratory*. United States Nuclear Regulatory Commission, Office of Nuclear Regulatory . . ., 2013 (pp. 15, 30).

[15] T. Fuketa *et al.*, ‘Safety significance of the halden ifa-650 loca test results,’ Organisation for Economic Co-Operation and Development, Tech. Rep., 2010 (p. 15).

[16] G. Greenwood, A. Foreman and D. Rimmer, ‘The role of vacancies and dislocations in the nucleation and growth of gas bubbles in irradiated fissile material,’ *Journal of Nuclear Materials*, vol. 1, no. 4, pp. 305–324, 1959, ISSN: 0022-3115. DOI: https://doi.org/10.1016/0022-3115(59)90030-3. [Online]. Available: https://www.sciencedirect.com/science/article/pii/0022311559900303 (p. 55).

[17] D. T. Hagrman, C. M. Allison and G. A. Berna, ‘Scdap/relap5/mod 3.1 code manual: Matpro, a library of materials properties for light-water-reactor accident analysis. volume 4,’ Jun. 1995. DOI: 10.2172/100327. [Online]. Available: https://www.osti.gov/biblio/100327 (p. 38).

[18] R. Hall, M. Mortimer and D. Mortimer, ‘Surface energy measurements on uo2 — a critical review,’ *Journal of Nuclear Materials*, vol. 148, no. 3, pp. 237–256, 1987, ISSN: 0022-3115. DOI: https://doi.org/10.1016/0022-3115(87)90017-1. [Online]. Available: https://www.sciencedirect.com/science/article/pii/0022311587900171 (pp. 39, 54).

[19] R. Hilbert, V. Storhok, W. Chubb and D. Keller, ‘Mechanisms of swelling and gas release in uranium dioxide,’ *Journal of Nuclear Materials*, vol. 38, no. 1, pp. 26–34, 1971, ISSN: 0022-3115. DOI: https://doi.org/10.1016/0022-3115(71)90004-3. [Online]. Available: https://www.sciencedirect.com/science/article/pii/0022311571900043 (p. 11).

[20] A. Jelea, ‘On the laplace-young equation applied to spherical fluid inclusions in solid matrices,’ *Journal of Nuclear Materials*, vol. 505, pp. 127–133, 2018, ISSN: 0022-3115. DOI: https://doi.org/10.1016/j.jnucmat.2018.03.051. [Online]. Available: https://www.sciencedirect.com/science/article/pii/S0022311517317385 (p. 55).

[21] A. Jelea, ‘An equation of state for xenon/krypton mixtures confined in the nuclear fuels,’ *Journal of Nuclear Materials*, vol. 530, p. 151 952, 2020, ISSN: 0022-3115. DOI: https://doi.org/10.1016/j.jnucmat.

2019.151952. [Online]. Available: https://www.sciencedirect.com/science/article/pii/S0022311519312772 (pp. ix, 46).

[22] A. Jelea, R.-M. Pellenq and F. Ribeiro, 'An atomistic modeling of the xenon bubble behavior in the uo2 matrix,' *Journal of Nuclear Materials*, vol. 444, no. 1, pp. 153–160, 2014, ISSN: 0022-3115. DOI: https://doi.org/10.1016/j.jnucmat.2013.09.041. [Online]. Available: https://www.sciencedirect.com/science/article/pii/S0022311513011185 (p. 45).

[23] L. Jernkvist, 'Computational assessment of loca simulation tests on high burnup fuel rods in halden and studsvik,' Mar. 2017 (pp. 27, 55).

[24] L. O. Jernkvist, 'A review of analytical criteria for fission gas induced fragmentation of oxide fuel in accident conditions,' *Progress in Nuclear Energy*, vol. 119, p. 103 188, 2020, ISSN: 0149-1970. DOI: https://doi.org/10.1016/j.pnucene.2019.103188. [Online]. Available: https://www.sciencedirect.com/science/article/pii/S0149197019302963 (pp. 2, 15, 16, 55).

[25] L. O. Jernkvist and A. Massih, 'Analysis of the effect of uo {sub 2} high burnup microstructure on fission gas release,' 2002 (p. 44).

[26] L.-O. Jernkvist, A. Massih and A. Alvestav, 'Axial relocation of fragmented and pulverized fuel and its effect on fuel rod heat load during locas,' in *Top Fuel, Zurich, Switzerland (2015)*, European Nuclear Society, 2015, pp. 457–480 (p. 30).

[27] Jernkvist, Lars O., 'Modelling of fine fragmentation and fission gas release of uo2 fuel in accident conditions,' *EPJ Nuclear Sci. Technol.*, vol. 5, p. 11, 2019. DOI: 10.1051/epjn/2019030. [Online]. Available: https://doi.org/10.1051/epjn/2019030 (pp. 30, 37, 55).

[28] W. Jiang, T. Hu, L. K. Aagesen, S. Biswas and K. A. Gamble, 'A phase-field model of quasi-brittle fracture for pressurized cracks: Application to uo2 high-burnup microstructure fragmentation,' *Theoretical and Applied Fracture Mechanics*, vol. 119, p. 103 348, 2022, ISSN: 0167-8442. DOI: https://doi.org/10.1016/j.tafmec.2022.103348. [Online]. Available: https://www.sciencedirect.com/science/article/pii/S0167844222000994 (p. 37).

[29] E. Karb, M. Pruessmann, L. Sepold, P. Hofmann and G. Schanz, *Lwr fuel rod behavior in the fr2 in-pile tests simulating the heatup phase of a loca*, 1983. [Online]. Available: https://inis.iaea.org/search/search.aspx?orig_q=RN:14775917 (pp. vii, viii, 14, 15, 20).

[30] S. Kashibe, K. Une and K. Nogita, 'Formation and growth of intragranular fission gas bubbles in uo2 fuels with burnup of 6–83 gwd/t,' *Journal of Nuclear Materials*, vol. 206, no. 1, pp. 22–34, 1993, ISSN: 0022-3115. DOI: https://doi.org/10.1016/0022-3115(93)90229-R. [Online]. Available: https://www.sciencedirect.com/science/article/pii/002231159390229R (pp. 44, 55).

[31] Y.-H. Koo, J.-Y. Oh, B.-H. Lee and D.-S. Sohn, 'Three-dimensional simulation of threshold porosity for fission gas release in the rim region of lwr uo2 fuel,' *Journal of Nuclear Materials*, vol. 321, no. 2, pp. 249–255, 2003, ISSN: 0022-3115. DOI: https://doi.org/10.1016/S0022-3115(03)00249-6. [Online]. Available: https://www.sciencedirect.com/science/article/pii/S0022311503002496 (p. 56).

[32] K. Kulacsy, 'Mechanistic model for the fragmentation of the high-burnup structure during loca,' *Journal of Nuclear Materials*, vol. 466, pp. 409–416, 2015, ISSN: 0022-3115. DOI: https://doi.org/10.1016/j.jnucmat.2015.08.015. [Online]. Available: https://www.sciencedirect.com/science/article/pii/S0022311515301549 (pp. 2, 10, 13, 24, 37, 45, 56).

[33] G. Latimer, W. R. Marcum and W. F. Jones, 'Experimental study on fuel depressurization and its effect on dispersion,' *Nuclear Engineering and Design*, vol. 409, p. 112 355, 2023, ISSN: 0029-5493. DOI: https://doi.org/10.1016/j.nucengdes.2023.112355. [Online]. Available: https://www.sciencedirect.com/science/article/pii/S0029549323002042 (p. 2).

[34] L. Lei, M. Guoqiang and Z. Xiang, 'The analysis and improvement of fuel damage fraction calculate,' in *Proceedings of the 23rd Pacific Basin Nuclear Conference, Volume 2*, C. Liu, Ed., Singapore: Springer Nature Singapore, 2023, pp. 58–66, ISBN: 978-981-19-8780-9 (pp. vii, 6).

[35] F. Lemoine, J. Papin, J.-M. Frizonnet, B. Cazalis and H. Rigat, 'The role of grain boundary fission gases in high burn-up fuel under reactivity initiated accident conditions,' *Fuel*, vol. 7, p. 98, 2002 (p. 56).

[36] A. Magni *et al.*, 'Chapter 8 - the transuranus fuel performance code,' in *Nuclear Power Plant Design and Analysis Codes*, ser. Woodhead Publishing Series in Energy, J. Wang, X. Li, C. Allison and J. Hohorst, Eds., Woodhead Publishing, 2021, pp. 161–205, ISBN: 978-0-12-818190-4. DOI: https://doi.org/10.1016/B978-0-12-818190-4.00008-5. [Online]. Available: https://www.sciencedirect.com/science/article/pii/B9780128181904000085 (pp. 1, 8).

[37] A. Massih, 'Irradiation induced swelling of nuclear fuel,' ASEA-ATOM AB, Tech. Rep., 1988 (p. 11).

[38] R. O. Meyer and W. Wiesenack, 'A critique of fuel behavior in loca safety analyses and a proposed alternative,' *Nuclear Engineering and Design*, vol. 394, p. 111 816, 2022, ISSN: 0029-5493. DOI: https://doi.org/10.1016/j.nucengdes.2022.111816. [Online]. Available: https://www.sciencedirect.com/science/article/pii/S0029549322001704 (p. 32).

[39] S. C. Middleburgh, W. E. Lee and M. J. Rushton, *Ceramics in the nuclear fuel cycle*, Jan. 2019. DOI: 10.1016/B978-0-08-102726-4.00002-8 (p. 5).

[40] NEA, 'Fission gas behavior in water reactor fuels,' Paris, 2002 (p. 14).

[41] M. OGUMA, 'Microstructure effects on fracture strength of u02 fuel pellets,' *Journal of Nuclear Science and Technology*, vol. 19, no. 12, pp. 1005–1014, 1982. DOI: 10.1080/18811248.1982.9734249. eprint: https://doi.org/10.1080/18811248.1982.9734249. [Online]. Available: https://doi.org/10.1080/18811248.1982.9734249 (pp. viii, 38).

[42] M. Oguma, 'Integrity degradation of uo2 pellets subjected to thermal shock,' *Journal of Nuclear Materials*, vol. 127, no. 1, pp. 67–76, 1985, ISSN: 0022-3115. DOI: https://doi.org/10.1016/0022-3115(85)90062-5. [Online]. Available: https://www.sciencedirect.com/science/article/pii/0022311585900625 (p. 16).

[43] D. R. Olander, 'Fundamental aspects of nuclear reactor fuel elements: Solutions to problems,' California Univ., Berkeley (USA). Dept. of Nuclear Engineering, Tech. Rep., 1976 (pp. 10, 40).

[44] D. R. Olander, 'Interaction of stresses with inclusions in solids — a review,' *Journal of Nuclear Materials*, vol. 92, no. 2, pp. 163–183, 1980, ISSN: 0022-3115. DOI: https://doi.org/10.1016/0022-3115(80)90100-2. [Online]. Available: https://www.sciencedirect.com/science/article/pii/0022311580901002 (pp. 39, 41).

[45] B. M. T. C. Peluzo and E. Kraka, 'Uranium: The nuclear fuel cycle and beyond,' *International Journal of Molecular Sciences*, vol. 23, p. 4655, 9 Apr. 2022, ISSN: 1422-0067. DOI: 10.3390/ijms23094655 (p. 5).

[46] C. Pillai and A. George, 'Thermal conductivity of uranium dioxide,' *Journal of Nuclear Materials*, vol. 200, no. 1, pp. 78–81, 1993, ISSN: 0022-3115. DOI: https://doi.org/10.1016/0022-3115(93)90011-M. [Online]. Available: https://www.sciencedirect.com/science/article/pii/002231159390011M (p. 12).

[47] L. Pizzagalli and M.-L. David, 'Surface stress calculations for nanoparticles and cavities in aluminum, silicon, and iron: Influence of pressure and validity of the young-laplace equation,' *Materials Theory*, vol. 5, no. 1, p. 5, 2021 (p. 55).

[48] P. Raynaud, 'Fuel fragmentation, relocation and dispersal during the loss-of-coolant accident, 2012,' *Report NUREG-2121, US Nuclear Regulatory Commission, Washington, DC, USA*, (p. 55).

[49] J. Rest, M. Cooper, J. Spino, J. Turnbull, P. Van Uffelen and C. Walker, 'Fission gas release from uo2 nuclear fuel: A review,' *Journal of Nuclear Materials*, vol. 513, pp. 310–345, 2019, ISSN: 0022-3115. DOI: https://doi.org/10.1016/j.jnucmat.2018.08.019. [Online]. Available: https://www.sciencedirect.com/science/article/pii/S0022311518309449 (p. 13).

[50] C. Ronchi, 'Physical processes and mechanisms related to fission gas swelling in mx-type nuclear fuels,' *Journal of Nuclear Materials*, vol. 84, no. 1, pp. 55–84, 1979, ISSN: 0022-3115. DOI: https://doi.org/10.1016/0022-3115(79)90150-8. [Online]. Available: https://www.sciencedirect.com/science/article/pii/0022311579901508 (p. 45).

[51] C. Ronchi, ‘Extrapolated equation of state for rare gases at high temperatures and densities,’ *Journal of Nuclear Materials*, vol. 96, no. 3, pp. 314–328, 1981, ISSN: 0022-3115. DOI: https://doi.org/10.1016/0022-3115(81)90575-4. [Online]. Available: https://www.sciencedirect.com/science/article/pii/0022311581905754 (pp. 37, 44).

[52] V. V. Rondinella and T. Wiss, ‘The high burn-up structure in nuclear fuel,’ *Materials Today*, vol. 13, pp. 24–32, 12 Dec. 2010, ISSN: 1369-7021. DOI: 10.1016/S1369-7021(10)70221-2 (p. 6).

[53] B. Roostaii, *Kerntechnik*, vol. 88, no. 3, pp. 354–360, 2023. DOI: doi:10.1515/kern-2022-0121. [Online]. Available: https://doi.org/10.1515/kern-2022-0121 (p. 44).

[54] G. Rossiter, ‘Development of the enigma fuel performance code for whole core analysis and dry storage assessments,’ *Nuclear Engineering and Technology*, vol. 43, Dec. 2011. DOI: 10.5516/NET.2011.43.6.489 (pp. 1, 8).

[55] P. Roy and D. Sah, ‘Irradiation behaviour of nuclear fuels,’ *Pramana*, vol. 24, pp. 397–421, 1985 (p. 12).

[56] R. L. Seibert, J. W. Werden, C. M. Parish, J. M. Harp, T. J. Gerczak and N. A. Capps, ‘Initial microstructure examination of high burnup fuel with varying operational burnups,’ Jun. 2022. DOI: 10.2172/1878682. [Online]. Available: https://www.osti.gov/biblio/1878682 (p. 44).

[57] H. Sonnenburg *et al.*, ‘Report on fuel fragmentation, relocation, dispersal,’ Oct. 2016 (pp. vii, x, 18, 19, 21).

[58] N. Soppera, M. Bossant and E. Dupont, ‘Janis 4: An improved version of the nea java-based nuclear data information system,’ *Nuclear Data Sheets*, vol. 120, pp. 294–296, 2014, ISSN: 0090-3752. DOI: https://doi.org/10.1016/j.nds.2014.07.071. [Online]. Available: https://www.sciencedirect.com/science/article/pii/S0090375214005237 (pp. vii, 7).

[59] J. Spino, J. Rest, W. Goll and C. Walker, ‘Matrix swelling rate and cavity volume balance of uo2 fuels at high burn-up,’ *Journal of Nuclear Materials*, vol. 346, no. 2, pp. 131–144, 2005, ISSN: 0022-3115. DOI: https://doi.org/10.1016/j.jnucmat.2005.06.015. [Online].

Available: https://www.sciencedirect.com/science/article/pii/S0022311505002898 (p. 45).

[60] 'Sustainable power technologies and infrastructure,' English, *Tribology & Lubrication Technology*, vol. 72, no. 3, p. 92, Mar. 2016, Copyright - Copyright Society of Tribologists and Lubrication Engineers Mar 2016; Last updated - 2023-06-23; CODEN - LUENAG. [Online]. Available: https://bangor.idm.oclc.org/login?qurl=https%3A%2F%2Fwww.proquest.com%2Fscholarly-journals%2Fsustainable-power-technologies-infrastructure%2Fdocview%2F1772038339%2Fse-2%3Faccountid%3D14874 (pp. vii, 4).

[61] M. Tonks *et al.*, 'Unit mechanisms of fission gas release: Current understanding and future needs,' *Journal of Nuclear Materials*, vol. 504, pp. 300–317, 2018, ISSN: 0022-3115. DOI: https://doi.org/10.1016/j.jnucmat.2018.03.016. [Online]. Available: https://www.sciencedirect.com/science/article/pii/S0022311517313405 (pp. vii, 10, 11).

[62] M. R. Tonks *et al.*, 'Mechanistic materials modeling for nuclear fuel performance,' *Annals of Nuclear Energy*, vol. 105, pp. 11–24, 2017, ISSN: 0306-4549. DOI: https://doi.org/10.1016/j.anucene.2017.03.005. [Online]. Available: https://www.sciencedirect.com/science/article/pii/S0306454916307423 (pp. vii, 9, 10).

[63] C. Tucker, *How to Drive a Nuclear Reactor*. Jan. 2019, ISBN: 978-3-030-33875-6. DOI: 10.1007/978-3-030-33876-3 (pp. 3–5, 7).

[64] J. A. Turnbull, S. K. Yagnik, M. Hirai, D. M. Staicu and C. T. Walker, 'An assessment of the fuel pulverization threshold during loca-type temperature transients,' *Nuclear Science and Engineering*, vol. 179, no. 4, pp. 477–485, 2015. DOI: 10.13182/NSE14-20. eprint: https://doi.org/10.13182/NSE14-20. [Online]. Available: https://doi.org/10.13182/NSE14-20 (pp. vii, 13, 16, 17).

[65] K. UNE, S. KASHIBE and A. TAKAGI, 'Fission gas release behavior from high burnup uo2 fuels under rapid heating conditions,' *Journal of Nuclear Science and Technology*, vol. 43, no. 9, pp. 1161–1171, 2006. DOI: 10.1080/18811248.2006.9711208. eprint: https://doi.

org/10.1080/18811248.2006.9711208. [Online]. Available: https://doi.org/10.1080/18811248.2006.9711208 (pp. 14, 37, 55).

[66] P. Van Uffelen, J. Hales, W. Li, G. Rossiter and R. Williamson, 'A review of fuel performance modelling,' *Journal of Nuclear Materials*, vol. 516, pp. 373–412, 2019, ISSN: 0022-3115. DOI: https://doi.org/10.1016/j.jnucmat.2018.12.037. [Online]. Available: https://www.sciencedirect.com/science/article/pii/S0022311518310298 (p. 10).

[67] M. Veshchunov and V. Tarasov, 'Modelling of pore coarsening in the high burn-up structure of uo2 fuel,' *Journal of Nuclear Materials*, vol. 488, pp. 191–195, 2017, ISSN: 0022-3115. DOI: https://doi.org/10.1016/j.jnucmat.2017.03.013. [Online]. Available: https://www.sciencedirect.com/science/article/pii/S0022311517301356 (p. 56).

[68] R. L. Williamson *et al.*, 'Bison: A flexible code for advanced simulation of the performance of multiple nuclear fuel forms,' *Nuclear Technology*, vol. 207, no. 7, pp. 954–980, 2021. DOI: 10.1080/00295450.2020.1836940. eprint: https://doi.org/10.1080/00295450.2020.1836940. [Online]. Available: https://doi.org/10.1080/00295450.2020.1836940 (p. 8).

[69] T. Wiss *et al.*, 'Properties of the high burnup structure in nuclear light water reactor fuel,' *Radiochimica Acta*, vol. 105, pp. 893–906, 11 Nov. 2017, ISSN: 2193-3405. DOI: 10.1515/ract-2017-2831 (pp. vii, 14, 15).

[70] Z. Xiao, Y. Wang, S. Hu, Y. Li and S.-Q. Shi, 'A quantitative phase-field model of gas bubble evolution in uo2,' *Computational Materials Science*, vol. 184, p. 109 867, 2020, ISSN: 0927-0256. DOI: https://doi.org/10.1016/j.commatsci.2020.109867. [Online]. Available: https://www.sciencedirect.com/science/article/pii/S092702562030358X (p. 45).

[71] A. Yamauchi, 'Study on the relationship between fuel fragmentation during a loca and pellet microstructure,' *Journal of Nuclear Science and Technology*, vol. 58, no. 12, pp. 1330–1342, 2021. DOI: 10.1080/00223131.2021.1943556. eprint: https://doi.org/10.1080/00223131.

2021 . 1943556. [Online]. Available: https://doi.org/10.1080/00223131.2021.1943556 (pp. 16, 55).

Appendix A

Empirical Model Code

```
import math
import re
import os
import sys


upper_pulverization_1mm = []
core = [[]]
dsize = 9.5


# segment burnup, segment average temperature

def GetSegmentPulverization(segment_burnup, local_temperature ):
    turnbull_pulverization: bool = 0
    local_pulverization_percent = 0
    local_average_fragment_size: float = 0
    # determine local fragment average size with curve
    local_average_fragment_size = 4490*math.exp(-0.112*
   segment_burnup)+0.308
    # determine turnbull fragmention
    temperature_bound_lower: float = 917 # minimum pulverisation
   temperature threshold for burnups of 70 - 79 GWd
    temperature_bound_upper: float = 635 # minimum pulverisation
   temperature thresholdfor burnups of > 95 GWd
    temperature_variable_bound: float = -11.24*segment_burnup +
   1703.8 # minimum pulverisation temperature dynamic threshold
   for 79 GWd < local_burnup <= 95 GWd

    turnbull_pulverization = (local_temperature >
   temperature_bound_lower and segment_burnup > 70) or (
   local_temperature > temperature_variable_bound and
   segment_burnup > 79) or (local_temperature >
   temperature_bound_upper and segment_burnup > 95)
    #pulverized percentage https://www.nrc.gov/docs/ML2131/
   ML21313A145.pdf
    local_pulverization_percent = (local_temperature >
   temperature_bound_upper)*((segment_burnup >= 55 and
   segment_burnup < 80) * (0.04*(segment_burnup-55))) + (
   segment_burnup >= 80)
    #local_pulverization_percent = (local_temperature >
   temperature_bound_upper)*(segment_burnup >= 55 and
   segment_burnup < 80) * ((0.025*segment_burnup)-1.38)
    return turnbull_pulverization, local_average_fragment_size,
   local_pulverization_percent


# get the average pulverisation fraction for a rod given the
   pulverisation fracion for segments,
# segment data read from enigma output file, [burnup, temperature
    (c)]
def GetRodPulverizationPercent(segments):
    rodAveragePulverizationFraction = 0
    rodAverageBurnup = 0
    rodAverageTemperature = 0
```

```
    for i in len(segments):
        rodAveragePulverizationFraction +=
   GetSegmentPulverization(segments[i][0], segments[i][1])
        rodAverageBurnup += segments[i][0]
        rodAverageTemperature += segments[i][1]
    rodAveragePulverizationFraction =
   rodAveragePulverizationFraction/len(segments)
    rodAverageBurnup = rodAverageBurnup/len(segments)
    rodAverageTemperature = rodAverageTemperature/len(segments)
    return rodAveragePulverizationFraction, rodAverageBurnup,
   rodAverageTemperature

def GetCoreFragmentationPercent():
    rods = len(upper_pulverization_1mm)
    total = 0
    for i in upper_pulverization_1mm:
        total = total + i[2]
        print(total)
    total = total/rods
    return total


def processBurnup(infile, average, outfile, aoutfile, fragsize):
    f = open(infile, "r").read()
    #print(dsize)
    try:
        os.remove(outfile)
    except:
        pass
    fr = open(outfile, 'x')
    if aoutfile != "":
        try:
            os.remove(aoutfile)
        except:
            pass
        of = open(aoutfile, 'x')
        of.write("EOST-/h    AVG-BU-MWd/tU  AVG-PULV-1mm\n")
    #print(f)
    #([^\d?.]\d+  +\d\d?.\d\d)
    m = re.findall('(?<=\d-)[\s\d\W]*(?=MEAN)', f)
    m = re.findall('\d*-[\s\d\W]*(?=MEAN)', f)
    #print(m[196].strip(" ").split("\n")[1].strip(" ").split()
   [-18])
    i = 0
    for block in m:
        avgb = 0
        avgf = 0
        avgfs = 0
        i+=1
        block = block.strip(" ")
        fr.write("\nSTEP " + block.split()[0])
        #print(block)
        fr.write("\nSUB-STEP " + block.split()[1] + "\n")
        fr.write("END OF STEP HOURS: " + block.split()[2] + "\n")
        fr.write("BURNUP MWd/tU   TEMPERATURE   PULV-FRAC-SUB-1mm
   \n")
        axialzones = block.split("\n")
        for zone in axialzones:
            zone = zone.strip(" ")
            #print(zone)
            parameters = zone.split()
            #print(parameters)
            # from end as first zone has 2 extra parameters
            try:
                burnup = parameters[-18]
                avgb += int(burnup)

                temperature = parameters[-13]
```

```
                avgf += float(GetSegmentPulverization(float(
burnup)/1000, float(temperature))[2]*100)
                fr.write(burnup.ljust(15) + " " + temperature.
ljust(13) + " " + str(round(GetSegmentPulverization(int(burnup
)/1000, int(temperature))[2]*100, 2)).ljust(20) )
                if (fragsize == True):
                    fr.write(str(min(dsize, round(
GetSegmentPulverization(float(burnup)/1000, float(temperature)
)[1], 2))))
                    avgfs += min(dsize, GetSegmentPulverization(
float(burnup)/1000, float(temperature))[1])
                fr.write("\n")
            except Exception as e:
                #print(e)
                continue
        if (average == True):
            fr.write(str(round(avgb/(len(axialzones)-1), 2)).
ljust(30) + str(round(avgf/(len(axialzones)-1), 2))+"%\n")
            if (aoutfile != ""):

                of.write(str(block.split()[2]).ljust(10) + str(
round(avgb/(len(axialzones)-1), 2)).ljust(15) + str(round(avgf
/(len(axialzones)-1), 2)).ljust(15))
                if (fragsize== True):
                    of.write(str(round(avgfs/(len(axialzones)-1),
 2)))
                of.write("\n")


def err():
    print("Correct usage:\n -i <infile>\nOptional:\n -a : Output
rod averages\n -A <average output file>\n -o <output file>\n -
f : Calculate average fragment size\n -d <rod diameter (mm)>")
#command line args
def main(argv):
    global dsize
    average = False
    fragsize = False
    arg=1
    outfile = "out.txt"
    aoutfile = ""
    try:
        while arg < len(argv):
            #print(arg)
            #print(argv[arg])
            if argv[arg] == "-i":
                infile = argv[arg+1]
                print(infile)
                arg += 1
            elif argv[arg] == "-a":
                average = True
                print("average")
            elif argv[arg] == "-A":
                aoutfile = argv[arg+1]
                print(aoutfile)
                arg += 1
            elif argv[arg] == "-o":
                outfile = argv[arg+1]
                print(outfile)
                arg += 1
            elif argv[arg] == "-f":
                fragsize = True
            elif argv[arg] == "-d":
                dsize = float(argv[arg+1])
                print(dsize)
                arg+= 1
            else:
                err()
            arg+=1
```

```
        if infile:
            processBurnup(infile, average, outfile, aoutfile,
    fragsize)

    except Exception as e:
        err()
        #print(e)

        #err()


if __name__ == "__main__": main(sys.argv)
```

Appendix B

Mechanistic Model Code

B.1 fragmentation-no-ramp.h

```
#include <math.h>
#include <stdlib.h>
#include <iostream>
#include <vector>

using namespace std;

class PressureDrivenFragmentationLib {
    public:
        /**
            Calculates the equilibrium pressure for a pore of a
   given size.

            @return [MPa] Equilibrium pressure

            @param pressure_hydrostatic [MPa] The external
   hydrostatic pressure.
            @param surface_energy [J/m  ] The surface energy of
   the ceramic around the pore.
            @param pore_size [ m ] The radius of the pore.


        */
        float pressure_equilibrium(float pressure_hydrostatic,
   float surface_energy, float pore_radius);

        /**
            Calculates the limit of overpressure that can
   permanently be sustained in a pore necessary.
            to allow for bubble growth.

            @return [MPa] Expansion pressure

            @param shear_modulus [GPa] The shear modulus of the
   material.
            @param burgers_vector [nm] The burgers vector for the
    ceramic.
            @param pore_radius [ m ] The radius of the pore.

        */
        float pressure_expansion(float shear_modulus, float
   burgers_vector, float pore_radius);

        /**

            Calculates the maximum pressure that a pore can
   sustain during normal fuel operation.

            @return [MPa] Pressure limit
```

```
         @param _pressure_expansion [MPa] The expansion
pressure for the pore size.
         @param _pressure_equilibrium [MPa] The equilibrium
pressure for the pore size.

     */
     float pressure_limit(float _pressure_expansion, float
_pressure_equilibrium);

     /**
         Calculates the tangential stress experienced at the
surface of a spherical pore, assuming that the pore is at the
maximum overpressure.

         As defined by:
               = Gb/r - 1/2* P

         @return [MPa] Tangential stress at pore surface

         @param _pressure_expansion [MPa] The expansion
pressure for the pore size.
         @param pressure_hydrostatic [MPa] The external
hydrostatic pressure.

     */
     float pore_tangential_stress(float _pressure_expansion,
float pressure_hydrostatic);

     /**
         Calculates the tangential stress experienced at the
surface of a spherical pore, caused by a given pressure in the
 pore.

         @return [MPa] Tangential stress at pore surface

         @param _pressure [MPa] The pressure in the pore
during heating.
         @param _pressure_hydrostatic [MPa] The external
hydrostatic pressure.
         @param _surface_energy [J/m  ] The surface energy of
the ceramic around the pore.
         @param _pore_radius [ m ] The radius of the pore.

     */
     float pore_tangential_stress_heating(float _pressure,
float _pressure_hydrostatic, float _surface_energy, float
_pore_radius);

     /**
         Calculates the fracture strength of the UO2 lattace
given a temperature and porosity fraction.

         @return [MPa] Fracture strength

         @param temperature [K] The temperature of the ceramic
.
         @param porosity_dependance [%] The porosity fraction
for the ceramic.

     */
     float UO2_fracture_strength(float temperature, float
porosity_dependance);

     /**
         Calculates the temperature dependant surface energy
of a free UO2 face.

         @return [J/m  ] Surface energy

         @param temperature [K] The temperature of the ceramic
.
```

```
     */
     float pressure_surface_energy(float temperature);

     /**
         Calculates the temperature and porosity dependant
surface energy of a free UO2 face.

         @return [J/m  ] Surface energy

         @param temperature [K] The temperature of the ceramic
.
         @param porosity_dependance [%] The porosity fraction
for the ceramic.

     */
     float porosity_dependant_surface_energy(float temperature
, float porosity_dependance);

     /**
         Calculates the young modulus for a material given
temperature and porosity.

         @return [MPa] Young modulus

         @param temperature [K] The temperature of the ceramic
.
         @param porosity_dependance [%] The porosity fraction
for the ceramic.

     */
     float young_modulus(float temperature, float
porosity_dependance);

     /**
         Calculates the porosity dependant poissons ratio for
the material.

         @return  Poissons ratio

         @param porosity_dependance [%] The porosity fraction
for the ceramic.

     */
     float poissons_ratio(float porosity_dependance);

     /**
         Calculates the shear strength for a material.

         Derived from E=2G(1+v)

         @return [MPa] Shear strength

         @param young_modulys [MPa] The young modulus of the
material.
         @param poissons_ratio The poissons ratio for the
material.

     */
     float shear_strength(float young_modulus, float
poissons_ratio);

     /**
         Returns true if the pore tangential stress is greater
 than the fracture strength of the UO2.

         @return true if tangential_stress >
UO2_fracture_strength

         @param _hyrostatic_pressure [MPa] The external
hydrostatic pressure.
```

```
            @param _temperature [K] The temperature of the
    ceramic.
            @param _porosity_dependance [%] The porosity fraction
     for the ceramic.
            @param _burgers_vector [nm] The burgers vector for
    the ceramic.
            @param _pore_radius [ m ] The radius of the pore.

        */
        bool  burst_pore_size(float _hydrostatic_pressure, float
    _temperature, float _porosity_dependance, float
    _burgers_vector, float _pore_radius);

};
```

B.2 ronchiEOS.h

```
#include <vector>
#include <map>
#include <iostream>

using namespace std;


//https://reader.elsevier.com/reader/sd/pii/0022311581905754?
    token=53
    A74CB05D2157249221B1F7A694E3C4562627826FFEBAA43C2ECD9411D0841066236C83FA26C
    &originRegion=eu-west-1&originCreation=20230504115639
//V = cm3/mol
// T = C
class RochiEOS {
    public:
    float volume[20] = {
        377.4,
        188.7,
        125.8,
        94.3,
        75.5,
        62.9,
        53.9,
        47.2,
        41.9,
        37.7,
        34.3,
        31.4,
        29.0,
        27.0,
        25.2,
        23.6,
        22.2,
        21.0,
        19.9,
        18.9
    };

    float temperature[21] = {
        300,
        400,
        500,
        600,
        700,
        800,
        900,
        100,
        1100,
        1200,
        1300,
        1400,
        1500,
```

```
     1600,
     1700,
     1800,
     1900,
     2000,
     2100,
     2200,
     2300
 };


 float data[21][2][20] = {
     {
         {
             0.69, 0.46, 0.32, 0.34, 0.58, 1.16, 2.21, 3.91,
6.48, 10.2, 15.42, 22.59, 32.31, 45.41, 63.17, 87.65, 122.79,
177.18, 274.04, 498.66
         },
         {
             45, 60, 63, 88, 191, 459, 1021, 2065, 3853, 6739,
 11200, 17913, 27757, 42020, 62622, 92693, 137969, 210792,
344141, 659168
         }
     },
     {
         {
             0.83, 0.71, 0.65, 0.69, 0.89, 1.33, 2.08, 3.27,
5.04, 7.56, 11.05, 15.81, 22.23, 30.86, 42.54, 58.74, 82.02,
117.86, 179.68, 308.95
         },
         {
             73, 124, 170, 243, 394, 701, 1284, 2306, 3995,
4659, 10714, 16722, 25467, 38075, 56258, 82826, 122880,
186960, 300848, 544531
         }
     },
     {
         {
             0.91, 0.86, 0.87, 0.97, 1.20, 1.63, 2.33, 3.39,
4.93, 7.09, 10.05, 14.05, 19.40, 26.56, 36.23, 49.52, 60.47,
97.14, 144.91, 237.97
         },
         {
             100, 189, 286, 426, 662, 1078, 1797, 2989, 4888,
7809, 12177, 18567, 27780, 40965, 59858, 87277, 128220,
192614, 303287, 524286
         }
     },
     {
         {
             0.96, 0.96, 1.01, 1.15, 1.41, 1.84, 2.51, 3.50,
4.91, 6.87, 9.52, 13.09, 17.83, 24.15, 32.63, 44.23, 60.60,
84.97, 124.44, 197.42
         },
         {
             126, 253, 400, 606, 929, 1458, 2323, 3704, 5846,
9079, 13849, 20757, 30640, 44691, 64702, 93540, 136179,
202186, 312530, 521921
         }
     },
     {
         {
             0.99, 1.02, 1.11, 1.27, 1.54, 1.97, 2.62, 3.56,
4.88, 6.69, 9.12, 12.37, 16.68, 22.39, 30.02, 40.40, 54.92,
76.24, 109.98, 169.91

         },
         {
             153, 315, 511, 1187, 1826, 2833, 4396, 6774,
10312, 15474, 22891, 33433, 48337, 69448, 99676, 143982,
211651, 322258, 524053
```

```
            }
        },
        {
            {
                1.02, 1.07, 1.17, 1.35, 1.63, 2.06, 2.69, 3.59,
4.83, 6.52, 8.78, 11.78, 15.74, 20.98, 27.95, 37.37, 50.46,
69.46, 94.94, 149.64
            },
            {
                179, 377, 620, 951, 1439, 2182, 3324, 5061, 7762,
 11487, 17019, 24914, 36070, 51765, 73886, 105382, 151192,
220355, 331315, 527477
            }
        },
        {
            {
                1.03, 1.10, 1.22, 1.41, 1.70, 2.13, 2.74, 3.59,
4.77, 6.36, 8.48, 11.28, 14.96, 19.81, 26.23, 34.88, 46.82,
63.96, 90.14, 133.97
            },
            {
                205, 437, 727, 1119, 1684, 2528, 3799, 5701,
8514, 12610, 18490, 26829, 38555, 54970, 78022, 110661,
157812, 228286, 339580, 531283
            }
        },
        {
            {
                1.05, 1.13, 1.26, 1.46, 1.75, 2.17, 2.76, 3.59,
4.71, 6.21, 8.21, 10.84, 14.28, 18.81, 24.78, 32.79, 43.77,
59.40, 82.93, 121.46

            },
            {
                230, 498, 832, 1283, 1925, 2866, 4261, 6322,
9337, 13690, 19897, 28654, 40911, 58007, 81896, 115573,
163924, 235554, 347142, 535183
            }
        },
        {
            {
                1.06, 1.15, 1.29, 1.49, 1.78, 2.20, 2.78, 3.57,
4.65, 6.08, 7.97, 10.45, 13.70, 17.94, 23.53, 30.99, 41.17,
55.54, 76.91, 111.22
            },
            {
                256, 557, 937, 1445, 2161, 3196, 4712, 6926,
10134, 14733, 21251, 30401, 43156, 60880, 85550, 120178,
169613, 242273, 354121, 539085
            }
        },
        {
            {
                1.07, 1.17, 1.31, 1.52, 1.81, 2.22, 2.78, 3.55,
4.59, 5.96, 7.76, 10.11, 13.18, 17.19, 22.45, 29.44, 30.93,
52.23, 71.79, 102.69

            },
            {
                282, 617, 1040, 1605, 2393, 3521, 5153, 7515,
10910, 15744, 22560, 32084, 45309, 63621, 89019, 124523,
174950, 248537, 360621, 542958
            }
        },
        {
            {
                1.07, 1.18, 1.33, 1.54, 1.83, 2.24, 2.79, 3.53,
4.53, 5.84, 7.56, 9.81, 12.73, 16.52, 21.49, 28.07, 36.97,
49.35, 67.39, 95.46

            },
```

```
        {
            307, 676, 1143, 1764, 2623, 3841, 5587, 8092,
11668, 16729, 23829, 33710, 47382, 66249, 92330, 128649,
179989, 254422, 366725, 546796
        }
    },
    {
        {
            1.08, 1.19, 1.35, 1.56, 1.85, 2.25, 2.79, 3.51,
4.47, 5.74, 7.39, 9.53, 12.32, 15.93, 20.64, 26.87, 35.24,
46.03, 63.56, 89.26

        },
        {
            333, 735, 1245, 1921, 2850, 4157, 6014, 8659,
12410, 17690, 25064, 35288, 49386, 68780, 95504, 132587,
184775, 259988, 372500, 550597
        }
    },
    {
        {
            1.09, 1.20, 1.36, 1.57, 1.86, 2.25, 2.78, 3.49,
4.42, 5.64, 7.23, 9.29, 11.95, 15.39, 19.88, 25.79, 33.70,
44.60, 60.20, 83.88
        },
        {
            358, 794, 1346, 2077, 3075, 4469, 6435, 9216,
13137, 18630, 26269, 36822, 51329, 71226, 98560, 136362,
189343, 265282, 377996, 554365
        }
    },
    {
        {
            1.09, 1.21, 1.37, 1.58, 1.87, 2.26, 2.78, 3.46,
4.37, 5.55, 7.08, 9.06, 11.61, 14.91, 19.20, 24.82, 32.33,
42.61, 57.22, 79.16

        },
        {
            384, 852, 1447, 2232, 3298, 4777, 6850, 9765,
13852, 19552, 27448, 38319, 53218, 73596, 101511, 139995,
193723, 270340, 383255, 558101
        }
    },
    {
        {
            1.09, 1.22, 1.38, 1.59, 1.88, 2.26, 2.77, 3.44,
4.32, 5.46, 6.94, 8.85, 11.31, 14.48, 18.58, 23.95, 31.09,
40.82, 54.57, 75.00
        },
        {
            409, 910, 1547, 2385, 3519, 5082, 7260, 10306,
14556, 20457, 28602, 39781, 55059, 75899, 104370, 143501,
197936, 275194, 388308, 561806
        }
    },
    {
        {
            1.10, 1.22, 1.38, 1.60, 1.89, 2.26, 2.76, 3.42,
4.27, 5.38, 6.82, 8.66, 11.03, 14.07, 18.01, 23.15, 29.96,
39.21, 52.18, 71.30
        },
        {
            434, 968, 1647, 2538, 3738, 5384, 7666, 10840,
15249, 21347, 29735, 41213, 56856, 78141, 107145, 146895,
202001, 279868, 393182, 565484
        }
    },
    {
        {
```

```
            1.10, 1.23, 1.39, 1.61, 1.89, 2.26, 2.75, 3.39,
4.23, 5.31, 6.70, 8.48, 10.77, 13.71, 17.49, 22.42, 28.94,
37.74, 50.03, 67.98
        },
        {
            459, 1026, 1746, 2690, 3955, 5683, 8067, 11367,
15932, 22222, 30847, 42616, 58614, 80329, 109845, 150188,
205935, 284382, 397899, 569134
        }
    },
    {
        {
            1.10, 1.23, 1.40, 1.61, 1.89, 2.26, 2.74, 3.37,
4.19, 5.24, 6.59, 8.32, 10.53, 13.37, 17.02, 21.76, 28.00,
36.41, 48.07, 64.99
        },
        {
            485, 1084, 1845, 2841, 4171, 5980, 8465, 11889,
16607, 23085, 31941, 43993, 60336, 82467, 112477, 153390,
209752, 288753, 402476, 572758
        }
    },
    {
        {
           1.10, 1.23, 1.40, 1.62, 1.90, 2.26, 2.74, 3.35,
4.15, 5.17, 6.49, 8.17, 10.31, 13.05, 16.58, 21.14, 27.14,
35.18, 46.29, 62.29
        },
        {
            510, 1141, 1944, 2991, 4386, 6275, 8858, 12405,
17273, 23937, 33019, 45346, 62025, 84559, 115048, 156509,
213461, 292997, 406927, 576357
        }
    },
    {
        {
            1.10, 1.24, 1.40, 1.62, 1.90, 2.26, 2.73, 3.33,
4.11, 5.11, 6.39, 8.03, 10.11, 12.76, 16.17, 20.57, 26.34,
34.06, 44.66, 59.83
        },
        {
            535, 1199, 2042, 3140, 4599, 6568, 9249, 12916,
17932, 24777, 34080, 46678, 63683, 86609, 117561, 159552,
217073, 297124, 411266, 579931
        }
    },
    {
        {
            1.11, 1.24, 1.41, 1.62, 1.90, 2.26, 2.72, 3.31,
4.08, 5.05, 6.30, 7.89, 9.91, 12.49, 15.79, 20.05, 25.61,
33.02, 43.16, 57.57
        },
        {
            560, 1256, 2140, 3289, 4812, 6858, 9636, 13422,
18584, 25607, 35127, 47988, 65312, 88620, 120021, 162526,
220596, 301145, 415501, 583482
        }
    }

};



    struct IndexData {
        int lower;
        int upper;
    };

    float GetZ(float v, float t);
    float GetPressure(float v, float t);
```

```
        IndexData GetTemperatureIndexData(float t);
        IndexData GetVolumeIndexData(float v);
        float ReverseGasVolumeLookup(float t, float p);



};
```

B.3 fragmentation-no-ramp.cpp

```
#include "fragmentation-no-ramp.h"

// temperatures in kelvin
// uo2 burgers vector
// D.R. Olander, Fundamental Aspects of Nuclear Reactor Fuel
   Elements, EnergyResearch and Development Administration, 1976.
    TID-26711eP1.
const float UO2_BURGERS_VECTOR = 0.39;

/*
    PORE PRESSURE STRESS IN TRANSIENT
    assume fracture if tangential stress > fracture resistence

   ---------------------------------------------------------------------------

*/

float PressureDrivenFragmentationLib::pressure_equilibrium(float
   pressure_hydrostatic, float surface_energy, float pore_radius)
{
    return pressure_hydrostatic + ((2.0 * surface_energy) /
   pore_radius);
}

float PressureDrivenFragmentationLib::pressure_expansion(float
   shear_modulus, float burgers_vector, float pore_radius)
{
    return (shear_modulus * burgers_vector) / pore_radius;
}
//

float PressureDrivenFragmentationLib::pressure_limit(float
   _pressure_expansion, float _pressure_equilibrium)
{
    return _pressure_equilibrium + _pressure_expansion;
}

//       = Gb/r - 1/2* P
//
// pore_tangential_stress(pressure_expansion(),
   pressure_hydrostatic())
float PressureDrivenFragmentationLib::pore_tangential_stress(
   float _pressure_expansion, float pressure_hydrostatic)
{
    return _pressure_expansion - (0.5 * pressure_hydrostatic);
}

float PressureDrivenFragmentationLib::
   pore_tangential_stress_heating(float _pressure, float
   _pressure_hydrostatic, float _surface_energy, float
   _pore_radius)
{
    return _pressure - (((3.0 / 2.0) * _pressure_hydrostatic) +
   ((2.0 * _surface_energy) / _pore_radius));
}
```

```
/*
    ---------------------------------------------------------------------------
*/

//  _f  = 170*exp(191.34/T)*sqrt(1-2.62  ) (T=T if T <= 1000K, T=
     1000 if T > 1000K)
float PressureDrivenFragmentationLib::UO2_fracture_strength(float
     temperature, float porosity_dependance)
{
     return 170.0 * exp(-(191.34 / (temperature <= 1000.0 ?
    temperature : 1000.0))) * sqrt(1.0 - (2.62 *
    porosity_dependance));
}

//    = 0.85 * 1.4 x 1 0   * T
float PressureDrivenFragmentationLib::pressure_surface_energy(
    float temperature)
{
     return 0.85 - (0.00014 * temperature);
}
// porosity dependant surface energy J/m2
//
//    = 2.334 x 1 0  * (1-1.0915 x 1 0   * T) * (1-2.752  )
float PressureDrivenFragmentationLib::
    porosity_dependant_surface_energy(float temperature, float
    porosity_dependance)
{
     return 0.41 * pressure_surface_energy(temperature) * pow(1 -
    porosity_dependance, 4.025);
}

// E = 0.41 * (0.85 - 1.0915 x 1 0   * T) * (1 -   )

// checked against https://www.sciencedirect.com/science/article/
    pii/S0022311517318457 figure 7
float PressureDrivenFragmentationLib::young_modulus(float
    temperature, float porosity_dependance)
{
     return 233400.0 * (1.0 - (0.00010915 * temperature)) * (1 -
    (2.752 * porosity_dependance));
}

// v = 0.32 - 0.34
float PressureDrivenFragmentationLib::poissons_ratio(float
    porosity_dependance)
{
     return 0.32 - 0.34 * porosity_dependance;
}
// G = E/2(1+v)
// validated against https://www.mdpi.com/2075-4701/12/5/761
float PressureDrivenFragmentationLib::shear_strength(float
    young_modulus, float poissons_ratio)
{
     return young_modulus / (2 * (1 + poissons_ratio));
}

bool PressureDrivenFragmentationLib::burst_pore_size(float
    _hydrostatic_pressure, float _temperature, float
    _porosity_dependance, float _burgers_vector, float
    _pore_radius)
{
     float surface_energy = porosity_dependant_surface_energy(
    _temperature, _porosity_dependance); // good
     float equilibrium_pressure = pressure_equilibrium(
    _hydrostatic_pressure, surface_energy, _pore_radius);
```

```
    float _young_modulus = young_modulus(_temperature,
   _porosity_dependance); // good
    float _poissons_ratio = poissons_ratio(_porosity_dependance);
    // good
    float shear_modulus = shear_strength(_young_modulus,
   _poissons_ratio); // good


    float expansion_pressure = pressure_expansion(shear_modulus,
   _burgers_vector, _pore_radius);
    float limit_pressure = pressure_limit(expansion_pressure,
   equilibrium_pressure);
    float heating_tangential_stress =
   pore_tangential_stress_heating(limit_pressure,
   _hydrostatic_pressure, surface_energy, _pore_radius);

    float tangential_stress = pore_tangential_stress(
   expansion_pressure, _hydrostatic_pressure);
    float fracture_strength = UO2_fracture_strength(_temperature,
    _porosity_dependance); // good

    return tangential_stress > fracture_strength;
}
```

B.4 RonchiEOS.cpp

```
#include "RochiEOS.h"

using namespace std;

float RochiEOS::GetZ(float v, float t) {
            IndexData tid = GetTemperatureIndexData(t);
            IndexData vid = GetVolumeIndexData(v);



            float c00 = data[tid.lower][0][vid.lower];
            float c01 = data[tid.lower][0][vid.upper];
            float c10 = data[tid.upper][0][vid.lower];
            float c11 = data[tid.upper][0][vid.upper];

            //cout << c00 << endl;
            //cout << c01 << endl;
            //cout << c10 << endl;
            //cout << c11 << endl;

            float xweight = 1-((v-volume[vid.upper])/(volume[vid.
   lower]-volume[vid.upper]));
            float int_c00_c01 = (1-xweight)*(c00-c01)+c01;
            float int_c10_c11 = (1-xweight)*(c10-c11)+c11;


            float yweight = 1-((t-temperature[tid.upper])/(
   temperature[tid.lower]-temperature[tid.upper]));

            float zval = (1-yweight)*(int_c00_c01-int_c10_c11)+
   int_c10_c11;
            //cout << zval << endl;



            return zval;


        }

float RochiEOS::GetPressure(float v, float t) {
```

```
            IndexData tid = GetTemperatureIndexData(t);
            IndexData vid = GetVolumeIndexData(v);


            float c00 = data[tid.lower][1][vid.lower];
            float c01 = data[tid.lower][1][vid.upper];
            float c10 = data[tid.upper][1][vid.lower];
            float c11 = data[tid.upper][1][vid.upper];

            //cout << c00 << endl;
            //cout << c01 << endl;
            //cout << c10 << endl;
            //cout << c11 << endl;

            float xweight = 1-((v-volume[vid.upper])/(volume[vid.
    lower]-volume[vid.upper]));
            float int_c00_c01 = (1-xweight)*(c00-c01)+c01;
            float int_c10_c11 = (1-xweight)*(c10-c11)+c11;


            float yweight = 1-((t-temperature[tid.upper])/(
    temperature[tid.lower]-temperature[tid.upper]));

            float tval = (1-yweight)*(int_c00_c01-int_c10_c11)+
    int_c10_c11;
            //cout << zval << endl;


            return tval;


        }

RochiEOS::IndexData RochiEOS::GetTemperatureIndexData(float t) {
    IndexData ind{};
        for (int i = 0; i < 21; i++) {
            if (t >= temperature[i] && t <= temperature[i+1]) {
                ind.lower = i;
                ind.upper = i == 20 ? i : i+1;
                break;
            }
        }
    return ind;
}


RochiEOS::IndexData RochiEOS::GetVolumeIndexData(float v) {
    IndexData ind{};
        for (int i = 0; i < 21; i++) {
            if (v <= volume[i] && v >= volume[i+1]) {
                ind.lower = i;
                ind.upper = i == 20 ? i : i+1;
                break;
            }
        }
    return ind;
}

//RochiEOS::GetReversePressureVolumeIndexData(float p, float t) {
//
//}

float RochiEOS::ReverseGasVolumeLookup(float t, float p) {
    IndexData tid = GetTemperatureIndexData(t);

}
```

Appendix C

ENIGMA Irradiation conditions

C.1 Power History

	Axial Zone									
	1	2	3	4	5	6	7	8	9	10
coolant temp /C	311.00	322.00	325.50	329.50	333.00	338.00	343.00	344.00	344.00	342.00
rating /kWm^{-1}	15.98	24.47	27.93	29.56	30.26	29.94	29.04	27.20	23.30	14.01
Time /h	4									
coolant temp /C	311.00	322.00	325.50	329.50	333.00	338.00	343.00	344.00	344.00	342.00

rating /kWm^{-1}	15.98	24.47	27.93	29.56	30.26	29.94	29.04	27.20	23.30	14.01
Time /h	100									
coolant temp /C	311.00	322.00	325.50	329.50	333.00	338.00	343.00	344.00	344.00	342.00
rating /kWm^{-1}	16.22	24.78	28.14	29.63	30.13	29.71	28.77	26.94	23.15	14.09
Time /h	1500									
coolant temp /C	311.00	322.00	325.50	329.50	333.00	338.00	343.00	344.00	344.00	342.00
rating /kWm^{-1}	16.47	25.12	28.36	29.69	29.99	29.47	28.47	26.67	22.98	14.18
Time /h	1500									
coolant temp /C	311.00	322.00	325.50	329.50	333.00	338.00	343.00	344.00	344.00	342.00
rating /kWm^{-1}	16.73	25.46	28.59	29.76	29.85	29.23	28.17	26.39	22.82	14.27
Time /h	1500									
coolant temp /C	311.00	322.00	325.50	329.50	333.00	338.00	343.00	344.00	344.00	342.00
rating /kWm^{-1}	16.99	25.80	28.81	29.83	29.70	28.98	27.87	26.11	22.66	14.36
Time /h	1500									

coolant temp /C	311.00	322.00	325.50	329.50	333.00	338.00	343.00	344.00	344.00	342.00
rating /kWm^{-1}	17.24	26.14	29.04	29.90	29.56	28.74	27.57	25.83	22.49	14.44
Time /h	1500									
coolant temp /C	311.00	322.00	325.50	329.50	333.00	338.00	343.00	344.00	344.00	342.00
rating /kWm^{-1}	17.29	26.20	29.08	29.91	29.54	28.70	27.52	25.79	22.46	14.46
Time /h	300									
coolant temp /C	311.00	322.00	325.50	329.50	333.00	338.00	343.00	344.00	344.00	342.00
rating /kWm^{-1}	18.04	27.15	29.12	29.05	28.57	28.11	27.58	26.46	23.34	14.98
Time /h	1500									
coolant temp /C	311.00	322.00	325.50	329.50	333.00	338.00	343.00	344.00	344.00	342.00
rating /kWm^{-1}	18.70	27.98	29.16	28.29	27.72	27.59	27.63	27.06	24.12	15.44
Time /h	900									
coolant temp /C	311.00	322.00	325.50	329.50	333.00	338.00	343.00	344.00	344.00	342.00

rating /kWm^{-1}	19.08	27.92	28.85	27.94	27.38	27.26	27.34	26.91	24.31	15.93
Time /h	400									
coolant temp /C	311.00	322.00	325.50	329.50	333.00	338.00	343.00	344.00	344.00	342.00
rating /kWm^{-1}	20.44	27.70	27.71	26.68	26.13	26.06	26.28	26.38	25.02	17.71
Time /h	1500									
coolant temp /C	311.00	322.00	325.50	329.50	333.00	338.00	343.00	344.00	344.00	342.00
rating /kWm^{-1}	21.80	27.47	26.57	25.42	24.89	24.86	25.23	25.85	25.72	19.49
Time /h	1500									
coolant temp /C	311.00	322.00	325.50	329.50	333.00	338.00	343.00	344.00	344.00	342.00
rating /kWm^{-1}	23.16	27.25	25.42	24.15	23.65	23.66	24.17	25.31	26.43	21.27
Time /h	1500									
coolant temp /C	311.00	322.00	325.50	329.50	333.00	338.00	343.00	344.00	344.00	342.00
rating /kWm^{-1}	23.97	27.11	24.74	23.39	22.91	22.94	23.54	24.99	26.85	22.34
Time /h	900									

coolant temp /C	311.00	322.00	325.50	329.50	333.00	338.00	343.00	344.00	344.00	342.00
rating /kWm^{-1}	13.88	20.48	22.95	24.25	24.92	24.78	24.15	22.83	20.16	12.84
Time /h	200									
coolant temp /C	311.00	322.00	325.50	329.50	333.00	338.00	343.00	344.00	344.00	342.00
rating /kWm^{-1}	14.02	20.51	22.87	24.08	24.61	24.43	23.79	22.52	19.98	12.93
Time /h	1500									
coolant temp /C	311.00	322.00	325.50	329.50	333.00	338.00	343.00	344.00	344.00	342.00
rating /kWm^{-1}	14.17	20.54	22.79	23.88	24.29	24.05	23.40	22.19	19.79	13.02
Time /h	1500									
coolant temp /C	311.00	322.00	325.50	329.50	333.00	338.00	343.00	344.00	344.00	342.00
rating /kWm^{-1}	14.32	20.57	22.70	23.69	23.96	23.68	23.02	21.85	19.59	13.11
Time /h	1500									
coolant temp /C	311.00	322.00	325.50	329.50	333.00	338.00	343.00	344.00	344.00	342.00

rating /kWm^{-1}	14.48	20.60	22.62	23.50	23.63	23.30	22.63	21.52	19.40	13.20
Time /h	1500									
coolant temp /C	311.00	322.00	325.50	329.50	333.00	338.00	343.00	344.00	344.00	342.00
rating /kWm^{-1}	14.58	20.62	22.56	23.37	23.41	23.05	22.37	21.30	19.27	13.26
Time /h	900									
coolant temp /C	311.00	322.00	325.50	329.50	333.00	338.00	343.00	344.00	344.00	342.00
rating /kWm^{-1}	14.78	20.77	22.46	23.05	23.05	22.79	22.31	21.45	19.51	13.47
Time /h	400									
coolant temp /C	311.00	322.00	325.50	329.50	333.00	338.00	343.00	344.00	344.00	342.00
rating /kWm^{-1}	15.39	21.21	22.14	22.09	21.98	22.04	22.13	21.90	20.23	14.07
Time /h	1500									
coolant temp /C	311.00	322.00	325.50	329.50	333.00	338.00	343.00	344.00	344.00	342.00
rating /kWm^{-1}	15.84	21.54	21.90	21.38	21.19	21.48	21.99	22.23	20.76	14.52
Time /h	900									

coolant temp /C	311.00	322.00	325.50	329.50	333.00	338.00	343.00	344.00	344.00	342.00
rating /kWm^{-1}	16.13	21.52	21.71	21.15	20.95	21.24	21.76	22.10	20.90	14.91
Time /h	1500									
coolant temp /C	311.00	322.00	325.50	329.50	333.00	338.00	343.00	344.00	344.00	342.00
rating /kWm^{-1}	17.25	21.43	20.98	20.27	20.04	20.29	20.88	21.58	21.40	16.43
Time /h	1500									
coolant temp /C	311.00	322.00	325.50	329.50	333.00	338.00	343.00	344.00	344.00	342.00
rating /kWm^{-1}	18.38	21.34	20.24	19.39	19.13	19.35	20.00	21.05	21.90	17.94
Time /h	1500									
coolant temp /C	311.00	322.00	325.50	329.50	333.00	338.00	343.00	344.00	344.00	342.00
rating /kWm^{-1}	19.50	21.26	19.51	18.50	18.21	18.41	19.11	20.53	22.41	19.45
Time /h	1500									
coolant temp /C	311.00	322.00	325.50	329.50	333.00	338.00	343.00	344.00	344.00	342.00

rating /kWm^{-1}	19.72	21.24	19.36	18.33	18.03	18.22	18.94	20.43	22.51	19.75
Time /h	300									

C.2 Fuel Parameters

Zone Length: 0.36 m

Thermal Conductivity: 37.5 0.2165 0 0 0 2.5 1 0.118

Enrichment: 4.5%

Coolant Pressure: 15.5 MPa

Porosity: 4.5%

Pellet Dimensions: 8.2 x 10 mm

C.3 LAMMPS Gas Simulation Input File

```
variable THERMO_DAMP equal 0.1
variable BARO_DAMP equal 0.5
variable V_STEP equal 0.95


print "V_SCALE : T : SIMU_T : V : P" file ${OUT_DIR}/
   p_out_300_2000


variable T equal 200
variable T_STEP equal 100.0
variable i equal 0



#start at 0.5 scale
variable V_SCALE equal 0.5

label vloop
  clear
  boundary p p p
  atom_style full
  units metal


  # This is the box side length in Angstrom
  variable lx equal 625*${V_SCALE}

  region          box block 0 ${lx} 0 ${lx} 0 ${lx}
  create_box      1 box

  # N= 6000 Number of Xenon atoms (can be changed)
  create_atoms    1 random 6000 4823295 box
  mass 1 131.29


  velocity  all create 300.0 87287

  pair_style soft 2.0
  pair_coeff * * 400.0
  variable prefactor equal ramp(10,30)


  fix             lim all nve
```

```
  run 100
  unfix lim


  variable Xe equal 1

  variable SR_CUTOFF equal 11.0
  pair_style table linear 1000
  pair_coeff   ${Xe}   ${Xe} ${SCRIPT_DIR}/library/tang_toennies.
   lmptab Xe-Xe ${SR_CUTOFF}

  velocity all create $T 160278
  timestep 0.001



  variable i equal ${i}+1
  variable T equal 200


  label ploop
    variable NEW_TEMP equal $T+${T_STEP}
    #run up
    fix volume_fix all nvt temp $T ${NEW_TEMP} 0.1
    run 10000
    #write_data run_${NEW_TEMP}

    variable T equal ${NEW_TEMP}

    variable AVE_START equal step+5000

    fix avg_T_fix all ave/time 1 1000 1000 c_thermo_temp start ${
   AVE_START}
    #fix avg_V_fix all ave/time 1 1000 1000 v_V start ${AVE_START
   }
    fix avg_P_fix all ave/time 1 1000 1000 c_thermo_press start $
   {AVE_START}

    fix volume_fix all nvt temp ${NEW_TEMP} ${NEW_TEMP} 0.1
    run 10000



    variable AVG_T equal f_avg_T_fix
    variable V equal vol
    variable AVG_P equal f_avg_P_fix

    print "${V_SCALE}:${T}:${AVG_T}:${V}:${AVG_P}" append ${
   OUT_DIR}/p_out_300_2000
    unfix avg_T_fix
    #unfix avg_V_fix
    unfix avg_P_fix

    if ${T}==2100.0 then "jump SELF endploop"
    jump SELF ploop
  label endploop

  if ${i}==35 then "jump SELF endvloop"


  variable V_SCALE equal ${V_SCALE}-0.01


  jump SELF vloop

label endvloop
```